THE PROTON'S LONGITUDINAL SPIN STRUCTURE STUDIED THROUGH THE WEAK INTERACTION IN PP COLLISIONS

BY

DANIEL JUMPER

DISSERTATION

Submitted in partial fulfillment of the requirements
for the degree of Doctor of Philosophy in Physics
in the Graduate College of the
University of Illinois at Urbana-Champaign, 2016

Urbana, Illinois

Doctoral Committee:

Professor Jen-Chieh Peng, Chair
Professor Matthias Grosse Perdekamp, Director of Research
Professor Aida El-Khadra
Professor Peter Abbamonte

Abstract

For many years there has been limited knowledge of the spin structure of the proton. The degree to which the antiquarks and gluons of radiative origin inside the proton contribute to the total spin is particularly not well confined. The PHENIX experiment at RHIC has made measurements that have, and will, better confine these spin contributions. One of these measurements, made possible by a series of experimental upgrades, is a study of the single spin asymmetry in W boson production (A_L^W) in polarized proton-proton collisions. In this measurement, the parity violating weak interaction serves, compared to than previously used techniques, as a cleaner and more direct probe of flavor separated quark and antiquark spin-dependent momentum distributions. This is most significant in the case of the antiquark distributions, which are currently not well constrained. PHENIX has taken data toward this measurement in 2013, analysis of the data was performed, and preliminary A_L^W results have been released. Work is currently underway to finalize these results for forthcoming publication. Once finalized, these results will be included in a global fit along with data from other experiments to reduce the uncertainty of the antiquarks' contribution to proton spin. This dissertation will detail the theoretical basis for this measurement and describe the experimental and analytic procedures used to obtain the result, with special emphasis on contributions from the author.

To my parents Peter and Nancy Jumper, for solid foundations.

To my wife Elizabeth Jumper, for patient support.

To my God, the source of it all.

Acknowledgments

I would like to thank the individuals that I have worked most closely with and from whom I received the most professional support in my doctoral research.

My advisor, Matthias Grosse Perdekamp, has been a mentor and inspiration. Your professional guidance has been invaluable and your passion for science and academic excellence has served as an example to strive for. Rusty Towell was my undergraduate professor and research mentor for my first summers working at PHENIX. In addition to instilling an excitement for experimental science and holding young students to a high standard of professional independence and success, you offered your students friendship and community. I'll always consider myself an extended member of the Towell family.

Fellow UIUC group member Francesca Giordano was my most consistent coworker. I learned so much from your rigorous and structured approach to problem solving. Your guidance and oversight shaped much of my work and success. Ralf Seidl has long been an example to me of diligent pursuit of scientific goals. I'm grateful for the patient guidance you provided in my analysis efforts. Both of you were instrumental in leading the push for our A_L^W results.

Mike Beaumier has been a dear friend and valuable ally in the analysis trenches. I learned the value of coding well from you. Sanghwa Park has optimized outstanding work ethic. In doing so, you accomplished a great deal for the forward arms and spin analysis. Thanks to Chong Kim for leading the way in some earlier stages of the W analysis and for giving practical help and reference as I followed.

To some of the earlier UIUC students with whom I overlapped, Cameron McKinney, Martin Leitgab and Scott Wolin: thanks for your friendship and guidance. From coding advice, to administrative tips, to "El Plato Grande"; I appreciate your help getting established in my grad school career.

There are a huge number of other PHENIX collaborators that I've worked with and learned from, but I'll end by acknowledging the long-term PHENIXians that I've relied on most over time. Thanks first to Carter Biggs and Frank Toldo for working tirelessly for years to make the RPC's work. It wasn't easy and we couldn't have done it without you. Martin Purschke and Ed Desmond both offered all manner of computational support through my years and I don't think the RPC's would have taken data, run high

voltage or provided properly timed triggers without your help.

It takes a huge amount of emotional, personal and technical support to complete seven years of doctoral research. To those I've mentioned, and to many more that I did not list - you have my hear-felt thanks.

Table of Contents

List of Tables

List of Figures

Chapter 1

Introduction

It is presently not well understood how the proton spin can be decomposed in spin and orbital angular momentum contributions from its quark and gluon constituents. Early investigation in the matter used deep inelastic scattering of high energy lepton beams on polarized nucleon targets (DIS) as a tool to lay the foundation for current knowledge and studies into proton spin structure. There are theoretical and experimental limitations, however, for how effectively DIS can constrain certain spin contributions - especially flavor specific antiquark contributions and the gluon spin contribution. Recently, however, new techniques have been introduced for constraining these contributions by measuring spin asymmetries in the production of high momentum probes in polarized proton-proton (pp) collisions.

This dissertation will discuss the measurement of A_L^W, the longitudinal single spin asymmetry in the production of W-bosons, in $\sqrt{S} = 500GeV$ polarized pp collisions at the Relativistic Heavy Ion Collider(RHIC). A_L^W can be related to the quark, and of particular interest, antiquark spin contribution to the proton. This channel is unique in its clean access to antiquark spin and the ability to maintain this relation even with next to leading order QCD considerations. An overview of past studies of spin structure as well as the theoretical basis for this W asymmetry measurement will be presented in chapter 2

Over the past decade, the PHENIX experiment has built a new muon trigger that improves the ability to detect high momentum muons resulting from $W \rightarrow \mu\nu_\mu$ events. This increased sensitivity is important because of high levels of background events that threaten to drown $W \rightarrow \mu\nu_\mu$ signal events. Chapter 3 describes PHENIX and its detector capabilities pertinent to this measurement with emphasis on the muon trigger upgrade. It also introduces the RHIC apparatus and its polarized proton acceleration capability.

The main dataset for this measurement was taken in 2013. Chapter 4 lists details of this dataset and describes processing steps taken to prepare the raw data for analysis. A principle challenge of analyzing this data is the high occurrence of background events recorded relative to signal events in the kinematic region of interest. An involved analysis strategy is used to filter out background and estimate signal events yields that makes heavy use of simulations to model signal and background processes in various steps of the procedure. These simulations are also introduced in chapter 4 and the analysis process is detailed in chapter 5.

A preliminary result for A_L^W has been obtained with said analysis procedure and was publicly presented in 2014. Work is ongoing to finalize the analysis, in particular to finalize the systematic uncertainty of the final result. Submission for publication is anticipated within the year. The preliminary result is shown and discussed in chapter 6. This chapter also shows the projected impact of this measurement on reducing uncertainty associated with antiquark spin contributions and gives a brief outlook of future related measurements.

Chapter 2

Theoretical Background

2.1 A Brief History of Proton Structure

Today's understanding of the general internal structure of nucleons started to take shape with the introduction of the parton model in 1969[1] and related experimental measurements of the time. It became clear that nucleons consisted of quarks and gluons that contributed to their overall properties. The nucleon charge, for example came from the sum of the charge of the valence quarks. Similarly, predictions were made for spin contributions of the nucleon constituents. But in 1988 early experiments found, surprisingly, that valence quarks contributed only a fraction of the total spin of the proton and that a majority was unaccounted for[2]. The topic of nucleon spin structure has been an area of focused study for the past thirty years following this. And still, there are substantial gaps in our understanding of the sources of spin in the proton. The following subsections will further discuss the parton model and early understanding of the proton spin, then describe various experimental measurements over time and finally summarizes our current knowledge by discussing global fits of results from many of these experiments.

2.1.1 The Quark Parton Model

Early particle accelerator experiments in the 50's and 60's produced a multitude of newly discovered particles. They were initially assumed to be fundamental particles and were collectively named hadrons. In an effort to explain the large number of hadron states, Gell-Mann proposed the "quark model" in 1964[3] (Zweig also published similar work[4]). This model was a theoretical classification scheme, based on an SU(3) symmetry, that posited hadrons were composite particles with three possible constituent quarks (and the corresponding anti-quarks): the up, down and strange quark. These quarks were presented as spin 1/2 particles with fractional 1/3 or 2/3 charge and (later specified) a novel quantum number of "color charge". This was viewed as a very peculiar proposal at the time and there was skepticism that it was more than a non-physical mathematical framework. Never the less, it *was* a successful mathematical framework that classified the abundance of newly discovered light hadrons, correctly describing their basic quantum numbers

and even magnetic moment[5][6].

In 1968, Bjorken predicted that, for scattering off point-like particles at high Q^2, the structure functions (F_1 and F_2, which parameterize then unknown underlying dynamics of scattering processes) would become less dependent on Q^2 and instead depend only on what would become the Bjorken scaling variable x[7]. This prediction, referred to as Bjorken scaling, was positively observed in 1969 by early DIS experiments at the Standford Linear Accelerator (SLAC)[8][9] thus confirming that high energy scattering probes were in fact resolving a point-like particle substructure of the nucleon. Quickly afterwards, Feynman published the parton model[1] which offered such a framework in which nucleons consisted of free, charged, point-like particles called "partons".

It was not clear yet at this point, but later experiments would confirm that Feynman's partons were in fact Gell-Mann's quarks. Eventually, the quark model and the parton model together with some of their implications (i.e. color confinement and asymptotic freedom) would form the basis for Quantum Chromodynamics (QCD). This theory described dynamics of quarks and their interactions mediated by a spin 1, color-charged, massless particle the gluon (now also known as a parton along with quarks).

The above narrative leaves us then with essentially the modern understanding of the protons. Additionally, it was recognized that gluons can split in to quark, anti-quark pairs and this happens continuously within a proton. So in addition to 3 valence quarks, the proton contains a dynamic "sea" of quarks, anti-quarks and gluons.

It's useful now to introduce details of Parton Distribution Functions (PDF's). Common to much of the work described so far, is the idea of considering not only what particles are are inside the hadron, but how the hadron momentum distributed between these constituents. PDF's describe the probability density of finding a given parton at various values of bjorken x, where x can be interpreted as the fraction of total proton momentum carried by the parton. Thus, for PDF's $f_i(x)$ for each of of the i partons, the sum of the momentum weighted PDF's must equal one (i.e. the sum of the parton momentums is 100% of the nucleon momentum):

$$\sum_i \int_0^1 x f_i(x) dx = 1 \tag{2.1}$$

Not only does this conceptually give a more full picture of internal structure, but distribution of momentum carried by each parton can be related to experimental observables. For example, the stucture function F_2 can be written as a sum of charge weighted PDF's:

$$F_2(x) = \sum_i e_i^2 x f_i(x) \tag{2.2}$$

It is this type of relation between observable structure functions and quark distributions that made it possible to measure PDF's and compare them to proposed models and which ultimately affirmed the quark parton model.

2.1.2 Proton Spin Structure

A natural next step in understanding the structure of the proton is to consider its spin composition: how the various partons contribute to the total spin of the proton. One can construct spin-dependent (or polarized) Parton Distribution Functions in analog with the spin-independent (or unpolarized) PDF's introduced in the previous section. Instead of describing the momentum carried by each parton, they describe longitudinal spin alignment or anti-alignment with the proton spin and can be written as:

$$\Delta q(x) = q^{\rightarrow\Rightarrow}(x) - q^{\leftarrow\Rightarrow}(x) \tag{2.3}$$

Where $\Delta q(x)$ is the spin-dependent PDF for parton q. $q^{\rightarrow\Rightarrow(\leftarrow\Rightarrow)}(x)$ represent the spin-independent PDF for only partons aligned (anti-aligned) with the proton spin. This contrasts with the definition of the corresponding spin-independent PDF for parton q which takes the sum of spin alignment states:

$$q(x) = q^{\rightarrow\Rightarrow}(x) + q^{\leftarrow\Rightarrow}(x) \tag{2.4}$$

In the case of unpolarized PDF's, as seen in figure 2.1, the bulk of nucleon momentum is carried by the valence quarks. Thus the naive parton model assumption of the time was that the 1/2 spin of the proton came from two spin 1/2 u quarks aligned with the proton's spin and one 1/2 spin d quark anti-aligned with the proton's spin. Early studies focused on measuring the contribution of the valance quarks and, in 1988, the EMC experiment at CERN measured a quark contribution of less than 25% of the total spin of the proton[2]. This disproved the naive parton model assumption which was a very surprising result at the time (it's referred to historically as "the proton spin crisis"). This prompted numerous subsequent experiments attempting to quantify the other contributions to the proton's spin spanning from then until now. But despite many years of focused research, the various contribution are still only know with large uncertainties.

Some of the possible alternate sources of the proton's spin include sea quark spin, gluon spin and orbital angular momentum of partons within the proton. One possibility for decomposing the sources of proton spin is as follows:[10]

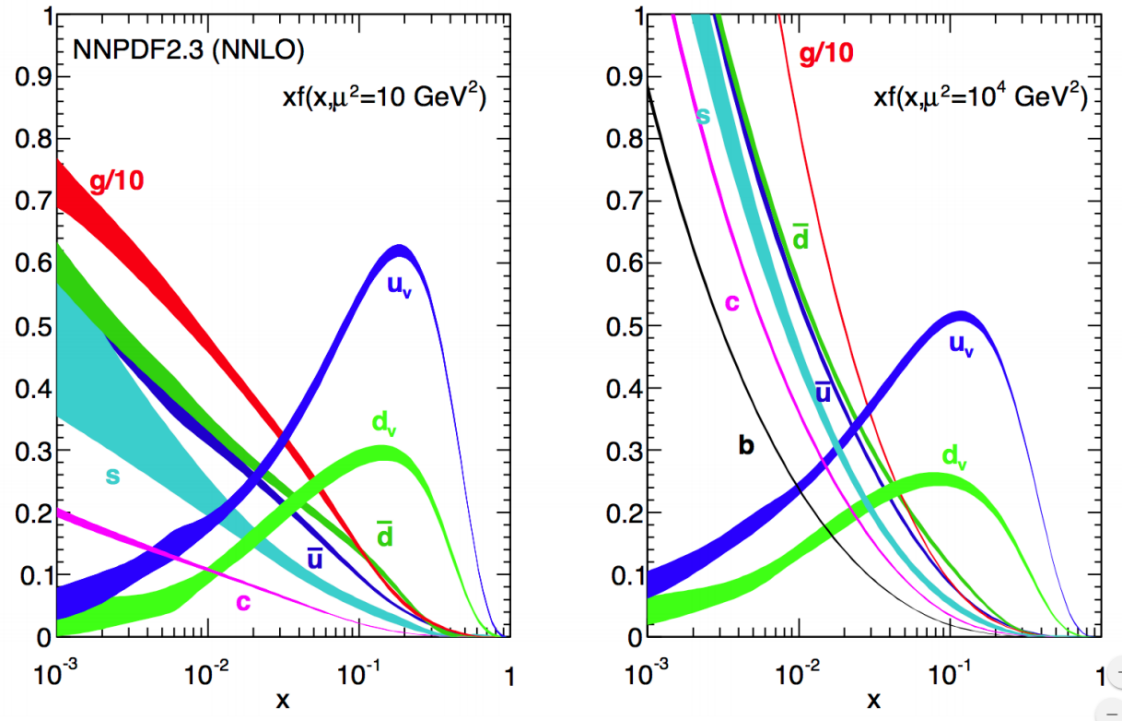

Figure 2.1: NNPDF 2.3 global fit results for unpolarized PDF's. Shown for lower (left) and higher (right) energy probes with different Q^2 values.

$$S_p = \frac{1}{2} = \frac{1}{2}\Delta\Sigma + L_q + \Delta G + L_g \tag{2.5}$$

Here $\frac{1}{2}\Delta\Sigma$ represents the spin contribution of all quarks, ΔG is the spin of the gluons, and L_q and L_g are the orbital angular momentum of the quarks and gluons respectively. $\Delta\Sigma$ can be further decomposed in to individual quark and anti-quark flavor distributions:

$$\Delta\Sigma = \Delta u + \Delta\bar{u} + \Delta d + \Delta\bar{d} + \Delta s + \Delta\bar{s} \tag{2.6}$$

Where the Δq's are the integrated polarized PDF's of each quark and anti-quark flavor. They represent the total probability of a quark's spin being aligned (or anti-aligned) with the spin of proton and can be written as:

$$\Delta q = \int_0^1 \Delta q(x)dx = \int_0^1 (q^{\rightarrow\Rightarrow} - q^{\leftarrow\Rightarrow})dx \tag{2.7}$$

Accurately measuring these polarized PDF's then is the goal in order to understand the spin structure of the proton. The following sections will review experimental efforts to constrain the polarized PDF's in both

lepton scattering and pp collisions, and then an overview will be given of global fits that use the experimental data to extract polarized PDF values.

2.1.3 Lepton Scattering

Lepton scattering has historically been the main tool for studying proton spin structure. This section will first briefly outline the theoretical tie between experimental observables and aspects of the spin structure. In polarized DIS, one can measure asymmetries between spin dependent scattering cross sections, which depend on polarized structure functions g_1 and g_2 (as well as unpolarized structure functions F_1 and F_2) which in turn can be related to polarized quark PDF's. In the simple parton model, the polarized structure function $g_1(x)$ can be written as:

$$g_1(x) = \frac{1}{2}\sum_j e_j^2[\Delta q_j(x) + \Delta\bar{q}_j(x)] \tag{2.8}$$

The polarized structure functions also relates to observable asymmetries $A_\parallel$ (for longitudinal polarization) and $A_\perp$ (for transverse polarization) as follows.

$$A_\parallel = \frac{d\sigma^{\rightarrow\Rightarrow} - d\sigma^{\rightarrow\Leftarrow}}{d\sigma^{\rightarrow\Rightarrow} + d\sigma^{\rightarrow\Leftarrow}} \text{ and } A_\perp = \frac{d\sigma^{\rightarrow\Uparrow} - d\sigma^{\rightarrow\Downarrow}}{d\sigma^{\rightarrow\Uparrow} + d\sigma^{\rightarrow\Downarrow}} \tag{2.9}$$

$$g_1(x) = \frac{F_1(x)}{(1+\gamma^2)(1+\eta\zeta)}\left[(1+\gamma\zeta)\frac{A_\parallel}{D} - (\eta-\gamma)\frac{A_\perp}{d}\right] \tag{2.10}$$

$$g_2(x) = \frac{F_1(x)}{(1+\gamma^2)(1+\eta\zeta)}\left[\left(\frac{\zeta}{\gamma}-1\right)\frac{A_\parallel}{D} + \left(\eta+\frac{1}{\gamma}\right)\frac{A_\perp}{d}\right] \tag{2.11}$$

Where $F_1(x)$ is the first unpolarized structure function, $\gamma^2 \equiv 4m^2x^2/Q^2$ and d, D, η and ζ are various kinematic factors of the scattering process. A more full treatment of these relations can be found in chapter 2 of [11] or in [12]. But for the present purposes it's sufficient to note the relation, through $g_1(x)$, of quark polarized PDF's summed for all flavors and observable asymmetries.

Early DIS measurements were made by experiments at SLAC, DESY and CERN [2, 13, 14]. They used lepton beams scattered off a nucleon and observed in the final state and measured $A_\parallel$ (and in some cases $A_\perp$). This interaction is sensitive to the flavor sums of quarks and antiquarks (eg. $\Delta u + \Delta\bar{u}$). Later experiments used Semi-Inclusive Deep Inelastic Scattering (SIDIS), where the scattered lepton as well as part of the hadronic final state of the lepton-quark interaction are observed. A statistical correlation exists between the flavor of the struck quark and, and the flavor composition of a produced hadron. This correlation was used

to gain first insight into individual quark helicity distributions with sensitivity to the products $\Delta u \Delta \bar{u}$ and $\Delta d \Delta \bar{d}$. But uncertainty on these measurments is limited because of dependance on experimentally measured fragmentation functions. Examples of SIDIS experiments include [15, 16, 17]. The final step to obtaining the polarized PDF's then is accomplished through global fits of all available data. This process will be covered in section 2.1.5.

2.1.4 pp Collisions

A more recent technique for spin structure measurements is polarized pp collisions. Thus far, this is limited to the Relativistic Heavy Ion Collider (RHIC, discussed in more detail in chapter 3) which is the only existing polarized proton collider. There are two main channels in pp that offer measurements toward contributions from different partons.

The first is high-p_T jet production, A_{LL}^{1-jet} (and to a lesser extent pion production) which both allow access to Δg, the gluon spin contribution. The double spin asymmetry for high-p_T jets is measured and can be related to Δg with next to leading order (NLO) computational techniques [18].

The second is the single spin asymmetry in W boson production, A_L^W, the topic of this thesis. This channel will be discussed in detail in section 2.2. It gives quark, anti-quark separation through sensitivity to the $\Delta q \Delta \bar{q}$ product (for u,d).

In both cases, these measurements are more direct than similarly sensitive DIS/SIDIS measurements because they avoid dependence on fragmentation functions that are present in DIS/SIDIS and thus avoid a large source of experimental uncertainty. Early results have been released for both measurements with further statistics expected. These early results have been included in the global fits discussed in section 2.1.5, giving a sense of their impact on better defining polarized PDF's.

2.1.5 Global Fits and Current Knowledge

Global fits are performed using data from experiments mentioned in the last two sections to extract distributions and uncertainties of the polarized Parton Distribution Functions as a function of x. The fits consist of varying QCD based simultaneous fits of all data points covering a wide range of x and Q^2. Two prominent groups are the DSSV author group[19, 20] and the more recent Neural Network PDF (NNPDF) collaboration[12, 18]. NNPDF's methods and results will be discussed below. Their values for polarized PDF's and the associated uncertainty represent our current best understanding of the proton spin structure and their next iterations including forthcoming data will extend this knowledge.

The NNPDF fitting procedure consists primarily of a Monte Carlo method for error propagation and a

neural network method to parameterize the PDF's[12, 18]. At a high level, this technique involves a repeated sampling of the data points with randomized variation which are then input to train a neural network to recognize the QCD driven relation between the data points and the underlying parton distributions and to estimate the associated uncertainty. The neural network technique is notable compared to DSSV and similar past techniques that used Hessian methods of PDF fitting uncertainty estimation which introduce bias with a fixed parameterization choice. The neural networks in contrast feature a very large number of free parameters thus allowing an unbiased fitting procedure. Additionally the Hessian fitting and uncertainty estimation techniques are widely used in fitting unpolarized parton distributions, but suffer in performance in the polarized case where data is more sparse and uncertainties are large.

NNPDF published one set of polarized PDF's in 2013 based on only DIS data, and another in 2014 based additionally on more recent datasets including data from SIDIS and pp experiments. Figure 2.3 shows the most recent results in comparison with DSSV results. Figure 2.2 shows the data points included from various experiments and table 2.1 lists the processes available from these datasets.

REACTION	PARTONIC SUBPROCESS	PDF PROBED	x	Q^2[GeV ^{2}]
$\ell^{\pm}\{p,d,n\} \to \ell^{\pm}X$	$\gamma^* q \to q$	$\Delta q + \Delta\bar{q}$ Δg	$0.003 \lesssim x \lesssim 0.8$	$1 \lesssim Q^2 \lesssim 70$
$\vec{p}\vec{p} \to jet(s)X$	$gg \to gq$ $qg \to qg$	Δg	$0.05 \lesssim x \lesssim 0.2$	$30 \lesssim p_T^2 \lesssim 800$
$\vec{p}p \to W^{\pm}X$	$u_L\bar{d}_R \to W^+$ $d_L\bar{u}_R \to W^-$	$\Delta u\Delta\bar{u}$ $\Delta d\Delta\bar{d}$	$0.05 \lesssim x \lesssim 0.4$	$\sim M_W^2$
$\ell^{\pm}\{p,d\} \to \ell^{\pm}DX$	$\gamma^* g \to c\bar{c}$	Δg	$0.06 \lesssim x \lesssim 0.2$	$0.04 \lesssim p_T^2 \lesssim 4$
$\ell^{\pm}\{p,d\} \to \ell^{\pm}hX$	$\gamma^* q \to q$	$\Delta u\Delta\bar{u}$ $\Delta d\Delta\bar{d}$ Δg	$0.005 \lesssim x \lesssim 0.5$	$1 \lesssim Q^2 \lesssim 60$
$\vec{p}p \to \pi X$	$gg \to gq$ $gg \to qg$	Δg	$0.05 \lesssim x \lesssim 0.4$	$1 \lesssim p_T^2 \lesssim 200$

Table 2.1: Processes Available in NNPDF 1.1 Included Data

Taken from [18]: Summary of available processes that allow for the determination of polarized PDFs. For each process, we show the leading partonic subprocesses, polarized PDFs, and the approximate ranges of x and Q2 that are accessible using the included data. Processes listed in the upper part of the table do not depend on fragmentation functions, while those in the lower part of the table do.

2.2 Sea Quark Polarized PDF's

The topic of this thesis is the W asymmetry measurment at PHENIX which aims to contribute to better constraints on the sea quark spin. As mentioned above, this technique, like SIDIS, is sensitive to $\Delta u\Delta\bar{u}$ and $\Delta d\Delta\bar{d}$. And with relatively well known $\Delta u(x)$ and $\Delta d(x)$, this make the more poorly constrained $\Delta\bar{u}(x)$ and $\Delta\bar{d}(x)$ the distributions of interest. The remaining sections in this chapter will discuss details of the

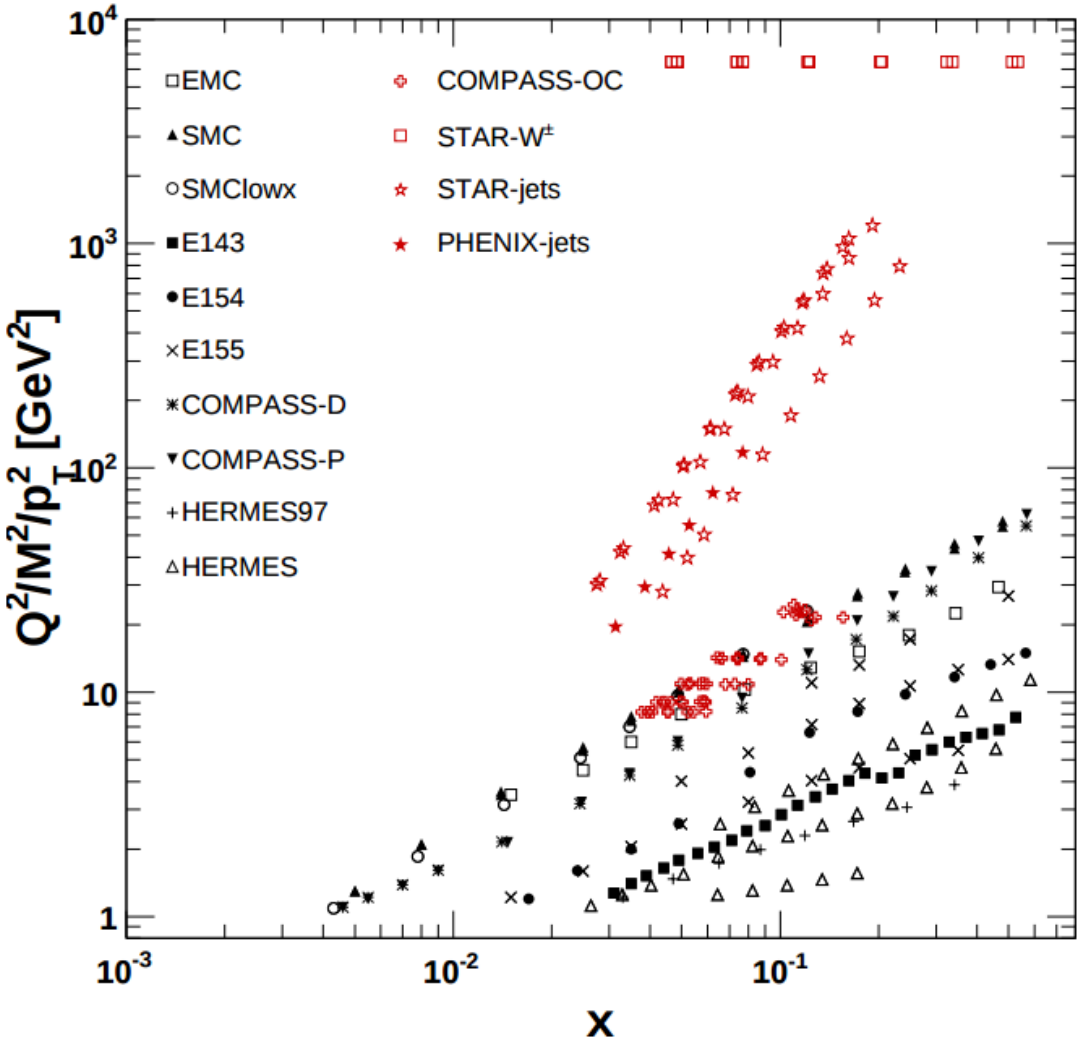

Figure 2.2: Taken from [18]: Kinematic coverage in the (x, Q^2) plane of the new experimental data included in NNPDFpol1.1 (red points, listed in Tab. 2.1) together with that of the inclusive DIS data already in NNPDFpol1.0 (black points). The new experiments are listed in the second column of the legend. For hadronic data, LO kinematics are assumed.

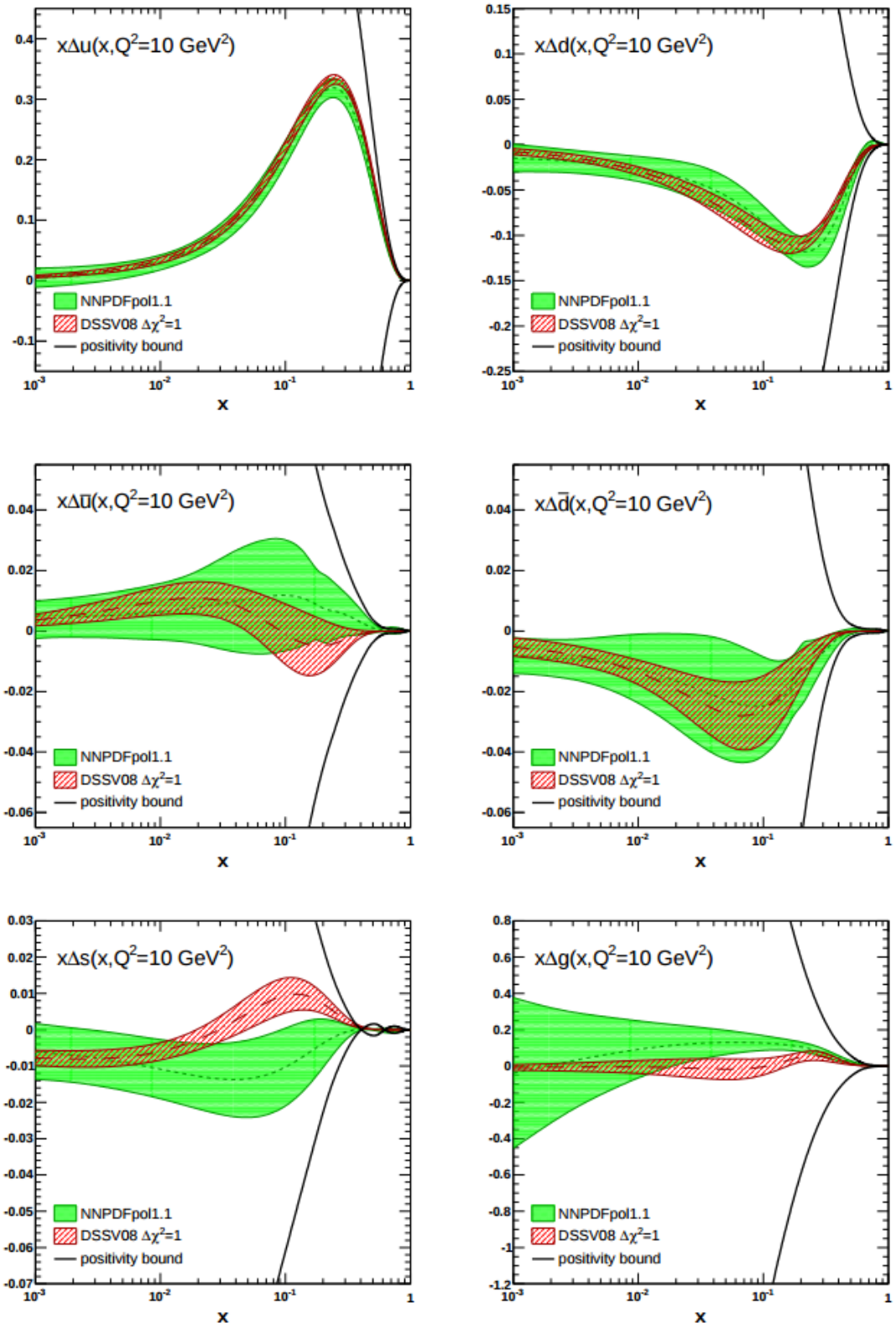

Figure 2.3: Polarized Parton Distribution Functions and uncertainty estimates generated by the NNPDF collaboration[18]. Shown in comparison with results from the DSSV author group [19]

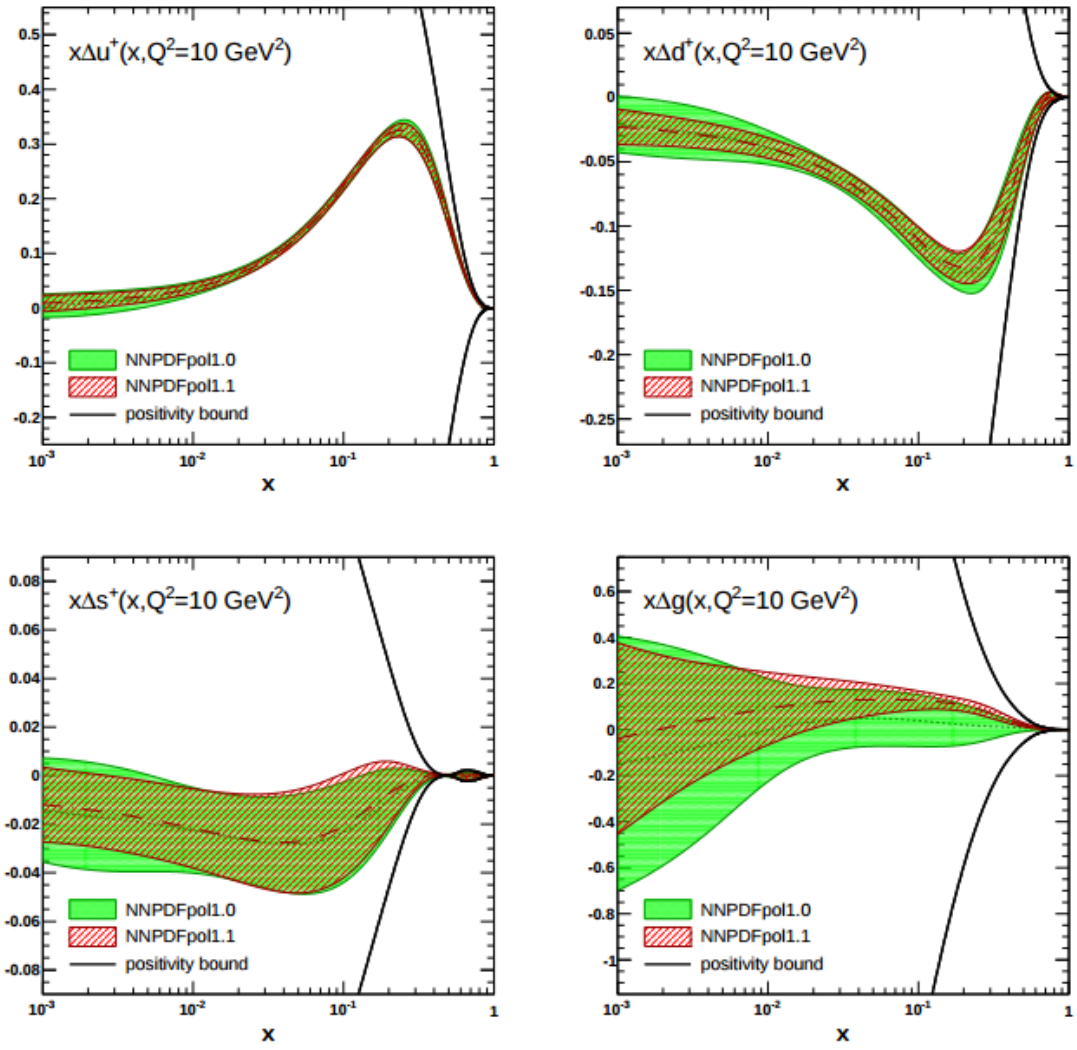

Figure 2.4: PDF results compared between NNPDF 1.0 [12], which uses only DIS data as input, and NNPDF 1.1 [18], which also includes SIDIS and *pp* data.

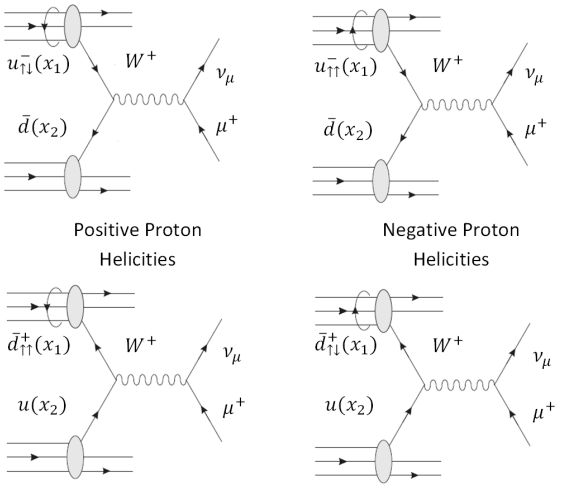

Figure 2.5: Diagrams showing the possible quark configurations for producing W^+ in p-polarized p collisions. The polarized beam's helicity is indicated by the circular arrows. In the $q^{+}_{\uparrow\downarrow}(x)$ notation, $q(x)$ is the spin independent quark momentum distribution representing simply the probability of finding a quark q in the proton with a certain x. $+$ and $\uparrow\downarrow$ are additional constraints describing the required quark helicity and the resulting spin orientation of the quark relative to the proton spin respectively. The diagrams are easily obtained for W^- production by switching the u and d flavors from the W^+ case.

theory behind this measurement, pointing out some of its advantages over SIDIS and will give an illustration of how this channel is sensitive to the individual flavor contributions.

2.2.1 Probing with the Weak Interaction

The mechanism being studied then is W boson production in longitudinally spin polarized pp collisions. By counting asymmetries of events in which W bosons are formed in polarized proton beam collisions between different polarization directions, one can extract information on quark and, particularly, flavor separated antiquark polarized PDF's. Specifically, the observable is $A_L^{\pm}$, the single spin asymmetry in W production. Though the accelerator for this experiment (detailed in chapter 3) collides two polarized p beams, for a single spin asymmetry only the polarization of one beam is considered at a time and the spin of the second beam is averaged out. The interactions of interest in this measurement are $pp \Rightarrow u\bar{d} \rightarrow W^+ \rightarrow \mu^+\nu_\mu$ or $pp \Rightarrow d\bar{u} \rightarrow W^- \rightarrow \mu^-\bar{\nu}_\mu$ where only the decay μ is observed. The subprocess driving this interaction is weak quark-antiquark annihilation. The weak interaction violates parity maximally, meaning that the W will only couple to left-handed (negative) helicity quarks and right-handed (positive) helicity antiquarks, helicity being the orientation of the quark's spin relative to direction of momentum. Additionally, the polarized PDF's for u and d are relatively well known and they show that u tends to have its spin aligned with the proton's spin and d tends have its spin anti-aligned. With these constraints, a known beam helicity, and a measured charge sign of the resulting $W \rightarrow \mu$, one can then deduce a set of only two possible flavor and spin specific $q\bar{q}$ interactions. As an example, figure 2.5 shows the possible interactions under these constraints resulting in W^+ for both positive and negative beam helicities.

This weak interaction method has several advantages over previous techniques used to study spin structure. One, the constrained set of interactions described above leads to a more direct relation between the

measured asymmetry and the spin-dependent momentum distributions. Additionally, probing quark helicity structure with W's does not require the knowledge of hadron fragmentation functions. Hadron fragmentation functions are necessary input for the extraction of quark and anti-quark helicity distributions from SIDIS data and the experimental uncertainties in the measured fragmentation functions are still large. The theoretical analysis of SIDS data and the W-data from RHIC are carried out at leading order twist in the Operator Product Expansion. At the mass scale of the W-boson ($M_W = 80GeV/c^2$, corresponding to $Q^2 = M_W^2 = 6400(GeV^2)/c^4$) contributions at sub-leading twist which are suppressed by $1/Q^2$ can be neglected. The situation is quite different for SIDIS datasets where the average $Q^2 = 3 - 10(GeV^2)/c^4$ and the suppression factor of sub-leading twist contributions in the OPE is only about 1/2 - 1/3. The following sections give details of how the spin distributions are related to W asymmetries at leading order.

2.2.2 Flavor Sensitivity in Leading Order

To understand how the asymmetry measurement is flavors sensitive to quarks and antiquarks separately, it is useful to first look at a Leading Order (LO) parton model description. The single spin asymmetry in production of W bosons for different helicities of the polarized beam can be written as Equation 2.12.

$$A_L^W = \frac{\sigma_+^W - \sigma_-^W}{\sigma_+^W + \sigma_-^W} \tag{2.12}$$

Here $\sigma_\pm^W$ is there cross section for W's to be produced for positive and negative helicities of the polarized beam respectively as indicated by the $\pm$ subscript. While not shown above, these asymmetries can be written separately for positive and negative W-bosons. To LO, the aforementioned constraints from parity violation on possible interactions can then be employed to write $\sigma_\pm^W$ in terms of quark distributions. An example of this for the W^+ case is show in equations 2.13 and 2.14. As in figure 2.5, we consider the polarized beam proton 1 and the unpolarized beam proton 2.

$$\sigma_+^{W^+} \propto u^{\leftarrow\Rightarrow}(x_1)\bar{d}(x_2) + \bar{d}^{\rightarrow\Rightarrow}(x_1)u(x_2) \tag{2.13}$$

$$\sigma_-^{W^+} \propto u^{\rightarrow\Rightarrow}(x_1)\bar{d}(x_2) + \bar{d}^{\leftarrow\Rightarrow}(x_1)u(x_2)d \tag{2.14}$$

$q(x_n)$, again refers to the unpolarized PDF and $q^{\rightarrow\Rightarrow}$ ($q^{\leftarrow\Rightarrow}$) represents the probability of finding the quark with its spin aligned (anti-aligned) with the spin of the proton. Referring again to Fig. 2.5, it can be seen that each term in these equations corresponds to one of the allowed configurations for W production. Using these cross section equations in conjunction with the definition of the polarized(eq. 2.15)

and unpolarized(eq. 2.16) PDF's

$$\Delta q(x) = q^{\rightarrow\Rightarrow}(x) - q^{\leftarrow\Rightarrow}(x) \tag{2.15}$$

$$q(x) = q^{\rightarrow\Rightarrow}(x) + q^{\leftarrow\Rightarrow}(x) \tag{2.16}$$

the following asymmetry relation can be obtained.

$$A_L^{W^+} \propto \frac{-\Delta u(x_1)\bar{d}(x_2) + \Delta\bar{d}(x_1)u(x_2)}{u(x_1)\bar{d}(x_2) + \bar{d}(x_1)u(x_2)} \tag{2.17}$$

Similarly, this process can be followed for W^- resulting in equation 2.18.

$$A_L^{W^-} \propto \frac{-\Delta d(x_1)\bar{u}(x_2) + \Delta\bar{u}(x_1)d(x_2)}{d(x_1)\bar{u}(x_2) + \bar{u}(x_1)d(x_2)} \tag{2.18}$$

These equations show, again only to LO, how the asymmetry can be related to quark distributions. Furthermore, flavor separation can be achieved by considering kinematic consequences.

If a produced W is observed in a forward direction (i.e. at a relatively small angle with respect to the beam axis) it follows that one quark in the interaction had a larger momentum and thus had a larger momentum fraction, x, while the other quark had a small x. This is significant because the spin independent antiquark momentum distribution is large at small x and small at large x, and the opposite is true for quark distributions. So different terms in the asymmetry relation reduce and can be neglected under different x conditions. If it is considered that $x_1 \gg x_2$ in the forward case and $x_1 \ll x_2$ in the backward case, then equations (2.17) and (2.18) will reduce to the following.

$$for x_1 \gg x_2,\ A_L^{W^+} \approx \frac{-\Delta u(x_1)}{u(x_1)}\ and\ A_L^{W^-} \approx \frac{-\Delta d(x_1)}{d(x_1)} \tag{2.19}$$

$$for x_1 \ll x_2,\ A_L^{W^+} \approx \frac{-\Delta\bar{d}(x_1)}{\bar{d}(x_1)}\ and\ A_L^{W^-} \approx \frac{-\Delta\bar{u}(x_1)}{\bar{u}(x_1)} \tag{2.20}$$

So, at LO pQCD and in forward directions equations 2.19 and 2.20 provide a simple relations between the measured single spin asymmetries in W production, the well-known spin independent quark momentum distributions and the goal of this study, the spin dependent quark and anti-quark distributions. There are however more complicated experimental and theoretical effects to consider.

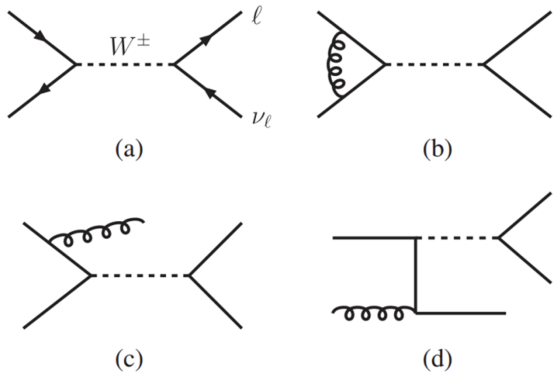

Figure 2.6: As shown in ref. [24], examples of NLO interactions in $pp \to W \to \ell\nu$. (a) LO interaction, (b) NLO virtual correction, (c) NLO real emission, (d) NLO quark-gluon scattering

2.2.3 Higher Order Effects

The asymmetries relations above are shown as a function of x, but it's possible to integrate over x to write the asymmetry in terms of kinematic parameters of the produced W such as transverse momentum, p_T, or angle with respect to the beam axis measured in rapidity, η. These variables fall more closely in line with observables measured in the experiment and η specifically will be used as the independent variable in the following discussion. So far the discussion was based on the assumption that the rapidity of the W-boson will be known experimentally. However, it is the lepton decay of the W that is observed, and its rapidity only matches that of the W under the leading order QCD assumption that the transverse momentum transfer from the W-boson, $Q_T = 0GeV/c$ [21]. In reality, radiative processes at higher order in the perturbative QCD expansion result in non-zero Q_T. Figure 2.6 shows some examples of these radiative processes. To understand and properly address this issue, simulations are performed with a program called RHICBOS. RHICBOS is a Monte-Carlo based event generator that produces W boson events based on NLO pQCD processes and including resummation of gluons emitted in the initial state [22, 23]. It uses a resummation technique to account for corrections from these soft gluon emissions and provides asymmetries as a function of the lepton kinematic variables η_ℓ and p_T. These asymmetry distributions are produced using as input separate fits of spin dependent and independent quark momentum distributions (for example the previously mentioned NNPDF and DSSV global fits). The different fits are optimized to previously available data, but make varying underlying assumptions. The plots in figure 2.7 show results of this simulated asymmetry distribution.

These plots will be used to compare the data with the various fits of spin structure and eventually be part of a global analysis that will better confine our knowledge of spin structure. Particularly notable is the spread of asymmetry predictions in backward rapidity of W^- production where the measurement has direct sensitivity between differing assumptions. RHICBOS has been used initially to show viability and

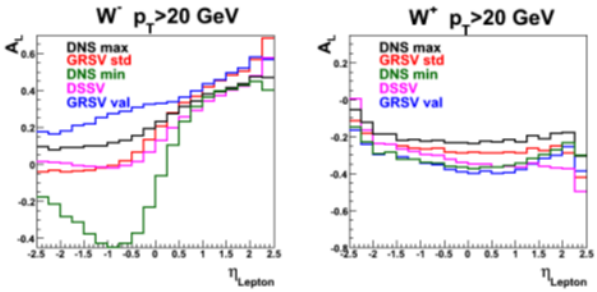

Figure 2.7: Single spin asymmetries, A_L^W from RHICBOS for different sets of helicity dependent PDF parameterizations. The large spread in $A_L^{W^-}$ at negative lepton rapidity results from the uncertainty in the $\bar{u}$ helicity distribution.

sensitivity of this measurement but also is used in an extensive series of simulations aimed at understanding the expected signal and background in the measurement. This will be discussed further in chapters 4 and 5. In addition to RHICBOS, work has been done by the authors of the DSSV global analysis to create an independent NLO corrected event generator for this measurement. In addition to providing and independent calculation, they propose a few theoretical and practical improvements over RHICBOS described in their publication [24]. As this new simulation is better designed for including W asymmetry analysis along with SIDIS data in a global fit of quark/antiquark spin distributions, their code will eventually preform that final analysis. To this end, the referenced DSSV publication contains projections on how RHIC data will fit into this analysis and affect the current spin distribution uncertainties.

Chapter 3

Experimental Apparatus

Measuring A_L^W is in essence a counting experiment: how many $W \to \mu + \nu$ events are seen for each spin polarization orientation in proton collisions. Obtaining this count requires a machine capable of polarized proton collisions, and a system of detectors capable of observing and recording details of the particles produced in the collisions. For this measurement, the Relativistic Heavy Ion Collider was used to accelerate and collide polarized protons and the PHENIX experiment operated detectors to observe, record and eventually analyze collision products. This chapter will present an overview of RHIC and its proton beam capabilities, as well as PHENIX and its detector systems pertinent to this measurement, with special emphasis on a muon detector and trigger system upgrade that was built for the W-physics program by the UIUC group and its collaborators.

3.1 The Relativistic Heavy Ion Collider

RHIC is a large superconducting collider capable of accelerating and colliding particles from protons to heavy nuclei such as Au [25]. The focus of this dissertation will be on RHIC's proton colliding capabilities with emphasis on its unique ability to accelerate spin polarized proton beams. Figure 3.1 diagrams the RHIC complex and its important components. The facility consists of a beam source, accelerating boosters and a main accelerator ring with two counter-propagating beams and six possible collision points and a circumference of about 2 miles. PHENIX and STAR are the two existing experiments observing collisions [1].

3.1.1 Components of RHIC Operation

Proton beam acceleration at RHIC starts with a polarized Hydrogen source that is used to generate protons. The group of protons is then accelerated first through a linear accelerator to 200 MeV, then through a booster synchrotron to 2 GeV and finally through the Alternate Gradient Synchrotron(AGS) to 25 GeV before being injected in to the main rings. RHIC's main accelerator consists of two rings with counter-rotating beams

[1] there were smaller, short-lived experiments at other collision points in the past

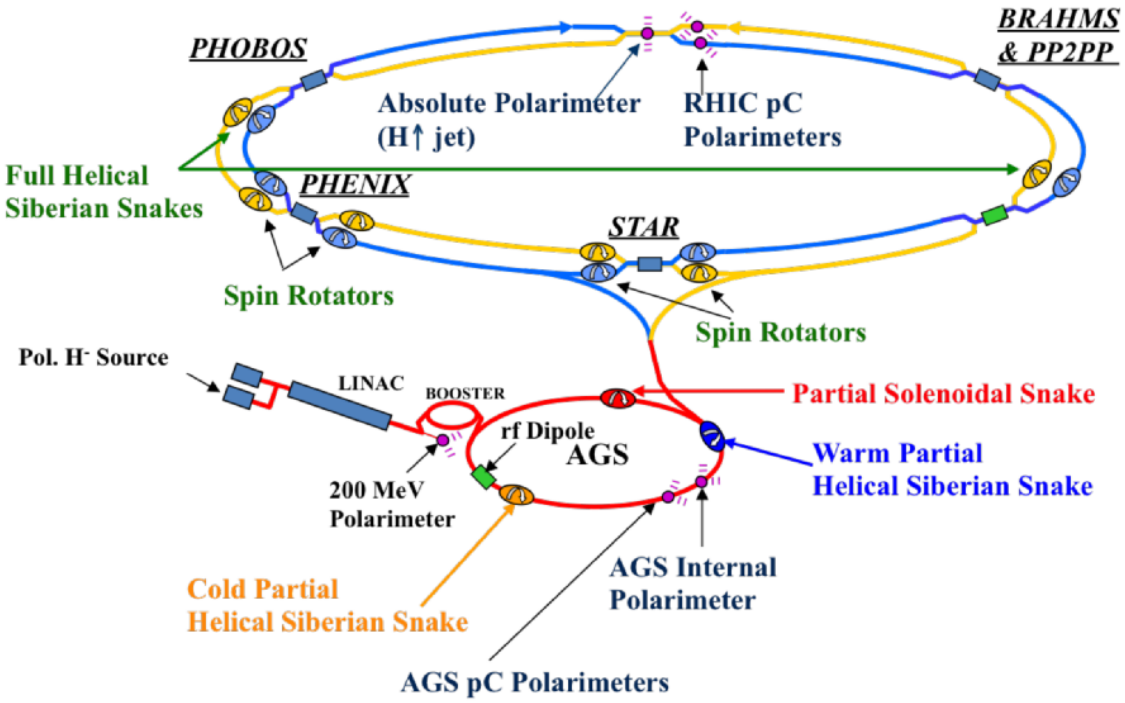

Figure 3.1: RHIC accelerator complex.

with a circumference of approximately 2 miles and a total of 1740 superconducting magnets. A switching magnet allows injection in to either the clockwise propagating ring, designated the blue ring, or in to the counter-clockwise propagating ring, designated the yellow ring. The groups of protons remain separated in "bunches" within the rings. Each ring is segmented with 120 bunches around its circumference. Most of these are filled with protons but 9 remain empty as a so called abort gap to allow time for an abort kicker magnet to activate when dumping the beam. Once the bunches are filled, RHIC accelerates the protons further to their final energy of up to 250 GeV in each ring then shifts the relative alignment of bunches between the rings to initiate collisions at the beam crossing points. Collisions at each crossing point then occur at a rate of 9.8 MHz.

3.1.2 Proton Beam Polarization

A unique aspect of RHIC compared with other colliders is the ability to maintain spin polarization thought the acceleration process. This is not a simple task because even small imperfections and misalignments in the accelerator magnets can result in a loss of polarization. However, dedicated systems have been added to the accelerator complex to accomplish this. RF dipole magnets (and a partial "Siberian Snake") in the AGS

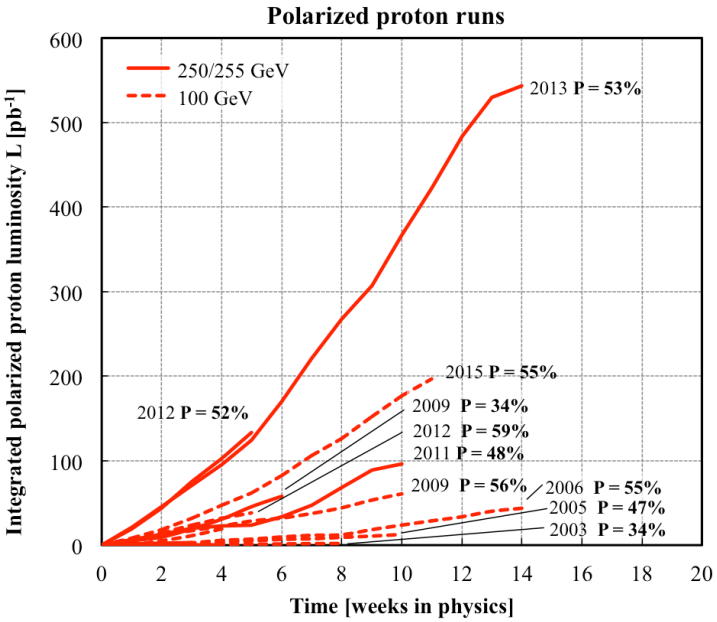

Figure 3.2: Integrated luminosity delivered by RHIC in pp runs at 250 GeV or 500 GeV center of mass energy.

and "Siberian Snake" magnets in the main RHIC ring periodically flip the spin of the protons at certain points along the ring. This allows cancellation of accelerator effects that degrade polarization by exposing the beam to these degrading effects with alternating beam spin orientation [26].

3.1.3 RHIC Performance

In recent runs, RHIC has collided protons with a center-of-mass energy of 500 GeV at a peak instantaneous luminosity of 165 $pb^{-1}s^{-1}$ with an average beam polarization above 50%. Figure 3.2 shows the integrated luminosity delivered across separate years of RHIC operation. As described, the focus of this dissertation will be on the data taken during the 2012 and particularly 2013 runs. In these runs, RHIC delivered total integrated luminosities of 277 $pb^{-}1$ and 50 $pb^{-}1$ respectively with average polarizations of 52% and 53%. As will be later discussed, the figure of merit of this measurement is proportional to integrated luminosity and the square of the average polarization, so these performance metrics have a significant impact on its quality.

3.2 PHENIX

PHENIX[27] is one of 2 main detectors on the RHIC ring. It is a multipurpose experiment consisting of many different detector systems used for a number of physics goals. The overall design philosophy is to

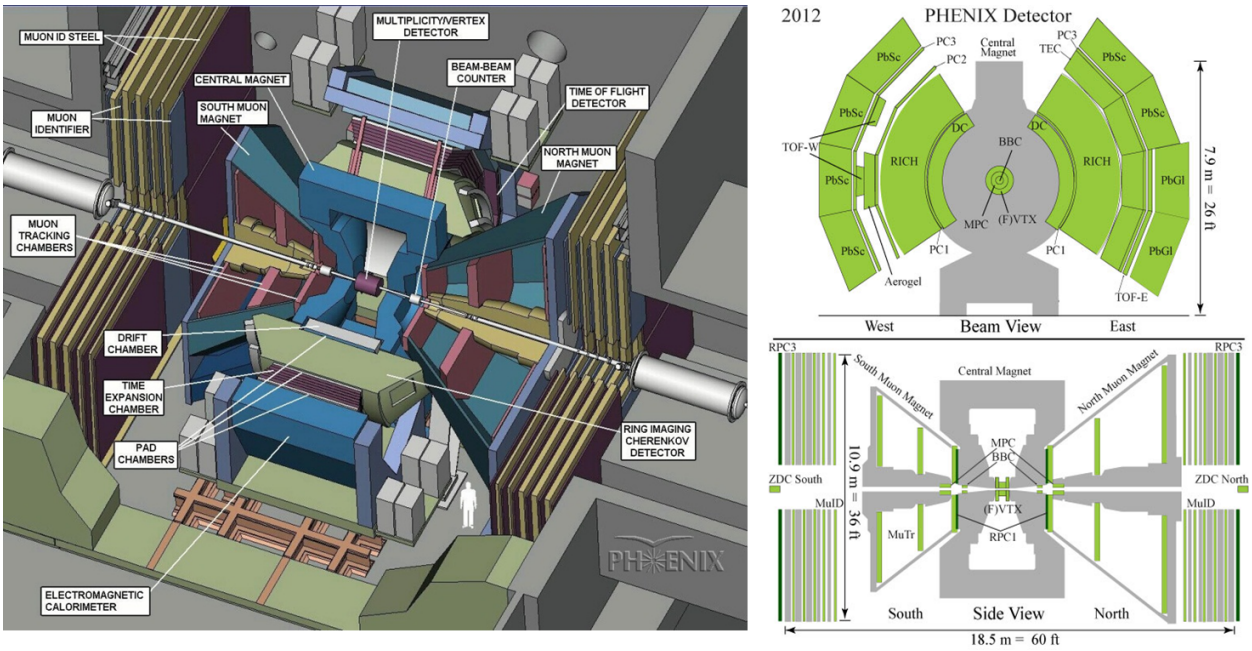

Figure 3.3: Drawing of the PHENIX experiment detectors. Left: Cut-away perspective view. Notice the orientation of the beam pipe (white) traversing from upper left to lower right. Top Right: View along the direction of beam pipe; the central arm detectors are featured in this view. Bottom Right: Side view showing the forward arms with the beam running horizontally through the center. Components of note are the 'MuID' Steel and 'MuID' layers on the left and right sides, the Muon magnets surrounding the Muon Tracking(MuTr) detectors, and the Resistive Plate Chambers (RPC1 & RPC3) drawn in dark green.

have high rate capability, good particle ID, momentum resolution from tracking, and energy resolution for photons on limited spatial sections. This results in a high volume of data on just part of the spatial area around the collision.

3.2.1 Detector Subsystems

The images in figure 3.3 show the layout of the experiment. The detectors can be generally divided into two groups: the central arms, and the forward arms. The forward arms, the system of interest for this measurement, are groups of detectors with nearly full ϕ coverage in a region of $\theta = 13 - 34°$ in the forward and backward directions.

The forward arms function as a spectrometer that consists of a series of detectors designed to identify events that produce muon candidates at small θ and provide tracking information through a magnetic field in order to calculate momentum of the candidate tracks. There are three main components in this system that will be briefly described below. Each component is roughly mirrored, with minor differences, in the forward and backward direction. Figure 3.3 features a profile schematic of the full system as described below while figure 3.4 shows a cartoon of only the main detectors used for the W analysis.

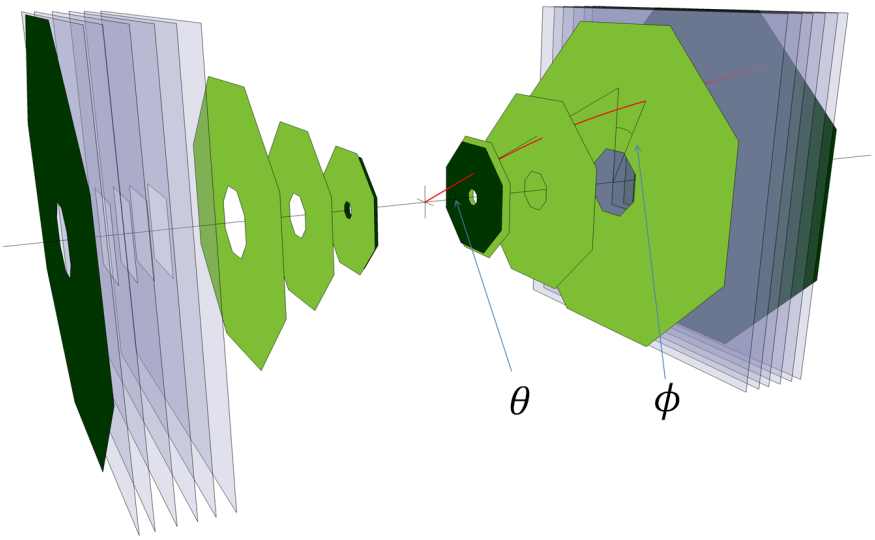

Figure 3.4: Cartoon of the active detector components of the forward arms MuTr shown in light green, RPC's in dark green, and MuID translucent. The red line represents a decay muon from W-decay formed at the interaction point and propagating through the muon arm detectors.

The first component consists of tracking detectors and a large magnet surrounding them. Both cover a range of approximately $13 - 34°$ relative to the beam line and have an octagonal ring profile orthogonal to the beam. The detectors, referred to as the muon tracker (MuTr), consist of three planes of cathode strip chambers designed for a position resolution of $150\mu m$. They are shown in light green in figure 3.4. The magnet produces a bending field radial to the beam line with $\int Bdl \approx 0.75$ Tesla-meters. A map of the field lines is shown in figure 3.5. Unfortunately, this spectrometer was not originally designed to measure momentum of high momentum tracks and its accuracy suffers as momentum increases; this issue will be discussed in the analysis section.

Next is alternating layers of absorber steel and active detector planes, again orthogonal to the beam line. The detectors, referred to as the muon identification (MuID), are streamer tubes aligned in grids which give a rough position measurement. They are drawn translucent in figure 3.4. The steel serves to absorb hadrons and provide increasing probability that a detected particle is a muon of interest for the deepest layers of detectors. The main function of the MuID is as a trigger: to identify events of potential interest and signal other detectors to record data for said event.

Lastly are two stations of Resistive Plate Chamber detectors (RPC's). One is located upstream the MuTr relative to the collision point and one downstream of the MuID, they are dark green in figure 3.4. They match the octagonal ring profile and general angular coverage of the MuTr and like the MuID, the RPC's serve as a trigger providing input for rapid online event selection but with more precise timing and position information in comparison. Together, these systems allow for selection of potential events and acquisition of

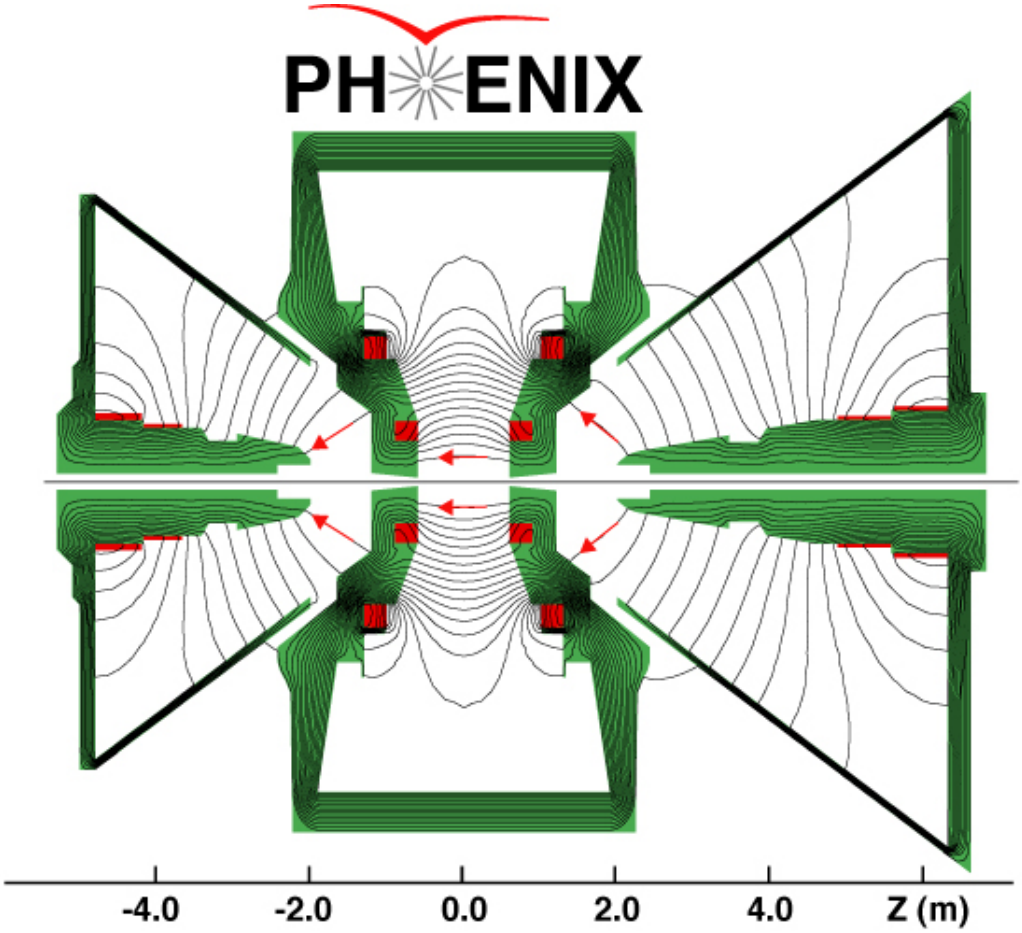

Figure 3.5: Side view of PHENIX Magnets. Magnetic field lines shown for when both central and forward magnet coils are on. hat the north muon spectrometer is on the right and the south muon spectrometer on the left.

kinematic information needed to further characterize events for the final A_L^W analysis. However, the trigger system in particular addresses the primary experimental challenge of this measurement and will be discussed in more detail in the next section.

3.2.2 Trigger Upgrade

The general purpose of any trigger is to identify possible events of interest in real time and provide a signal for other detectors to deliver data to be recorded. The forward muon arms in PHENIX mainly use information from the MuID, MuTR and RPC detector subsystems when selecting trigger events. In the past, the MuID was the only detector capable of providing trigger information. On its own, however, its rejection and discriminating power were not sufficient to accommodate the high event rate compared to the limited data acquisition bandwidth and a low signal to background[2] ratio of $W \to \mu$ events of interest inherent in the dataset. The RHIC collision rate is on the order of 10 MHz and the total data taking rate capability from all PHENIX triggers, not just those associated with the W measurement, is just over 7 kHz. This requires an initial rejection rate of three orders of magnitude just to reduce the dataset from raw collisions to a level that can be recorded. Additionally, the production of background events dominates signal events by 2-3 orders of magnitude requiring further rejection to maximize signal events in the final dataset. A two part trigger upgrade was implemented to provide the discriminating power necessary to meet this event selection demand.

The first part was a front end electronics upgrade to the MuTr detectors allowing their signal to be included in the trigger. Adding MuTr tracking information to the trigger allows for selection based on kinematic variables such as transverse momentum, which is a sensitive parameter for distinguishing signal from background events.

The second part was the design and installation of Resistive Plate Chamber detectors in the experiment. The RPC's give some spatial information, but most importantly they provide precise timing information (on the order of 3 ns resolution) that is substantially lacking in the other forward detectors. This timing information is useful for rejecting beam background not associated in time with the collision. But moreover, the MuTr time resolution is on the order of three times the collision period (300 ns), so without correlating RPC timing with a MuTr track, it is not possible to distinguish which collision a track came from. Together, these systems provide a trigger with greatly improved rejection power that is sufficient for collecting a $W \to \mu\nu$ dataset at PHENIX.

This trigger upgrade has been installed in stages from 2009 - 2013 was fully operational for the large 2013

[2]The dominant background to the single muon signal is hadronic decay events which will be discussed in detail in later chapters.

pp run. The efforts of UIUC contributed a significant portion of the workload of this upgrade, specifically in regards to the RPC's. UIUC's PHENIX group was the group primarily responsible for the development and operation of the RPC system, which is discussed in the following section.

3.2.3 Resistive Plate Chambers

As described, the RPC's play an integral role in this measurement; thus their design, installation, and eventual operation and maintenance have been important to its success. This section will introduce pertinent background information about the RPC technology and summarize work done to implement this technology at PHENIX, which has been a primary task of the author prior to the completion of data taking in 2013.

3.2.3.1 RPC Detector Technology

Resistive Plate Chambers are a type of gaseous detector that function, like many gaseous detectors, on the premise of a strong electric field generated across a volume containing a specific mixture of gases. Charged particles traversing this volume ionize certain gas molecules producing electron/ion pairs that respond to the electric field in a way that can induce an electric signal thus 'detecting' the particle. Figure 3.6 diagrams the basic construction of an RPC. The gas volume is a thin plane bounded by sheets a resistive material (often glass or specific polymer materials). As a unit, the plates and gas volume are referred to as a gas gap. Some RPC designs use multiple gas gaps stacked together. High voltage is then applied evenly across the outer surface of the gas gap, producing an electric field perpendicular to the plane of the gas volume. When incident charged particles ionize the gas, the resulting electron ion pairs travel along the direction of the electric field. Additionally, the field is strong enough to accelerate the electrons to the point of producing secondary ionizations which can in turn produce further ionization resulting in an 'avalanche' effect. 'Signal strips' are small metal planes placed adjacent to the gas gap. When an avalanche occurs, the ions produce an image charge in the signal strips and then their motion in the electric field induce an image current in the strips. This signal is captured and amplified to be processed further through the data acquisition system.

A unique property of RPC technology is that signals have effectively a self-quenching dynamic. In the steady state before a signal occurs, the applied voltage results in a build up of charge along the inner surfaces of the resistive plates (oppositely charged on each surface). When an avalanche occurs and charge drifts through the gas volume on to each plate inner surface, the charge build up is neutralized in a small local area around the avalanche. Because of the resistivity of the plate material, it takes a short period of time for the neutralized area to build up charge again. During this time the local electric field is neutralized by the neutralized charge which prevents further avalanching ionization until recharging occurs. This process takes

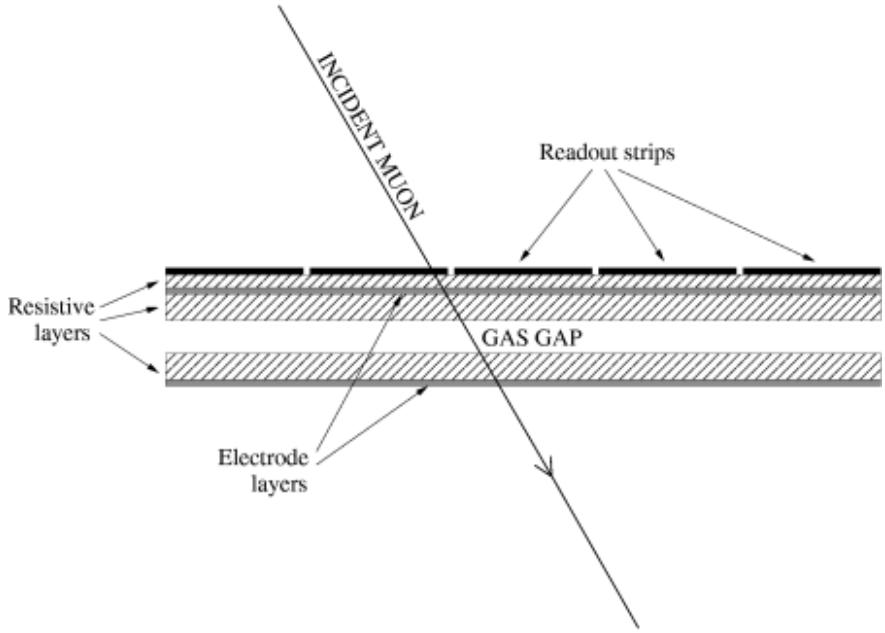

Figure 3.6: Basic construction of a resistive plate chamber.

a relatively short amount of time in contrast with mechanisms from other gaseous detectors that require a slow drift of ions through a gas volume or an avalanche that amplifies further over a longer period of time. This dynamic defines the rate capability of the detector, or the speed at which the detector is ready to detect a second signal after a first signal occurs. Rate capability ends up being one of the most important performance parameters for RPC use in PHENIX.

3.2.3.2 RPC Design for PHENIX

At PHENIX, the intended use case for these detectors is real time triggering with a high collision rate. At a high level, this requires a detector with a high rate capability and somewhat high timing resolution but only moderate position resolution. RPCs can be configured to meet these standards. Additionally the detector needs to cover a large spatial area (70 m^2 for the largest station) with many separate signal channels. The cost of RPC's per area of coverage and per signal channel are much lower than other detector technologies allowing them to maximally fill performance needs while satisfying funding constraints. These factors made RPC's an ideal choice for PHENIX.

There are a number of parameters of RPC design and operation that affect the performance capability of the detector. Some of these include the resistivity of the plate material, the composition of gas used in the gas volume, the width of the gas volume, the magnitude of high voltage applied, the number of gas gaps that are stacked and the size and shape of the signal strip. The design parameters for the PHENIX

RPC's are described in detail in the Concept Design Report submitted to Brookhaven Lab [28]. These parameters were chosen to closely match the design of RPC's used in the CMS experiment at the Large Hadron Ccollider. Their design was developed through a thorough research and development process and satisfies similar performance parameters as required by PHENIX. This allowed PHENIX to adapt their design to achieve our goals with minimal additional R&D efforts (and in fact, to take advantage of existing experience in the supply and manufacturing chain). The general design that was adopted is a double-gap, bakelite RPC with a gas composed of freon, isobutane and SF_6. Detailed design parameters of the PHENIX RPC's are listed in table 3.1 and the performance requirements that this design was intended to meet are listed in table 3.2.

Table 3.1: PHENIX RPC design parameters.

Bakelite thickness	2 mm
Bakelite bulk resistivity	$2.0 - 5.0 \times 10^{10}\ \Omega cm$
Gap width	2 mm
Gas mixture	95% $C_2H_2F_4$, 4.5% i-C_4H_{10} and 0.5% SF_6
Operating high voltage	9 kV
Number of gaps	2

Table 3.2: PHENIX RPC performance requirements

Efficiency	$> 95\%$
Time resolution	≤ 3 ns
Average cluster size	≤ 2 strips
Rate capability	0.5 kHz/cm^2
Operating plateau	> 300 V
# of streamers	$< 10\%$

In terms of the spatial arrangement within the experiment, the PHENIX RPC's have four stations, two in each arm. One of these two stations is downstream of all other detectors relative to the collision (designated RPC3) and the other is upstream from most detectors (designated RPC1). Note there is no RPC2 because of the use of nomenclature defined in historic designs that were altered later. Refer again to figure 3.3 and figure 3.4 for a spatial intuition. The ϕ and θ coverage are similar to that of the Muon Tracking detectors: almost full θ coverage and a ϕ range, with respect to the beam axis, of 14.4°-34°for RPC1 and 8.9°-28°for RPC3.

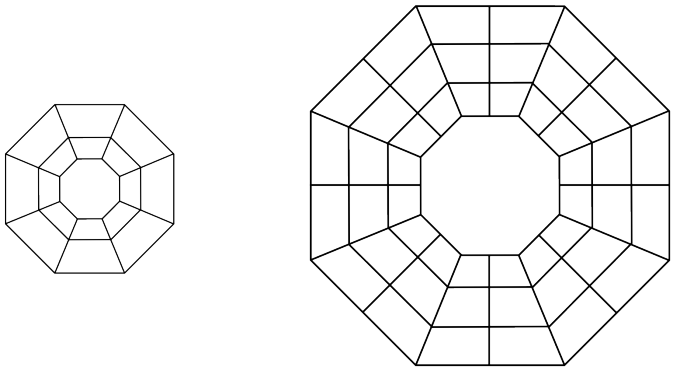

Figure 3.7: Cartoon of RPC module layouts for RPC1 (left) and RPC3 (right). Drawing is not to exact scale and is only intended to give a sense of relative module divisions and orientations.

The RPC detector planes are made of smaller modules. The modules are divided in to octant slices in θ, and have 2(3) divisions in ϕ which form "rings" for RPC1(RPC3). Figure 3.7 shows the module arrangement for RPC1 and RPC3 respectively. The signal strip layout within each module then approximates radial strips giving higher position resultion in θ and low resolution in ϕ. The strips vary in size for each station and for each "ring" radius from the beam axis, but have a width of approximately 0.85˚in theta and span either a full or half module in ϕ. Figure 3.8 shows the signal strip geometry for one octant(including two "rings") of RPC1 as an example.

3.2.3.3 Implimentation of PHENIX RPC's

Construction and installation of the RPC modules was completed in stages since 2009, and the system was fully commissioned by the 2013 run. Prior to installation, various parts and components were manufactured and shipped to BNL where the detectors were assembled and tested in a small "factory" area. Figure 3.9 shows examples of this assembly as well as a cosmic ray test stand that was used for initial testing of the modules.

Once installed, the RPC's required close attention for conditioning and operation. Resistive plate chambers are a type of gaseous detector that are very sensitive to changes and gas composition and flow and whose high voltage and current pull must be closely monitored when exposed to high beam radiation rates. This monitoring as well as maintaining the detector electronics and data acquisition interface were major operational tasks filled primarily by the author and other UIUC group members.

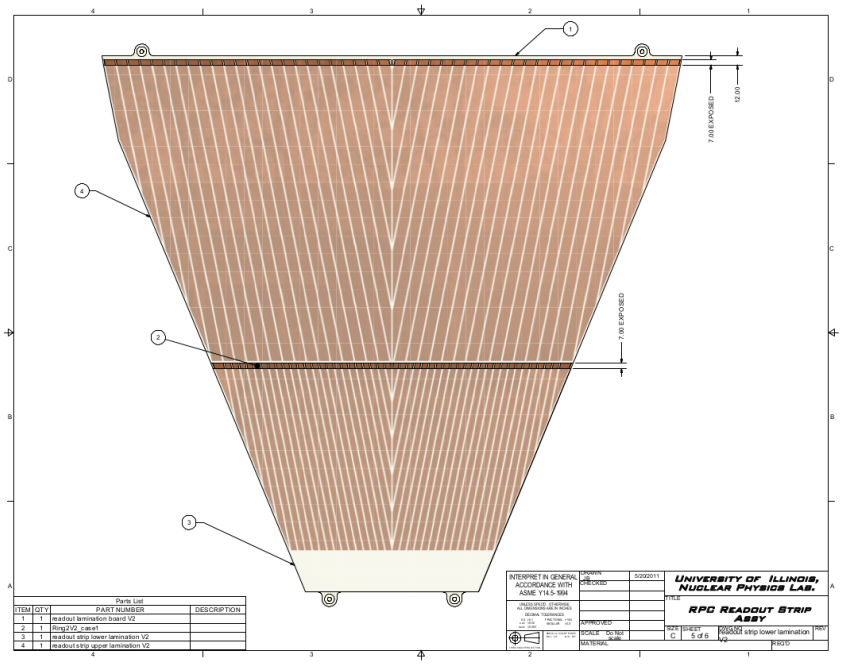

Figure 3.8: Signal strip layout for one octant (including two ϕ "modules") of RPC1.

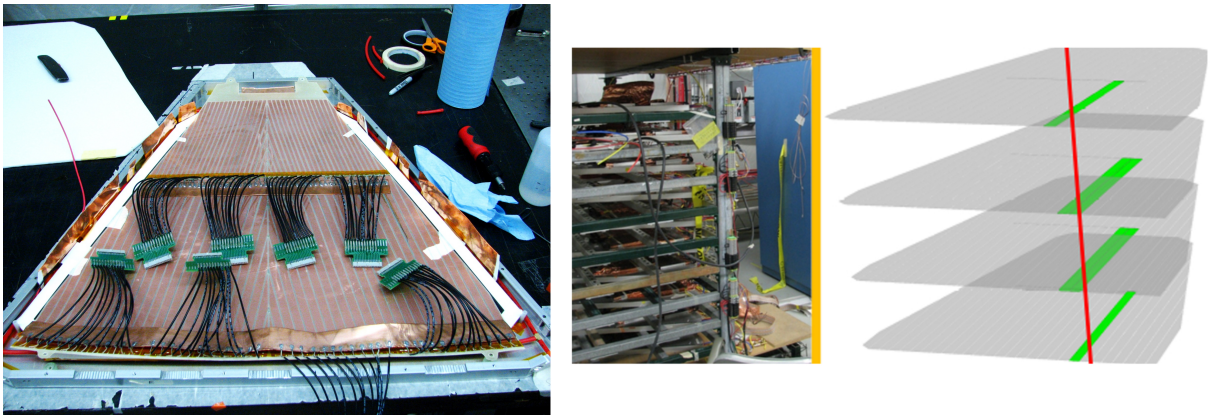

Figure 3.9: Left: Partially assembled RPC 1 module. Right: Cosmic test stand used for RPC testing. RPC modules were stacked on shelves between triggering hodoscope planes. An event display graphic showing a cosmic track and corresponding strips with signal is also shown.

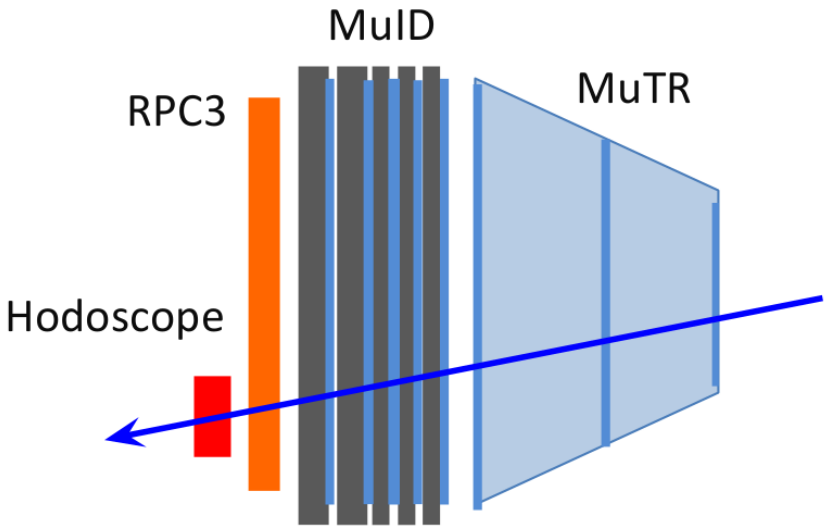

Figure 3.10: Schematic side view of one forward arm, the collision point being to the right. The location of the hodoscope relative to other detectors is shown - relative to the collision point it is the most downstream PHENIX detector. Without the hodoscope downstream, it would not be possible to tell if a tracked muon traversed RPC 3 or was absorbed in the last layer of MUID steel when calculating RPC 3 efficiency.

3.2.3.4 PHENIX RPC Efficiency Hodoscope

An peripheral project coordinated and carried out by the author was the design and construction of a pair of hodoscope that were installed adjacent to the outer RPC stations. Hodoscopes are groups of scintillator paddles in a plane. Scintillators are a particle detector composed of a scintillating material that generates photons when traversed by a charged particle and a photomultiplier tube that produces and amplifies an electric signal from the generated photons. These hodoscopes are used for measuring RPC efficiency. These RPC efficiencies are important to characterize because they are used directly as one of the correction factors applied when calculating the final A_L^W. The hodoscopes are necessary to measure these efficiencies because the outer RPC stations are the outermost detectors in PHENIX. And without downstream detection it is not possible to confirm that tracks selected for an efficiency calculation did not decay or scatter before reaching these RPC's, thus biasing the resulting efficiency. Figure 3.10 shows this possible ambiguity. However, hodoscopes positioned downstream of the RPC's over a small portion of their area can be used to select particle tracks that are know to traverse the RPC and thus give an accurate efficiency calculation which can then be extrapolated to correct the calculated efficiency for the rest of the detector.

The hodoscope design was drafted by the author, who also led construction and testing in late 2011. Figure 3.11 shows the design of one hodoscope plane. The paddles were designed to match RPC 3 readout strip orientation with one paddle covering two readout strips as shown in figure 3.12. In this way individual paddles can be used to test efficiency of pairs of RPC readout strips.

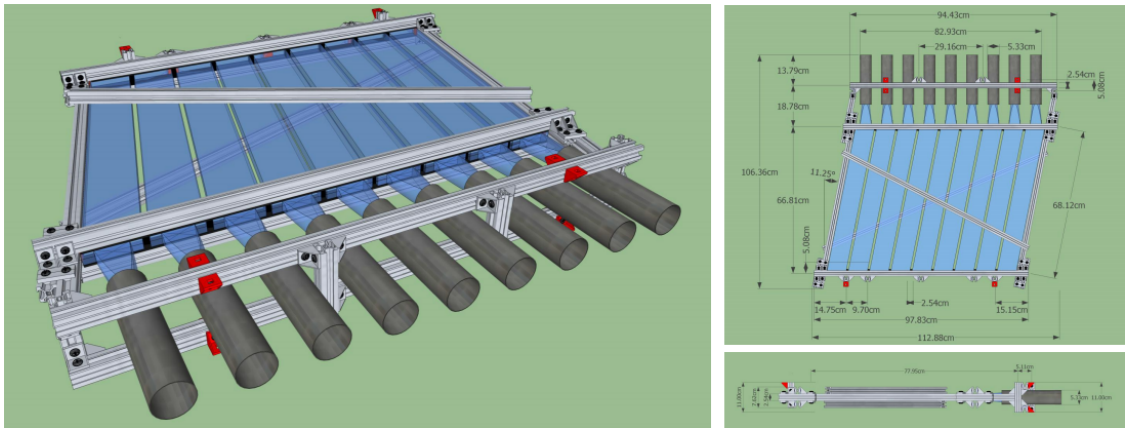

Figure 3.11: Design drawings of the RPC Hodoscopes

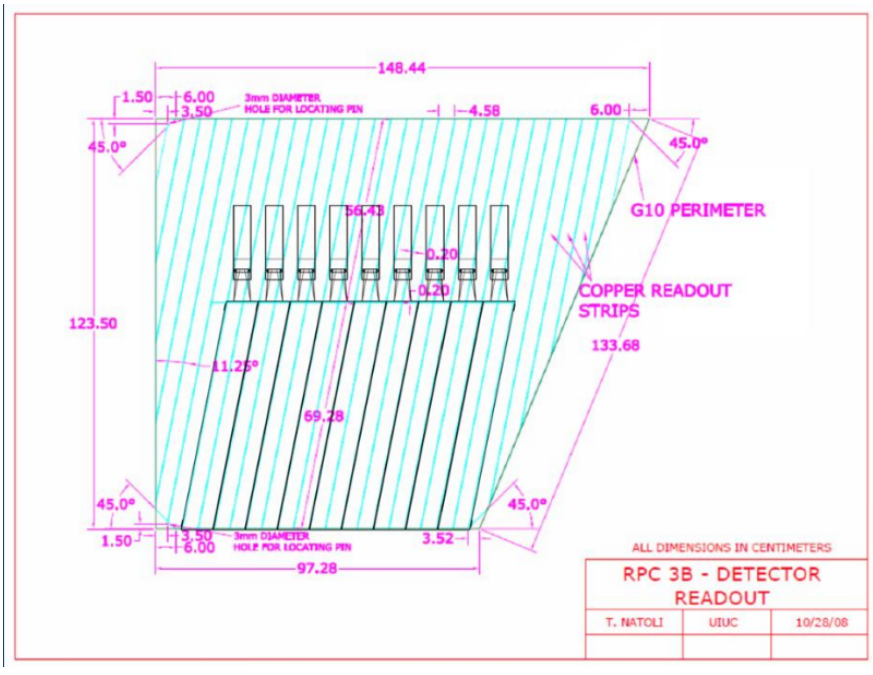

Figure 3.12: Blueprint of RPC 3 (Module B) readout strips overlayed with the hodoscope paddle design.

Figure 3.13: Photographs of the hodoscope construction process. Top: finished hodoscope with frame. Bottom Left: testing of photomultiplier voltage responses. Bottom Right: attaching light guides to scintillator paddles.

Both the scintillator material and the photomultiplier tubes were re-purposed after use in previous experiments. The material is an acrylic plastic scintillator which was larger than required for the hodoscope paddles and was machined to size at the UIUC Nuclear Physics Lab machine shop. Photomultiplier tubes were available that were tested for performance prior to construction. This work, as well as wrapping the paddles in light-tight layers and assembling the hodoscopes with their supportive frames was also completed at the NPL machine shop by UIUC students (figure 3.13 shows some of this work).

The hodoscopes were delivered to BNL and installed in January 2012. An installed hodoscope is shown in figure 3.14. Data from the hodoscopes was successfully used for efficiency calculations in run 12 and run 13.

Figure 3.14: Left: RPC outer station shown with a cartoon indicating planned hodoscope position. Right: Hodoscope in position post-installation.

Chapter 4

Data & QA

The primary data source for this analysis is $510GeV$ polarized pp collision data from RHIC's 2013 run. Section 4.1 will report details of this dataset as well as information about previous $510GeV$ pp data from PHENIX. Initial processing steps that are taken to prepare the data for analysis are discussed in section 4.2. As will prove important for later steps of the analysis, detailed studies are performed to understand the efficiency with which events are collected relative to the true rate of events (the trigger efficiency) which will be shown in section 4.3.

In addition to collision data, simulations were used to gain insight in to expected detector response for dominant signal and background collision products. Specifically, muons decayed from W bosons, muons produced by other background processes and background hadrons were generated in a simulation of the PHENIX detector. The results of these simulations will be discussed in section 4.4. And lastly, PHENIX also recorded a small set of cosmic data (cosmic muon events recorded with no active beams in RHIC). This data is used to study certain aspects of detector performance that will be described in section 4.5.

4.1 Collected *pp* Data Set

Table 4.1 gives an summary overview of the datasets collected in 2012 and 2013. Other than the large luminosity difference, the most important differences between the run years is the full inclusion of RPC triggers. Both RPC station 1 and station 3 were operated for both years, but only RPC 3 was used in triggers for most of run 12. RPC 1 and 3 were used in triggers fully in run 13. So in addition to more data in 2013, the improved triggers offered higher rejection power for better data as well.

The data from each year is segmented according to the following divisions:

- **Fill**: 8 hour periods of collisions from one beam injection. Beam is injected to the main collider and collisions occur for a target duration of 8 hour periods before the beam is dumped.
- **Run**: 90 minute periods of collision data (about 2.5TB is recorded per run). Within each fill, PHENIX collects and saves data in 90 minute target duration blocks.

	Run 12	**Run 13**
Proton Energy [GeV]	254.9	254.9
Total Delivered Integrated Luminosity [pb^{-1} in $\beta^* = 65$ cm]	133	543
Sampled Integrated Luminosity in Analysis [pb^{-1}]	50	277
Average Polarization (Blue Beam)	50.3±0.5%	50.5±0.2%
Average Polarization (Yellow Beam)	52.0±0.8%	55.4±0.2%

Table 4.1: Beam operation parameters for the 2012 and 2013 RHIC $\sqrt{s}$ =510 GeV pp datasets.

- **Event**: Data from a single collision (about 100kB is recorded per event). For each collision that satisfies a trigger criteria, signal data is recorded from all detector subsystems. There are millions of events per run.

Most of the analysis will focus on data on an event level basis. Section 4.2.2 will describe what event level collision information is used in the analysis.

4.1.1 Luminosity

The integrated luminosity values quoted above are determined using counts from the BBC. Corrections must be applied to the raw counting rate of the BBC however. As described references [29] and [30], luminosity is defined generally as:

$$L = \frac{1}{\sigma}\frac{dN}{dt} = \frac{R}{\sigma} \tag{4.1}$$

Where σ is the cross section and $dN/dt = R$ is the rate of collision events. This is integrated over the time period of data taking to give integrated luminosity. The correction needed come from the fact that it's possible for multiple proton collisions to happen in one bunch crossing. In this case the BBC will undercount as it cannot distinguish single collision from multi-collision event. Because of this, the observed rate of events must be adjusted to match a "true" rate of collisions. And this adjustment is further complicated by ambiguities in separate North BBC and South BBC efficiencies in observing events. A more complete treatment of this issue can be found in reference [31] where that measurement relies much more heavily on precise luminosity corrections. But in summary, equation 4.2 defines the observed rate in terms

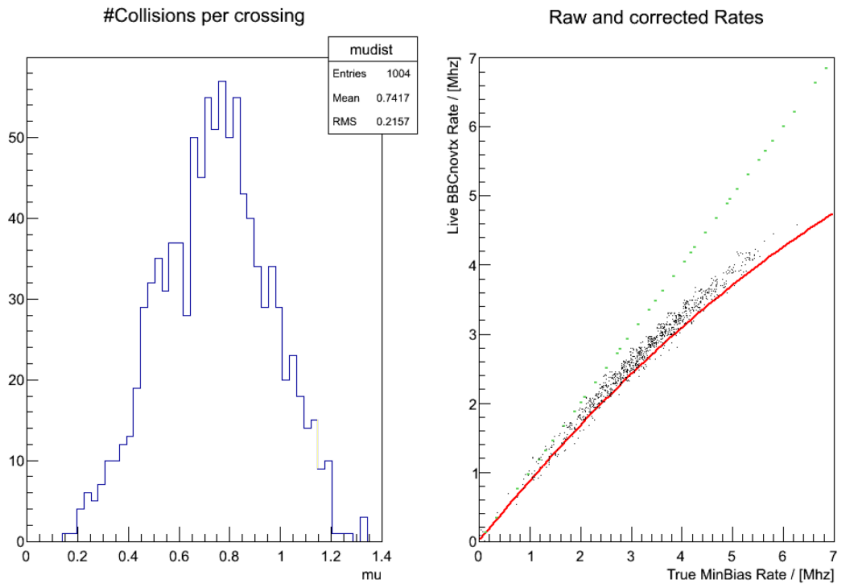

Figure 4.1: Taken from [32]. **Left**: multiple collision parameter, μ for 2013 runs. μ represents the average number of collisions per crossing **Right**: Observed vs. true BBC rates for 2013 runs. A line of slope 1 (green) would represent accurate counting. Datapoints (individual runs) shown increasing levels of under-counting as a function of collision rate. This is consistent with misidentifying multi-collision events as single collision events when muli-collisions occur more frequently at higher rates.

of experimentally determined constants. This equation is numerically solved to determine corrections for the observed rate to obtain the true rate that can then be used to calculate a true luminosity.

$$R_{BBCobserved} = 1 - e^{-\mu\epsilon_{BBC}(1+k_N)} - e^{-\mu\epsilon_{BBC}(1+k_S)} + e^{-\mu\epsilon_{BBC}(1+k_N+k_S)} \tag{4.2}$$

Where ϵ_{BBC} is net efficiency of collision detection in the BBC, measured in 2009 to be 0.53, and $k_{N(S)}$ are independent relative efficiences of $\text{BBC}_{N(S)}$ ($k_{N(S)} = \epsilon_{N(S)}/\epsilon_{BBC}$) and are determined to be $k_N = 0.289$, $k_S = 0.280$ [31]. The equation can then determine μ, the multiple collision parameter that describes the average number of collisions per bunch crossing, which can in turn be used to calculate the final true luminosity (and subsequently integrated luminosity) of the dataset.

Figure 4.1 shows the distribution of the average number of collisions per bunch crossing, μ, calculated for 2013 runs. Also shown is the relationship between observed and adjusted BBC rate. The pre-adjusted integrated luminosity was $240pb^{-1}$ and this procedure produces the previously listed true integrated luminosity of $277pb^{-1}$.

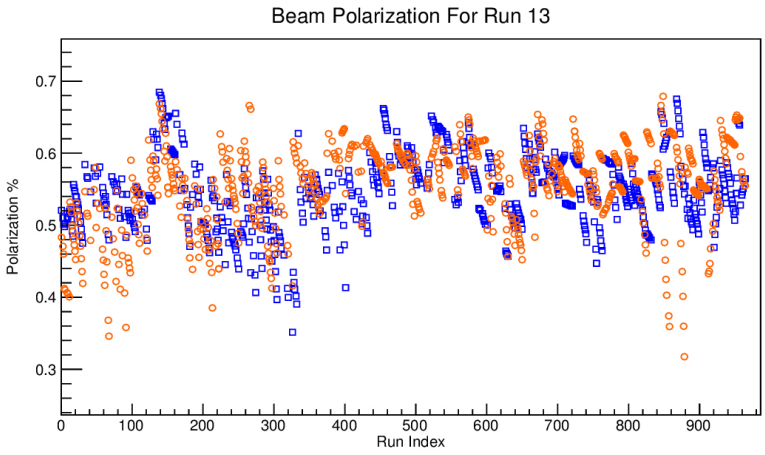

Figure 4.2: Taken from [32]. Beam polarization per run for the blue(squares) and yellow(circles) beams for 2013.

4.1.2 Polarization

Beam polarization is measured by the RHIC Polarimitry group on a fill by fill basis. Two methods are used: a proton carbon polarimeter and an atomic hydrogen jet method. More details on both techniques can be found in the RHIC Polarimitry analysis note [33] and full results as well as other details can be found on the RHIC Spin Group wiki [34]. Figure 4.2 shows 2013 beam polarizations for each run. As listed in table 4.1, the average polarization rate over the runs in the final analysis for 2013 are 50.5±0.2% for the blue beam and 55.4±0.2% for the yellow beam.

4.1.2.1 Spin Patterns

An important detail of RHIC's beam polarization is the so called "spin pattern". This describes a set order of polarization orientation for each of the 120 bunches in to which each beam is divided. On the most basic level, the patterns are designed to give equal occurance of collisions with each permutation of positive and negative helicity for the blue and yellow beams. Further though, varying the spin orientation on a bunch by bunch basis ensures any systematic beam effects or oddities affect all spin orientations evenly. For similar reasoning, a number of different patterns are used over the course of 2013 to exclude the possibility of pattern dependent effects. In 2013 there were 16 distinct combinations between blue and yellow of 8 distinct patterns. These combinations are listed in table 4.2 where $+(-)$ represent positive(negative) helicity and the indicated pattern starts at bunch 0 and repeat for all 120 bunches (including any empty bunches).

Because accurate collision-by-collision spin information is essential to calculating a spin dependent asymmetry, several consistency checks were performed on the database of recorded spin information for each run.

2013 Spin Patterns

Pattern ID	Blue Pattern	Yellow Pattern
P1	++−− ++−− ++−−	++++ −−−− ++++ −−
P2	−−++ −−++ −−++	++++ −−−− ++++ −−
P3	++−− ++−− ++−−	−−−− ++++ −−−− ++
P4	−−++ −−++ −−++	−−−− ++++ −−−− ++
P5	++++ −−−− ++++ −−	++−− ++−− ++−−
P6	++++ −−−− ++++ −−	−−++ −−++ −−++
P7	−−−− ++++ −−−− ++	++−− ++−− ++−−
P8	−−−− ++++ −−−− ++	−−++ −−++ −−++
P21	++−− ++−− ++−−	−− ++++ −−−− ++++ −−−− ++++
P22	++−− ++−− ++−−	++ −−−− ++++ −−−− ++++ −−−−
P23	−−++ −−++ −−++	−− ++++ −−−− ++++ −−−− ++++
P24	−−++ −−++ −−++	++ −−−− ++++ −−−− ++++ −−−−
P25	−− ++++ −−−− ++++ −−−− ++++	++−− ++−− ++−−
P26	−− ++++ −−−− ++++ −−−− ++++	−−++ −−++ −−++
P27	++ −−−− ++++ −−−− ++++ −−−−	++−− ++−− ++−−
P28	++ −−−− ++++ −−−− ++++ −−−−	−−++ −−++ −−++

Table 4.2: Taken from [32]. Spin patterns used in 2013. All distinct combinations of blue and yellow beam patterns are show. $+(-)$ represent positive(negative) bunch helicity and the indicated pattern (starting from the left) starts at bunch 0 and repeats for all 120 bunches, including any empty bunches.

In these checks, different sources of information are compared to confirm consistency on the relative bunch alignment between the beams, the location of the abort gap in each beam, and consistency of this information within each fill. Any runs with unresolved inconsistency are then excluded from the analysis. Full details of these tests can be found in the 2013 Spin Database QA analysis note [35].

4.1.3 Triggers

As discussed briefly in section 3.2.2, PHENIX uses some of the forward arm detectors to generate triggers. The specific combinations of detectors and logic conditions defining these triggers are important because they introduce varying bias on what events are collected in the dataset. This section will describe the muon triggers used and list accumulated yields for each.

The detector subsystems involved in the muon triggers are the BBC, MUID, MuTr and RPC's. All of these aside from BBC can function independently in the South and North arm, and each have criteria that can be evaluated in real time to make a trigger decision. Table 4.3 list all muon triggers used in 2013 and describes what combination of detectors and what criteria of each is required to record an event.

Table 4.4 lists the yield of events in the dataset associated with each trigger (including non forward muon triggers). These yields are what remain after accounting for live time and prescales. Live time is the slightly lower rate of a trigger including occasional rejected events that come in when the data acquisition is busy and not free to record. Prescales are manual settings to reject all but every n^{th} event from a certain trigger in order to reduce data bandwidth to a manageable level.

These trigger yields are informative for understanding the exact origin of events in the dataset, but a more significant variable for the A_L^W analysis is trigger efficiencies. This is the net rate at which events are collected by a trigger relative to the true rate at which compatible events occur in the collisions. This information is necessary for comparing the collected yield to the collision luminosity of the dataset, which is needed to calculate A_L^W. It's worth emphasizing the BBC and also ERT detectors in this regard. Both are independent counting detectors that attempt to detect all collisions. The BBC, in particular, without any vertex restrictions is referred to as the "minimum bias" trigger because it represents the loosest possible criteria for events to be collected by PHENIX. Because of this, the yields of these triggers are useful as a reference compared to the yield of muon triggers when calculating muon trigger efficiencies. More about the trigger efficiencies is in section 4.3.1.

Muon Trigger Descriptions

Trigger Name	BBC	MUID	MuTr	RPC
BBCLL1(>0 tubes)	<30cm vertex	-	-	-
BBCLL1(>0 tubes) narrowvtx	<15cm vertex	-	-	-
BBCLL1(>0 tubes) novertex	any vertex	-	-	-
(MUIDLL1_N1D||S1D)&BBCLL1(noVtx)	any vertex	N||S lastGap >= 1	-	-
((MUIDLL1_N2D||S2D)||(N1D&S1D))&BBCLL1(noVtx)	any vertex	(N&S lastGap >= 1) || (N||S lastGap >= 2)	-	-
MUON_N_SG1&BBCLL1(noVtx)	any vertex	-	N sagita <= 1	-
MUON_N_SG1_RPC3_1_B||C	-	-	N sagita <= 1	N (3 B||C)&(1 B||C)
MUON_N_SG1_RPC3A&MUID_N1D	-	N lastGap >= 1	N sagita <= 1	N 3 A
MUON_S_SG1&BBCLL1(noVtx)	any vertex	-	S sagita <= 1	-
MUON_S_SG1_RPC3_1_B||C	-	-	S sagita <= 1	S (3 B||C)&(1 B||C)
MUON_S_SG1_RPC3A&MUID_S1D	-	S lastGap >= 1	S sagita <= 1	S 3 A
RPC1+RPC3_N	-	-	-	N (1 B||C)&(3 A||B||C)
RPC1+RPC3_S	-	-	-	S (1 B||C)&(3 A||B||C)
SG1+RPC1(C)&MUIDLL1_N||S	-	N||S	N||S sagita <= 1	N||S 1 C
SG3&MUID_1H_N||S	-	N||S lastGap >= 1	N||S sagita <= 3	-
SG3&RPC3&MUID_1D_N||S	-	N||S lastGap >= 1	N||S sagita <= 3	N||S 3 A||B||C

Table 4.3: List of Triggers used in the 2013 run and description of hit requirements in various detectors. Some reminders about detector geometry: MUID has 5 gaps and last gap describes the furthest gap away from the collision that sees a hit. MuTr measures sagita (amount of azimuthal(ϕ) bending of a track) in terms of number of MuTr strips. RPC has two stations - station 1 is closest to the collision, station 3 is further away. Station 1 has two "rings" of modules in θ (B, C). Station 3 has three rings (A, B, C).

Trigger Yields

Bit	Trigger Name	Total* Yield (in M events)	Basic Cuts Yield	$W_{ness} > 0.92$ Yield
0	BBCLL1(>0 tubes)	77.20	16	0
1	BBCLL1(>0 tubes) novertex	566.11	108	0
2	ZDCLL1wide	73.89	11	0
3	BBCLL1(noVtx)&(ZDCN||ZDCS)	283.26	56	1
4	BBCLL1(>0 tubes) narrowvtx	350.07	90	1
5	ZDCNS	66.05	8	0
6	ERT_4x4b	154.03	479	28
7	ERTLL1_4x4a&BBCLL1(noVtx)	592.57	896	37
8	ERT_4x4c&BBCLL1(noVtx)	1172.62	1205	32
9	SG3&MUID_1H_N||S	132.71	1541	2
10	ERTLL1_E&BBCLL1(narrow)	539.25	470	11
11	CLOCK	280.47	19	0
12	MPC_B	325.26	101	1
13	MPC_A	1738.41	867	15
14	MPC_C&ERT_2x2	263.81	159	4
15	(MPCS_C&MPCS_C)||(MPCN_C&MPCN_C)	12.60	12	0
16	((MUIDLL1_N2D||S2D)||(N1D&S1D))&BBCLL1(noVtx)	324.24	66109	409
17	(MUIDLL1_N1D||S1D)&BBCLL1(noVtx)	413.20	56311	221
18	RPC1+RPC3_S	101.67	589	6
19	RPC1+RPC3_N	87.35	557	4
20	SG3&RPC3&MUID_1D_N||S	640.32	340734	1881
21	SG1+RPC1(C)&MUIDLL1_N||S	155.20	177537	1821
22	MUON_S_SG1_RPC3A&MUID_S1D	38.39	66059	886
23	MUON_N_SG1_RPC3A&MUID_N1D	80.25	118697	1307
24	MUON_S_SG1&BBCLL1(noVtx)	91.14	336	3
25	MUON_N_SG1&BBCLL1(noVtx)	73.96	146	2
26	MUON_S_SG1_RPC3_1_B||C	147.76	116215	2314
27	MUON_N_SG1_RPC3_1_B||C	179.45	123125	2322

Table 4.4: Yields of recorded events for various 2013 triggers (this includes live time and prescaling). Note: triggers are treated independently, and a single event may have more than one trigger, but in this table both triggers include that event in their yield. Yields are show for three conditions: Total* triggers in the dataset, remaining yield after basic cuts, and yield in the final reduced dataset after the W_{ness} cut

***** This "Total" is a sum of events from runs chosen using a similar but not identical criteria to the runs in our analysis dataset. So the total column should be considered as an estimate of the totals in the analysis dataset.

4.1.4 Data Composition

This section will briefly introduce some of the various underlying processes that contribute to the dataset. There are three main categories of processes present in our events as listed below. These components will be discussed in more detail in later sections but a simple understanding gives useful context for now.

- **Signal Muons**: Real muons decaying from W bosons produced in $q\bar{q}$ interactions
- **Background Muons**: Real muons produced in other interactions, such as $W \to \tau + cc$ (refered to as "wtau") or $W \to q\bar{q}$ ("whad") or most prominently open bottom, open charm, and onium sub processes.
- **Background Hadrons ("Fake Muons")**: This catagory consists of low momentum hadron events whose signal falsely mimic straight, high-momentum muon tracks (as seen in figure 4.3). Charged kaons and pions are the dominant hadrons producing this background.

4.2 Data Pre-processing

The first step from collected data toward analysis is refining the event level raw detector signals. Various quality assurance steps are taken, such as identifying and masking noisy detector channels, checking the detector high voltage status across runs or calculating run-by-run detector efficiencies and looking for abnormalities. These steps are discussed in detail in the PHENIX Muon QA analysis notes for 2013, 2012 and for reference also 2011 in references [36], [37], and [38] respectively.

The main pre-processing step, however, is generating spatial tracks of particle paths from groups of single detector hits. This "track reconstruction" will be discussed in section 4.2.1. Once tracks have been generated, various properties of the tracks are calculated that will be used for the final analysis. The variables defining these properties are described in section 4.2.2. The last step before analysis is to apply a set of "basic cuts". This is a relatively loose set of criteria meant to remove the lowest quality events. Basic cuts are listed in section 4.2.3.

4.2.1 Muon Track Reconstruction

A more detailed discussion of track reconstruction can be found in reference [39]. But the following is an overview of the steps taken to use the raw detector signals to identify coherent particle paths:

1. Generate MUID Roads

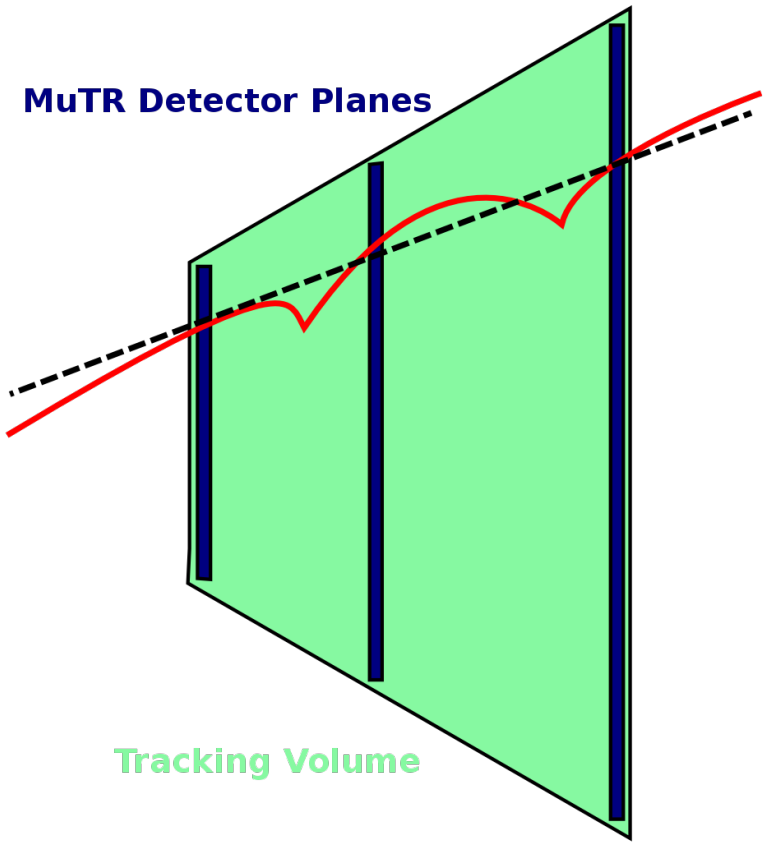

Figure 4.3: Cartoon showing the mechanism by which low momentum hadronic events can be mistaken for high momentum tracks. The red curve represents a possible hadronic track with scattering or boosted decay within the Muon Tracking volume(light green). The black dashed line represents the corresponding reconstructed track as seen by the three MuTr planes(blue).

- Identify clusters of hit channels in the various MUID gaps.
- Find sufficiently linearly correlated clusters between the gaps to define a "road".
- MUID has only coarse position resolution (8cm) so these roads define a windowed path that must point generally toward the beam axis.
- The roads are then used as a starting point for finding tracks in the MuTr.

2. Preform Detailed Tracking of MuTr Hits

   - Find clusters in all MuTr planes. Signal amplitude on adjacent strips is fit to provide a precise cluster location.
   - Project the MUID road to the outer MuTr station (station 3). Define a search window around the road.
   - Each MuTr station consists of 3 planes. Starting in the search window in station 3, identify linear tracks ("stubs") between clusters in the 3 planes.
   - Identify stubs in station 1 and 2 as well, each making separate possible tracks to station 3.
   - A rough fitting selects the best possible track between the stubs.
   - A Kalman Filter fit (technique introduced in [40]) is performed to set the final MuTr track coordinates.

3. Project MuTr Track for Matching

   - Once a detailed track has been made, it is projected forward through MUID and RPC 3 and backward to the vertex.
   - The new track is used to redefine the MUID road for the best match.
   - Clusters are searched for around the track projection to RPC 3.

4.2.2 Kinematic Variables

This section will discuss exactly what information is used from the collision data. Table 4.5 lists the main variables used in the analysis, which describe properties of the reconstructed tracks. Figure 4.4 show schematic views describing the physical meanings of some of the variables.

Name	(Unit) Description
Evt_Nmu	The number of muon tracks reconstructed for a given event
charge	$(\pm e)$ The charge associated with a reconstructed muon track
p	(GeV) The total momentum of a charged track
p_z	(GeV) The z-momentum associated with the muon track
p_T	(GeV) The transverse momentum associated with the muon track
χ^2	The result of the Kalman fitter reconstructing the track
lastGap	The last gap in the Muon Tracker which was activated (there are 4)
η	The rapidity of the track
ϕ	(rad) The azimuthal position angle the track makes relative to the x-axis
DG0	(cm) A Track matching variable (matching between MuID and MuTR) associated with the MuID road, at MuID station 3.
DDG0	(degree) The opening angle between the MuID track road, and the MuTr projection onto the MuID
xSta_i	(cm) The x-coordinate of the track at Station i, $i \in 1, 2, 3$ of the MuTr
ySta_i	(cm) The y-coordinate of the track at Station i, $i \in 1, 2, 3$ of the MuTr
θ	(rad) Azimuthal angle of track, $tan^{-1}\left(\frac{p_T}{p_z}\right)$
ϕ_i	(rad) The angle the track makes with Station i, $i \in 1, 2, 3$, i.e.: $\phi_i = tan^{-1}\left(\frac{x_1}{y_i}\right)$
$d\phi_{23}$	(rad) Difference in azimuthal angle between track position in station 2 and station 3 of the MuTR $(\phi_3 - \phi_2)$
dw_{23}	Constructed as follows: $p_T \times sin(\theta) \times d\phi_{23}$. More detail is discussed in section 5.1.2.1
DCA_z	(cm) Distance of closest approach between the z-vertex positions extracted by projecting the MuTR track z-vertex back to the BBC z-vertex
DCA_r	(cm) Distance of closest approach between the track and beam axis
Rpc1dca	Distance of closest approach between projected MuTR track onto the RPC 1 and the closest hit cluster on RPC 1
Rpc3dca	Distance of closest approach between projected MuTR track onto the RPC 3 and the closest hit cluster on RPC 3
$fvtx_{d\phi}$	The ϕ residual between MuTR track and FVTX track
$fvtx_{d\theta}$	The θ residual between the MuTR track and FVTX track
$fvtx_{dr}$	The radial residual between the MuTR track and the FVTX track
$fvtx_{conebits}$	The number of FVTX clusters inside a cone around the track defined by: $0.04rad < dR < 0.52rad$ where $dR = \sqrt{d\eta^2 + d\phi^2}$

Table 4.5: Description of event level variables used in the analysis.

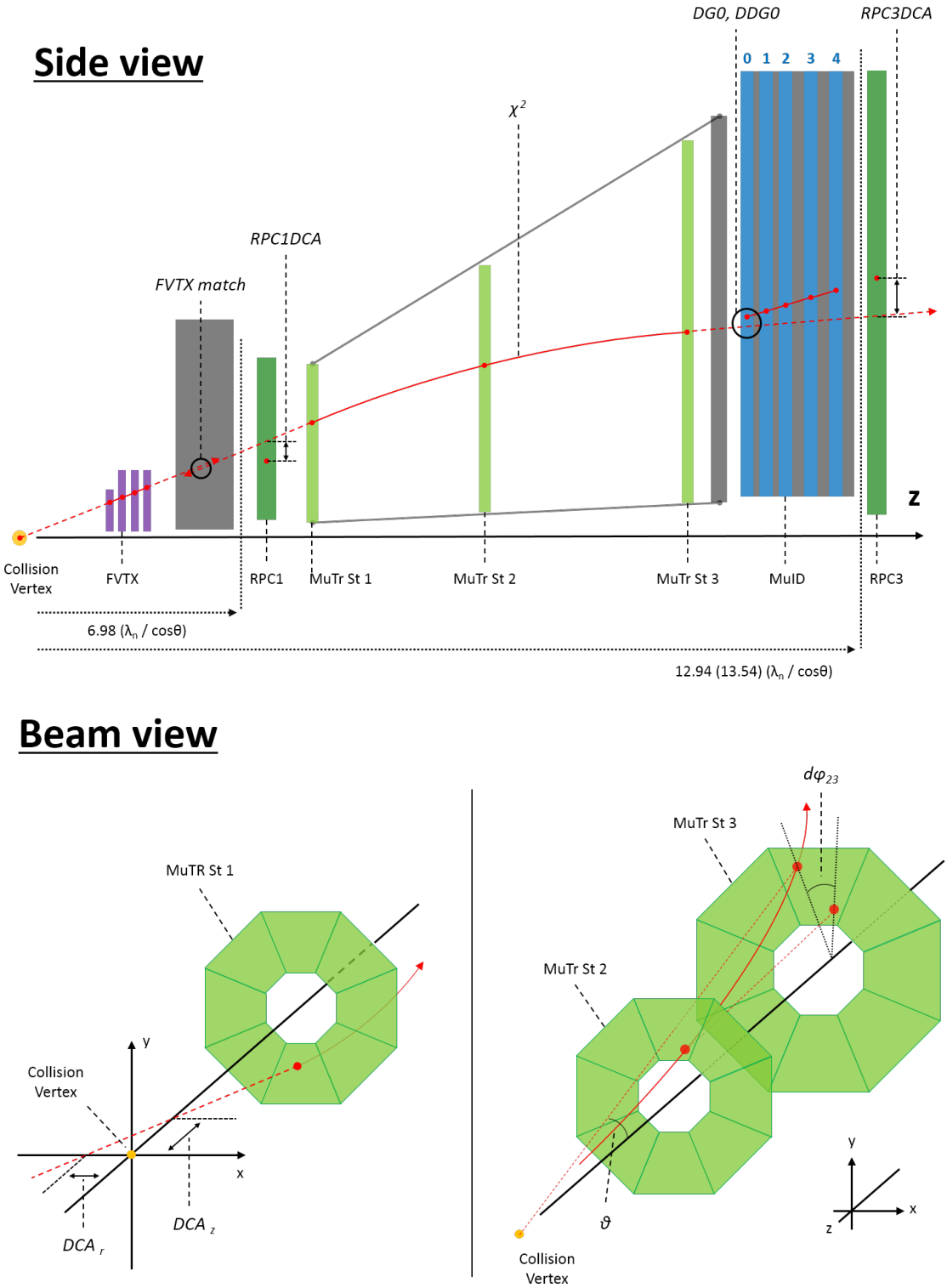

Figure 4.4: Taken from [41]. Schematic diagrams of analysis variables. The numbers at the bottom of the Top figure indicate accumulated nuclear interaction length of south (north) Muon Arm. Polar angle (θ) in bottom right indicates particular condition for dw_{23}. Note that not all analysis variables are displayed.

4.2.3 Basic Event Cuts and Criteria

Once reconstruction variables are generated, a loose set of cuts (the "basic cuts") are applied. This selection eliminates a large portion of events that are clearly background. The remaining dataset is then what is used in the A_L analysis. These basic cuts select events that meet the following criteria (again, these variables are described in table 4.5 and figure 4.4):

- lastGap = 4
- $5 < p < 250$
- $16 < p_T < 60$
- DG0 < 20
- DDG0 < 9
- $\chi^2 < 20$

4.3 Trigger Efficiencies

The efficiency with which a trigger is activated and records a muon candidate event relative to the true rate of occurrence is an important scaling factor used in the A_L^W analysis. This section will describe the process used to calculate trigger efficiencies and will list resulting values. Further details on trigger efficiency calculation can be found in reference [29]. Chapter 5 will discuss how these efficiencies are used in the analysis.

The general principle used to calculate a triggers efficiency is to choose a selection of muon events triggered by an uncorrelated trigger and check the fraction in which the trigger in question successfully fired. A number of triggers shown in table 4.4 are independent from the muon triggers. Three selections of these uncorrelated triggers are used separately to calculate efficiencies: minimum bias (BBC) triggers (trigger bits 0, 1, 3, 4), ERT triggers (bits 6-8, 10), and MPC triggers (bits 12-15). An additional criteria must be added to these triggers however to ensure the events in question are actually muon candidate events: MUID 1D. The Muon Identifier 1 deep trigger selects events seen by at least the MUID plane closest to the collision point, which means the detected particle has penetrated at least the first layer of MUID absorbing steel. And as particles other than muons tend to be absorbed in this steel, it preferentially selects muons. It is a minimum condition indicating muon events and has little correlated bias with any specific other

muon trigger. The generic efficiency for a muon trigger "a" compared with one of the reference triggers $ref = [BBC, ERT, MPC]$ is then written in terms of event counts, $N(conditions)$, as:

$$\epsilon_a^{ref} = \frac{N(ref \;\&\&\; MUID\ 1D \;\&\&\; a_{live})}{N(ref \;\&\&\; MUID\ 1D)} \tag{4.3}$$

As perhaps implied above, each trigger will be treated independently in calculating efficiencies. But further, because a single event can be associated with more than one trigger, each distinct combination of triggers will also be treated separately to avoid any sort of efficiency double counting. While this could in principle lead to a huge permutation of trigger combinations, in reality the majority of events have just one or two triggers. So this expansion is quite manageable. A total trigger efficiency is then produced by combining results for each separate trigger combination.

4.3.1 Trigger Efficiencies vs. η

Figure 4.5 shows the distribution of events collected with the various muon triggers with respect to rapidity (η). A first clear observation is that the triggers differ strongly in their η distributions. This is due largely to the spatial location of detector modules present in the trigger criteria. Because of this, trigger efficiency will be treated as a function of η (more specifically, in separate η bins). Trigger efficiency also has dependence on other event-level kinematic variables such as p_T and the likelihood variable W_{ness}(which will be introduced in section 5.1.1). To be properly evaluated, the efficiencies should also be binned with respect to these variables, but statistics limitations at the higher p_T and W_{ness} regions restrict this. These higher regions will be the region of interest for our analysis however. So trigger efficiencies are binned with respect to these variables, with large resulting error bars, then a fit is performed to extrapolate a value to use for efficiency at higher p_T and W_{ness}.

A comprehensive set of plots of trigger efficiency with respect to η for each muon trigger can be found in reference [29], but examples for the most prominent triggers can be found in figures 4.6, 4.7, 4.8 and 4.6. Note the varying distributions with respect to η which is, again, due primarily to the different spacial location of detectors associated with each trigger.

These efficiencies were calculated with a relatively fine binning of 15 bins in η. In order to check the trend of trigger efficiency with respect to p_T and W_{ness} a more coarse binning must be used due to limited statistics. A binning of three bins in η with boundaries at 1.1, 1.4, 2.0 and 2.6 was selected. Trigger efficiency binned with respect to p_T and (separately) W_{ness} were then calculated independently for each of the three η bins. Again, a full set of permutations for these plots can be found in reference [29] but for brevity, examples will be shown just for trigger bit 20 (SG3&RPC3&MUID_1D_N||S), which is representative of trends seen

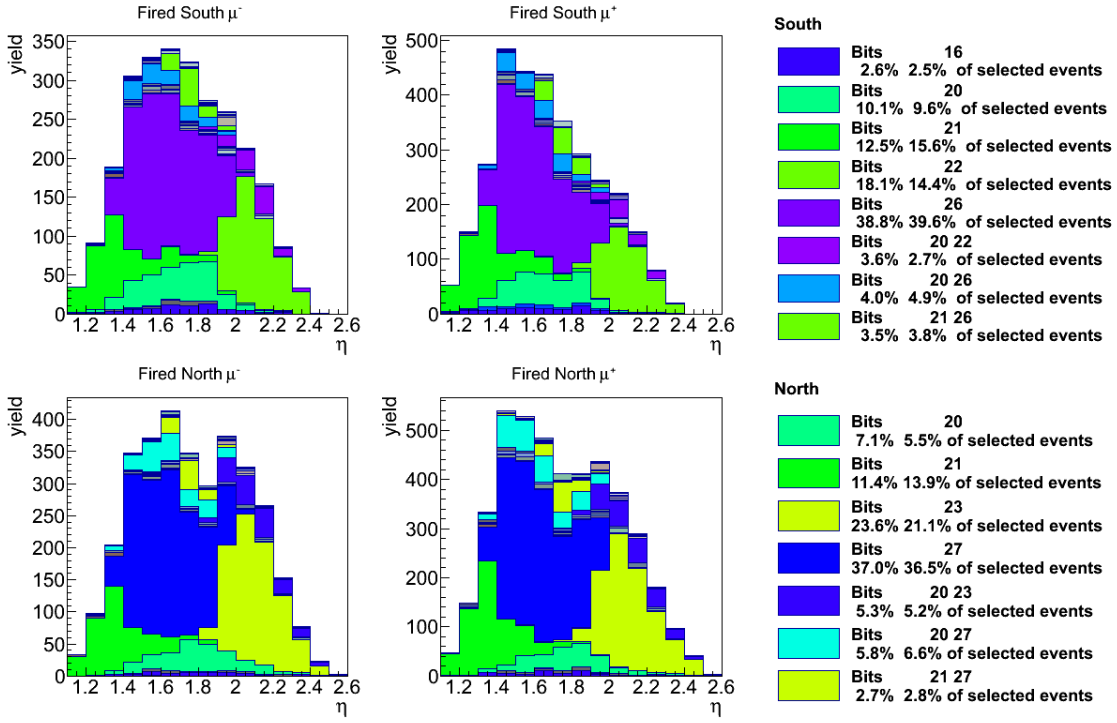

Figure 4.5: Taken from [29]. Stacked histogram of collected events versus η for each trigger combination. The legend labels bits for trigger combinations that had a high percentage of events of the total dataset. For reference, table 4.4 lists triggers associated with each trigger bit and 4.3 describes their detector criteria.

in many of the triggers.

4.3.2 Trigger Efficiencies vs. p_T

Figures 4.10, 4.11, and 4.12 show the trigger efficiencies with respect to p_T for the three aforementioned η bins. Generally, true $W \to \mu\nu$ events are expected to have increasing trigger efficiency with increasing p_T. The measured values, however, show a bump at relatively low p_T then decreasing efficiency as p_T increases from there. This turns out to be an effect of "fake muon" events (introduced in section 4.1.4). These are hadrons that decay or scatter in the MuTr volume in such a way that the track reconstruction mimics the straight path of a high momentum muon. These events are expected to have poor efficiency because they are not true muons and are not likely to penetrate the MUID steel or have correlated hits in other detectors (particularly RPC 3). Thus the presence of this background in the high p_T region brings down the measured trigger efficiency. To account for this high-p_T efficiency dilution of true efficiency for real muons, a plateauing error function is fit to the data that extrapolates this "bump" to the higher p_T region:

$$f(x; C_0, C_1, C_2) = \frac{C_0}{2}\left(1 + \text{TMath::Erf}\left(\frac{x - C_1}{\sqrt{2}C_2}\right)\right) \tag{4.4}$$

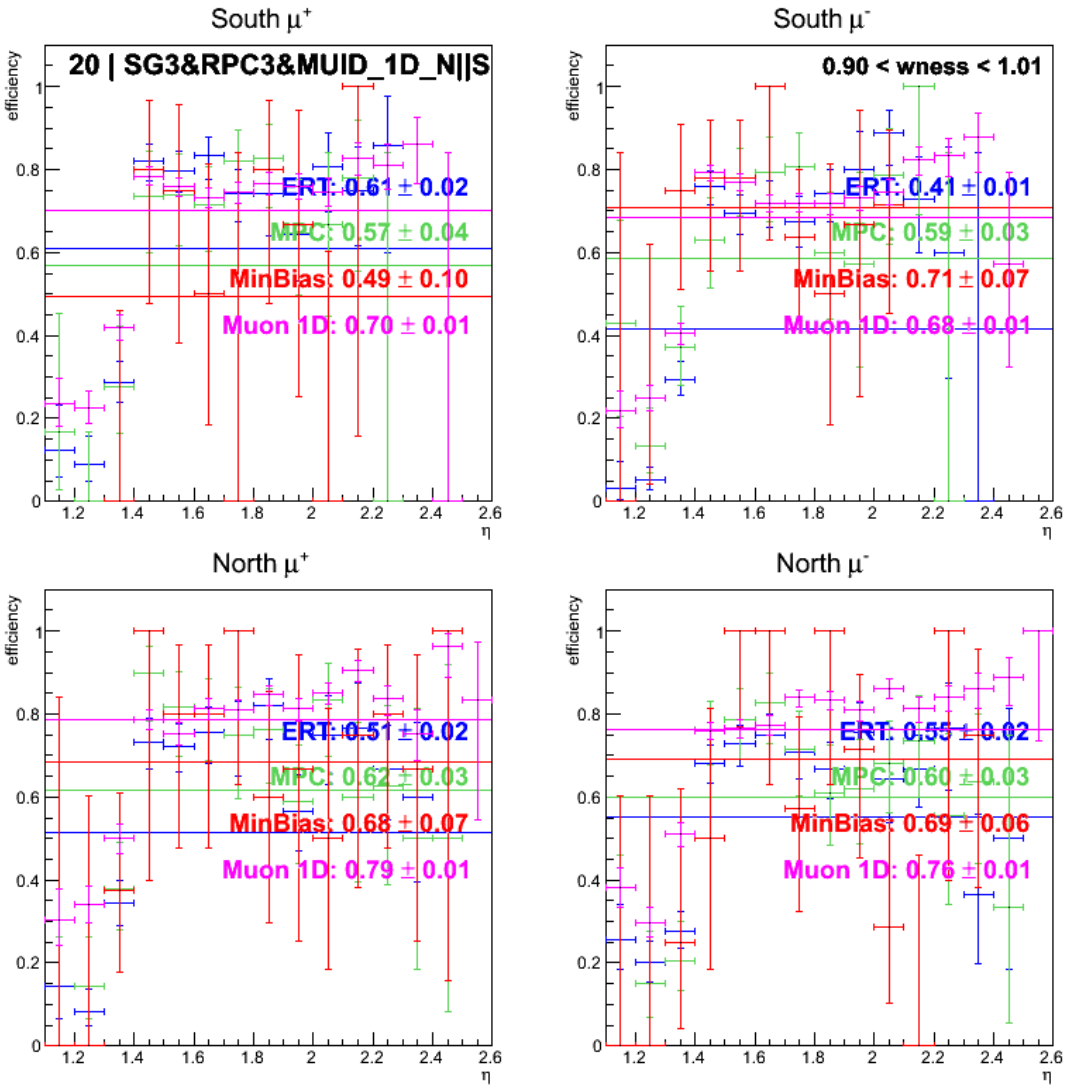

Figure 4.6: Taken from [29]. Trigger efficiency vs η as calculated compared to different reference triggers for **trigger bit 20 - (SG3&RPC3&MUID_1D_N||S)**. Muon candidate events with $p_T > 5$ are considered. For each reference trigger, ERT (Blue), MPC (green), MinBias or BBC (red) and MUID 1D (purple), the value of a constant fit is shown.

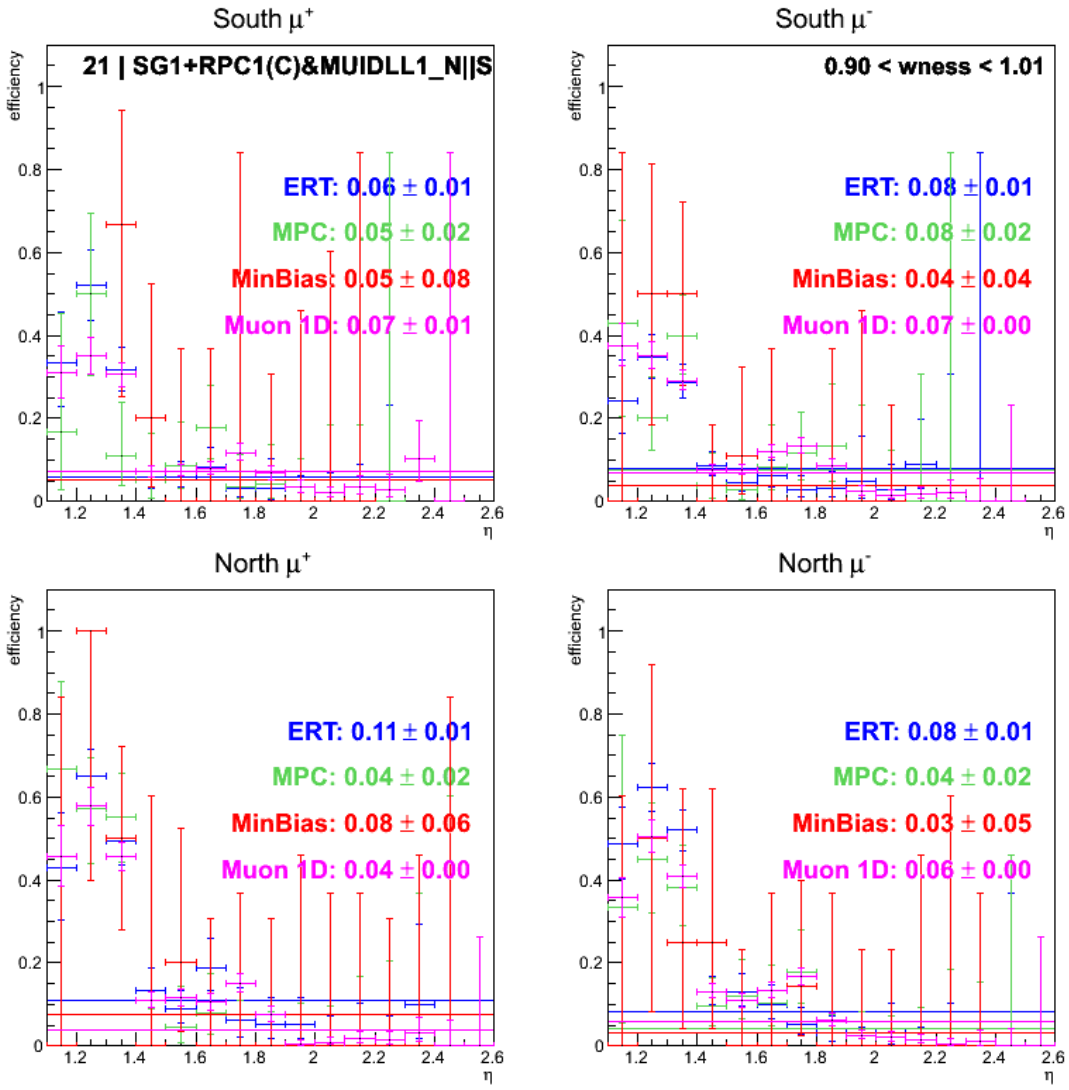

Figure 4.7: Taken from [29]. Trigger efficiency vs η as calculated compared to different reference triggers for **trigger bit 21 - (SG3&RPC3&MUID_1D_N||S)**. Muon candidate events with $p_T > 5$ are considered. For each reference trigger, ERT (Blue), MPC (green), MinBias or BBC (red) and MUID 1D (purple), the value of a constant fit is shown.

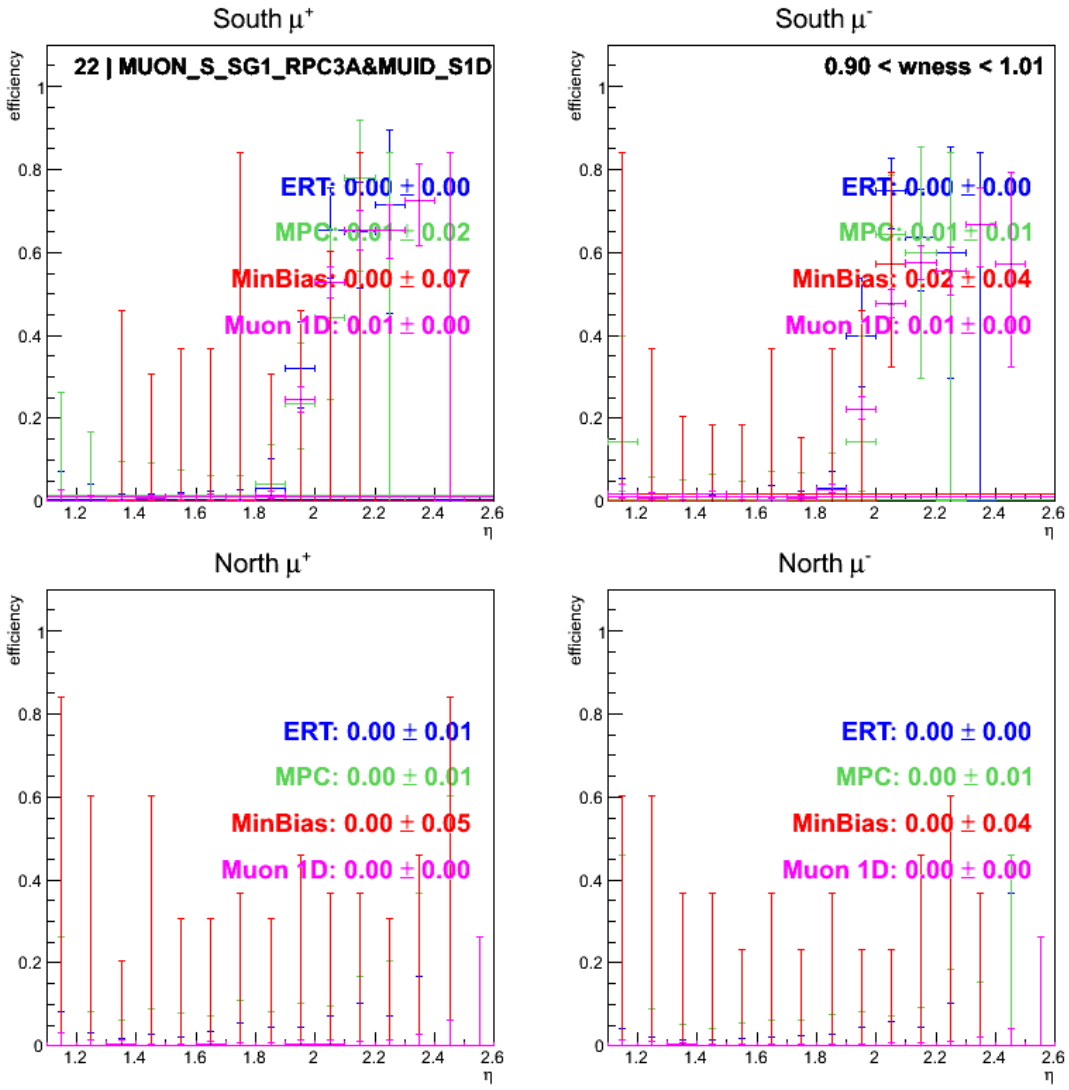

Figure 4.8: Taken from [29]. Trigger efficiency vs η as calculated compared to different reference triggers for **trigger bit 22 - (MUON_S_SG1_RPC3A&MUID_S1D)**. Muon candidate events with $p_T > 5$ are considered. For each reference trigger, ERT (Blue), MPC (green), MinBias or BBC (red) and MUID 1D (purple), the value of a constant fit is shown.

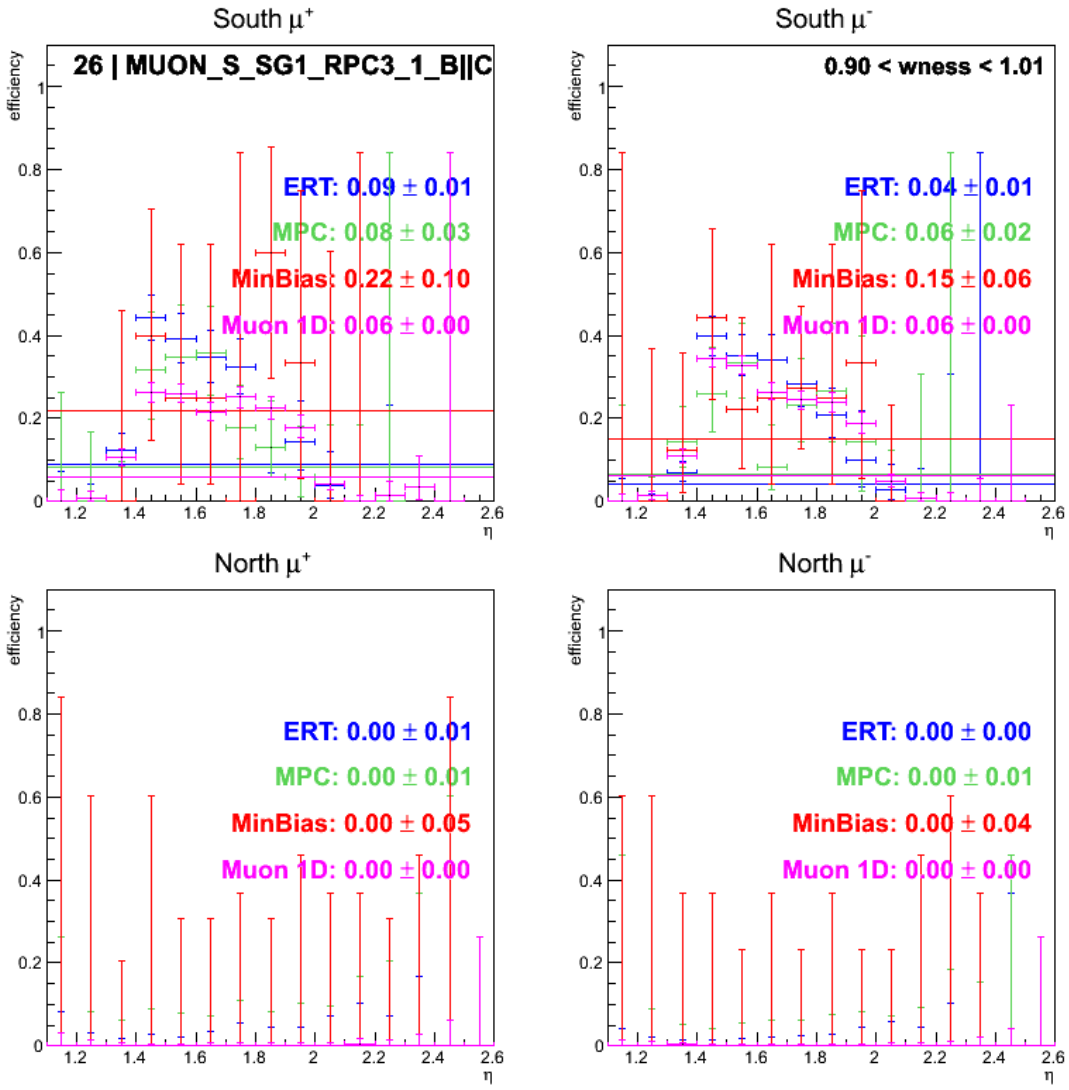

Figure 4.9: Taken from [29]. Trigger efficiency vs η as calculated compared to different reference triggers for **trigger bit 26 - (MUON_S_SG1_RPC3_1_B||C)**. Muon candidate events with $p_T > 5$ are considered. For each reference trigger, ERT (Blue), MPC (green), MinBias or BBC (red) and MUID 1D (purple), the value of a constant fit is shown.

The plots versus p_T include this function fit to each set of efficiencies. The plateau value of this function is higher than the calculated data points at high p_T but is still expected to be lower than the true trigger efficiency for real muon events due to "fake muon" dilution. The plateau value is then considered a lower bound for the true trigger efficiency for signal muons in the respective eta bin.

4.3.3 Trigger Efficiencies vs. W_{ness}

Trigger efficiency with respect to W_{ness} is also considered. Again, W_{ness} is a composite variable containing combined information from multiple kinimatic variables that is discussed in more detail later in section 5.1.1. These distributions are shown, again for trigger bit 20, in figures 4.13, 4.14, and 4.15 for the three bins in η. The W_{ness} data selection for these calculations includes a cut of $p_T > 5GeV$. In the case of efficiencies with respect to W_{ness}, the trend matches an expectation of efficiencies rising slightly with increasing W_{ness} in a roughly linear fashion. There is a statistical problem, however, that a majority of the events lie at very low values of W_{ness}. Because of this, a fairly coarse binning of only 6 bins between 0 and 1 are used. Because most of the statistics are in the lowest bin, but the higher W_{ness} bins are of greater interest, a linear fit is performed excluding the first bin to avoid its overweighted influence on the fit results. The plots are shown with the results of these linear fits and a final efficiency value is extrapolated using the fit result in a target W_{ness} region of $0.9 < W_{ness} < 1.0$.

4.3.4 Total Trigger Efficiencies

With efficiencies calculated for each trigger versus rapidity, and versus p_T and W_{ness} for three rapidity bins, the triggers can be combined to give a total trigger efficiency for the dataset. Considering only the η dependence, the total efficiency for one bin is calculated as a weighted average of each individual triggers efficiency (ϵ_{trig}) weighted by the fraction of events (f_{trig}) for that trigger within the bin:

$$\epsilon_{total} = \sum_{trig} \epsilon_{trig} f_{trig} \tag{4.5}$$

In this way, a total efficiency versus rapidity in fine bins can be generated that ignores (and thus averages over) p_T and W_{ness} dependence. To account for these dependencies as calculated in the previous subsections, the results of the respective p_T and W_{ness} fitting procedures in the course eta bins are used to scale the fine eta bins such that the average of the corresponding fine η bins match each course bin. This is done separately for p_T and W_{ness} and results are shown in figures 4.16 and 4.17.

A few observations from these results: first, as expected, the efficiency values are smaller when scaled

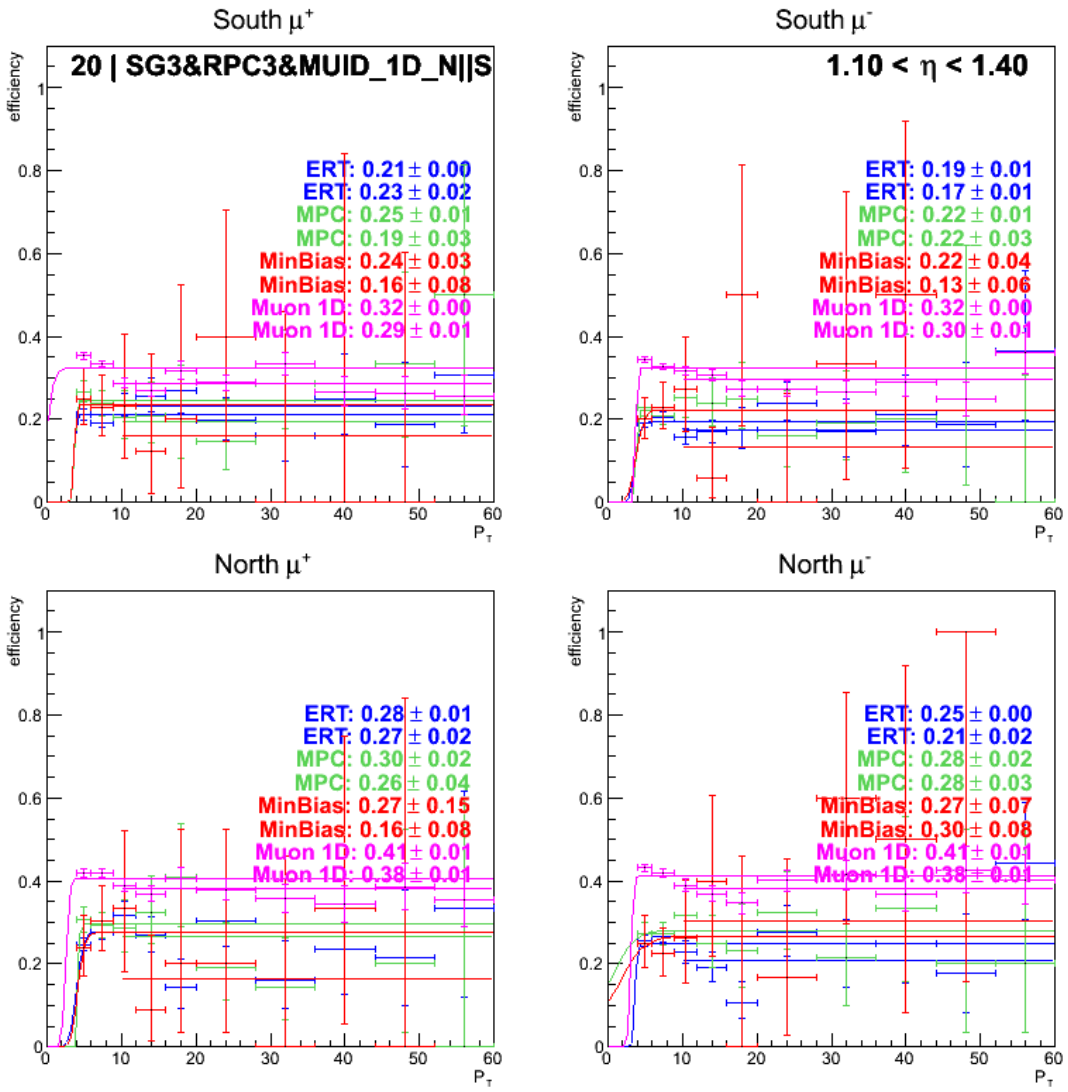

Figure 4.10: Taken from [29]. Trigger efficiency vs p_T as calculated compared to different reference triggers for trigger bit 20 - (SG3&RPC3&MUID_1D_N||S). Muon candidate events selected within the η **range:** $1.1 < \eta < 1.4$. The plateau value of the functional fit is listed for each reference trigger.

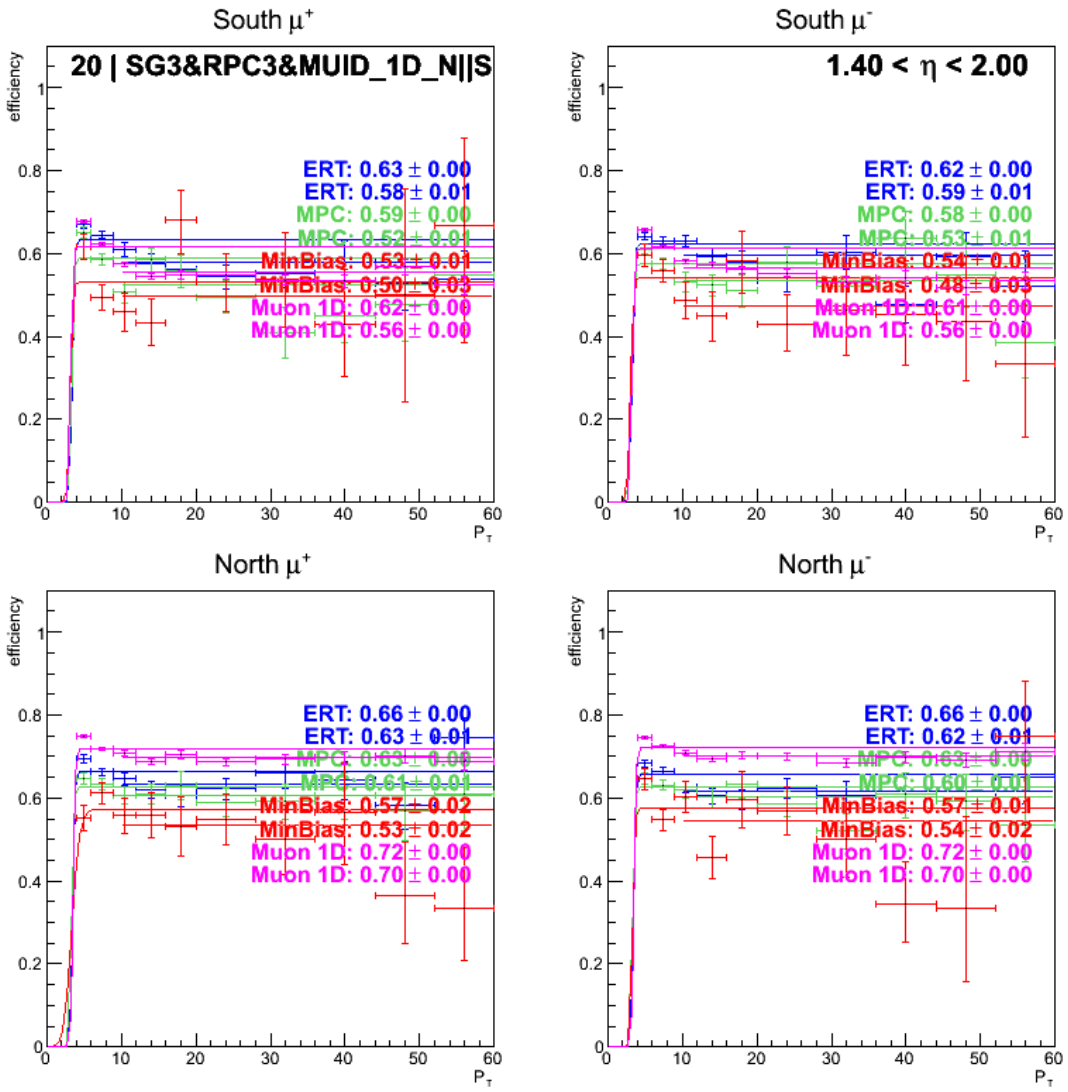

Figure 4.11: Taken from [29]. Trigger efficiency vs p_T as calculated compared to different reference triggers for trigger bit 20 - (SG3&RPC3&MUID_1D_N||S). Muon candidate events selected within the η **range:** $1.4 < \eta < 2.0$. The plateau value of the functional fit is listed for each reference trigger.

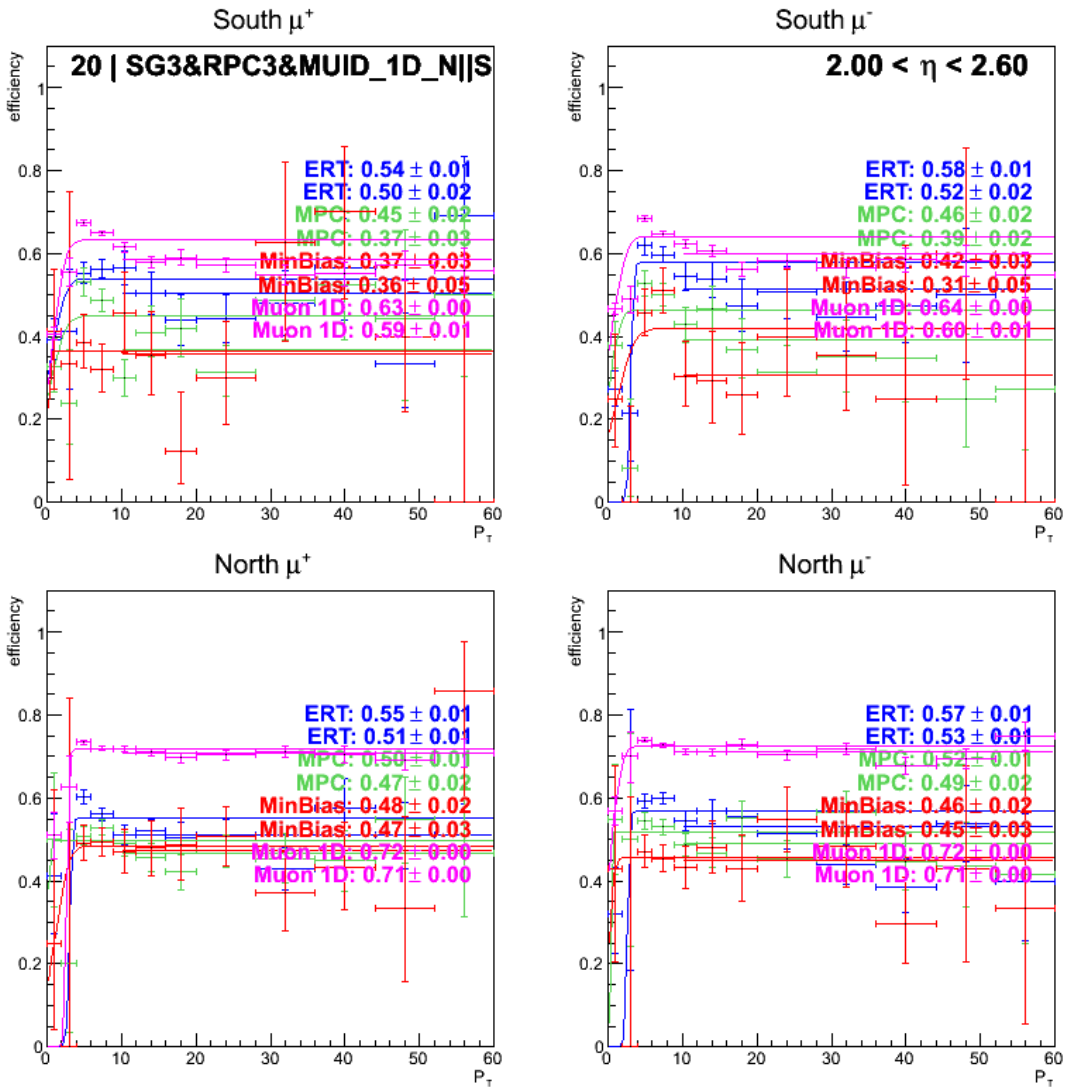

Figure 4.12: Taken from [29]. Trigger efficiency vs p_T as calculated compared to different reference triggers for trigger bit 20 - (SG3&RPC3&MUID_1D_N||S). Muon candidate events selected within the η **range:** $2.0 < \eta < 2.6$. The plateau value of the functional fit is listed for each reference trigger.

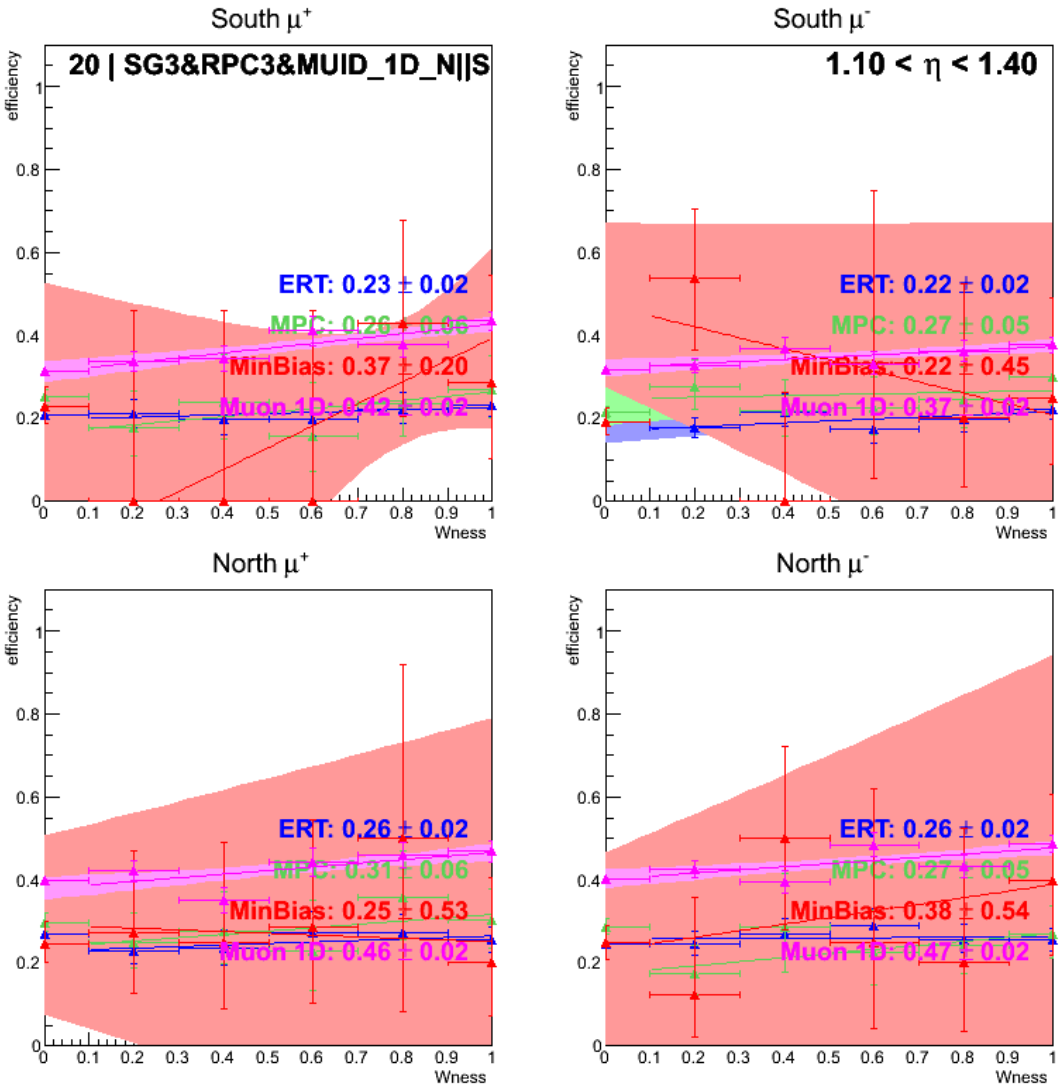

Figure 4.13: Taken from [29]. Trigger efficiency vs W_{ness} as calculated compared to different reference triggers for trigger bit 20 - (SG3&RPC3&MUID_1D_N||S). Muon candidate events selected within the η **range:** $1.1 < \eta < 1.4$ and with $p_T > 5GeV$. A linear fit is performed on the upper 5 W_{ness} bins and the values shown for each reference trigger are the extrapolation of this fit to the high W_{ness} region.

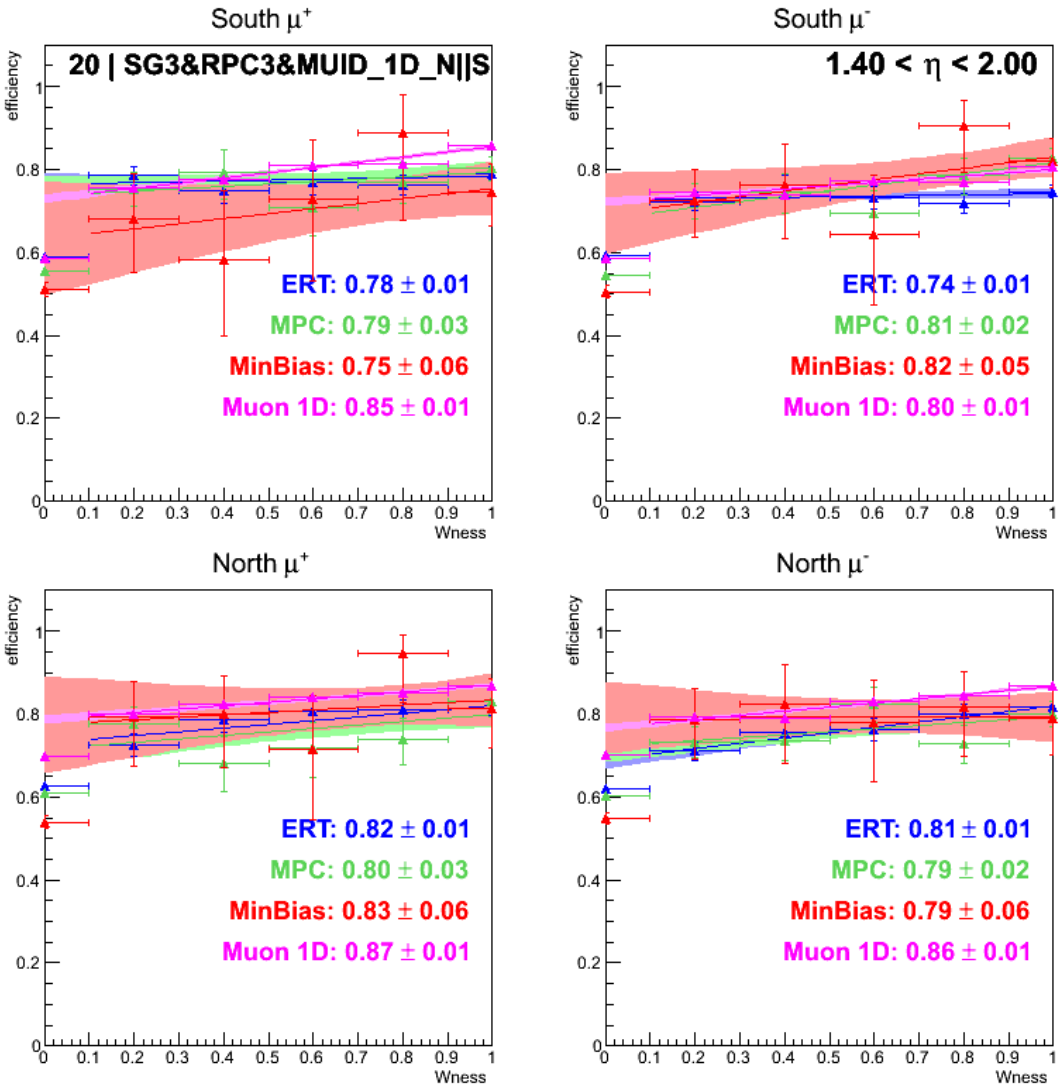

Figure 4.14: Taken from [29]. Trigger efficiency vs W_{ness} as calculated compared to different reference triggers for trigger bit 20 - (SG3&RPC3&MUID_1D_N||S). Muon candidate events selected within the η **range:** $1.4 < \eta < 2.0$ and with $p_T > 5GeV$. A linear fit is performed on the upper 5 W_{ness} bins and the values shown for each reference trigger are the extrapolation of this fit to the high W_{ness} region.

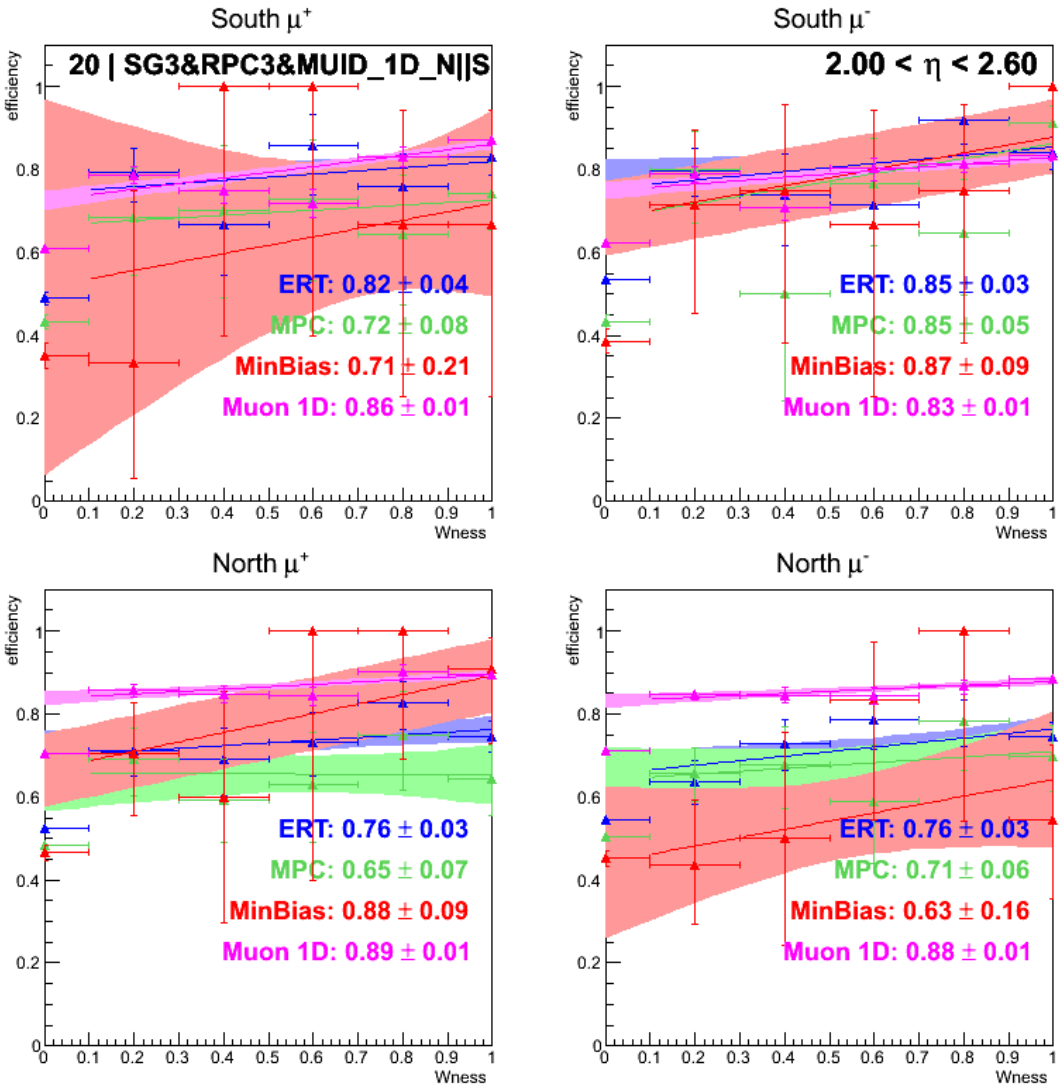

Figure 4.15: Taken from [29]. Trigger efficiency vs W_{ness} as calculated compared to different reference triggers for trigger bit 20 - (SG3&RPC3&MUID_1D_N||S). Muon candidate events selected within the η **range:** $2.0 < \eta < 2.6$ and with $p_T > 5GeV$. A linear fit is performed on the upper 5 W_{ness} bins and the values shown for each reference trigger are the extrapolation of this fit to the high W_{ness} region.

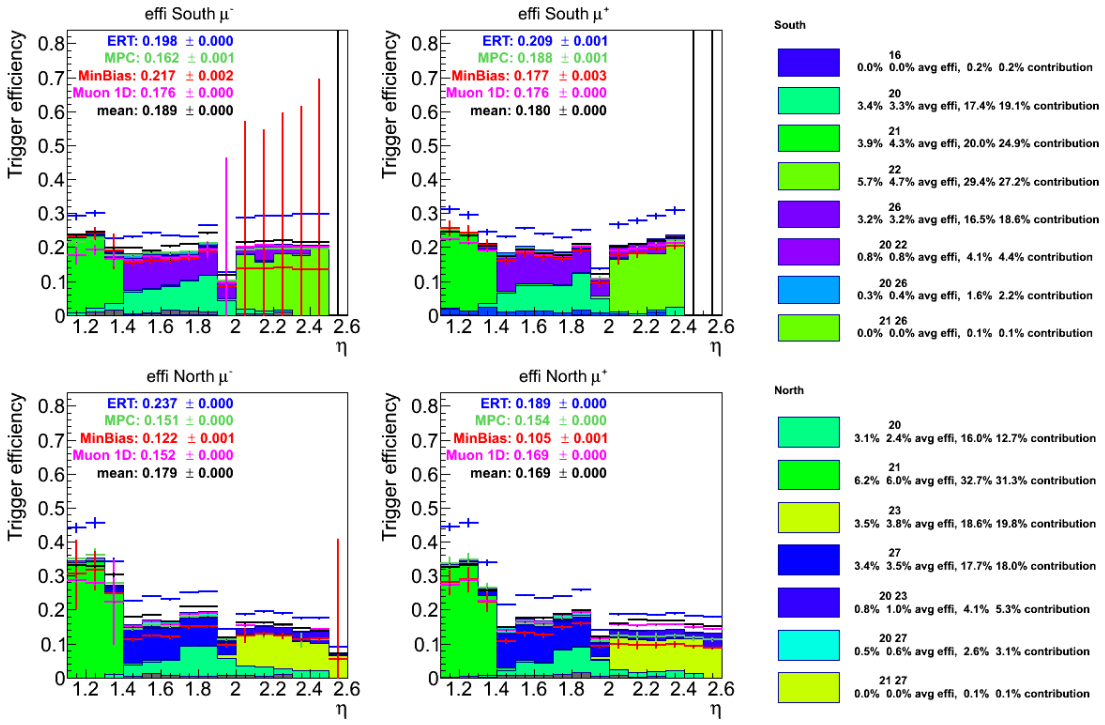

Figure 4.16: Taken from [29]. Total Trigger efficiency vs η. Different color data points with error bars are calculated compared to different reference triggers as labeled (with the average between them shown in black). The stacked histograms show the fractional contribution from each individual trigger with the largest contributing bits labeled in the legend. Efficiency values were scaled according to the course η bin p_T **fit plateau evaluation** discussed in section 4.3.2. For reference, table 4.4 lists triggers associated with each trigger bit and 4.3 describes their detector criteria.

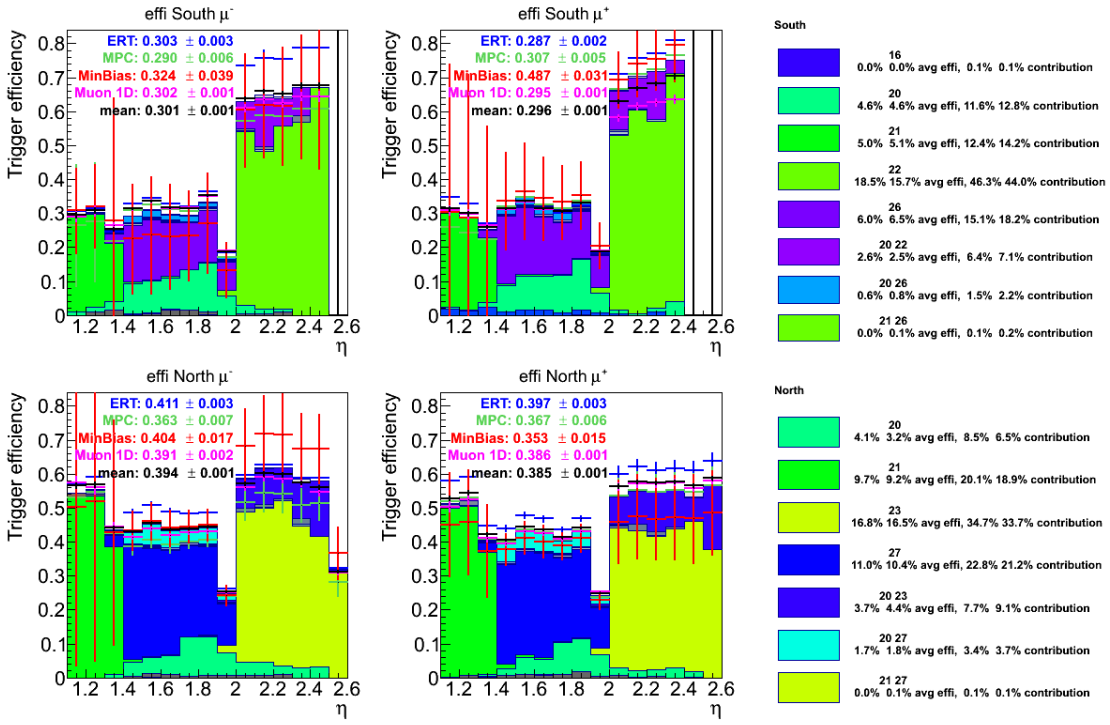

Figure 4.17: Taken from [29]. Total Trigger efficiency vs η. Different color data points with error bars are calculated compared to different reference triggers as labeled (with the average between them shown in black). The stacked histograms show the fractional contribution from each individual trigger with the largest contributing bits labeled in the legend. Efficiency values were scaled according to the course η bin W_{ness} **fit extrapolation evaluation** discussed in section 4.3.3. For reference, table 4.4 lists triggers associated with each trigger bit and 4.3 describes their detector criteria.

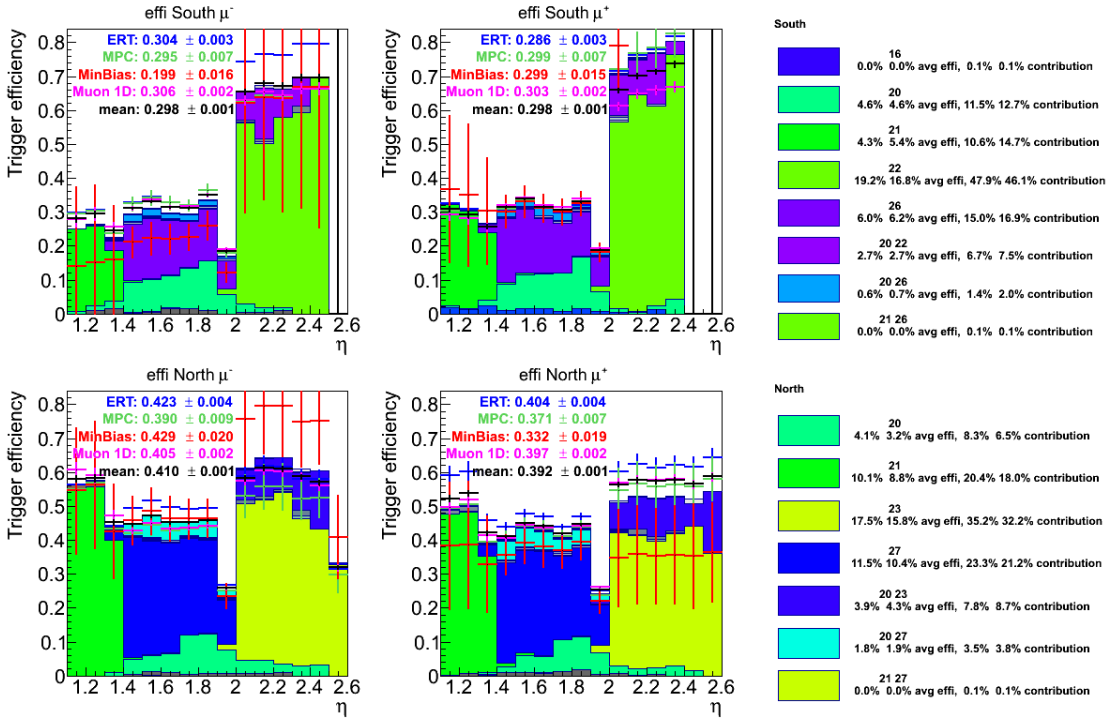

Figure 4.18: Taken from [29]. Total Trigger efficiency vs η. Different color data points with error bars are calculated compared to different reference triggers as labeled (with the average between them shown in black). The stacked histograms show the fractional contribution from each individual trigger with the largest contributing bits labeled in the legend. Efficiency values were scaled according to the course η bin **top W_{ness} bin evaluation** discussed in section 4.3.4. For reference, table 4.4 lists triggers associated with each trigger bit and 4.3 describes their detector criteria.

according to p_T than when scaled according to W_{ness}. As described, this is because of the high occurrence of "fake muons" at high p_T. The W_{ness} version is expected to more closely represent the true efficiency values, but the error bars are notably larger.

Other methods can be used to obtain W_{ness} scaling for the efficiencies however. Instead of using the high W_{ness} extrapolation of the linear fits of W_{ness} in each of the coarse η bins, the efficiency value of the highest W_{ness} bin can be used directly. This in principle should yield similar results to those in figure 4.17 and in fact, any variation is a useful indicator of systematic uncertainty in the trigger efficiency calculation. Results for this "highest W_{ness} bin" method are shown in figure 4.18.

All three total results shown so far rely on scaling according to values determined in the three coarse η bins. And it's clear there are discontinuity artifacts due to this around the bin boundaries ($\eta = 1.4, 2.0$). In an effort to avoid this, a third method is employed to scale according to the W_{ness} dependance of efficiencies. This time, values are calculated independently in the fine η bins (15 bins) but with a $W_{ness} > 0.92$ cut applied, which matches the W_{ness} region of interest in our analysis, and without the $p_T > 5GeV$ requirement. The

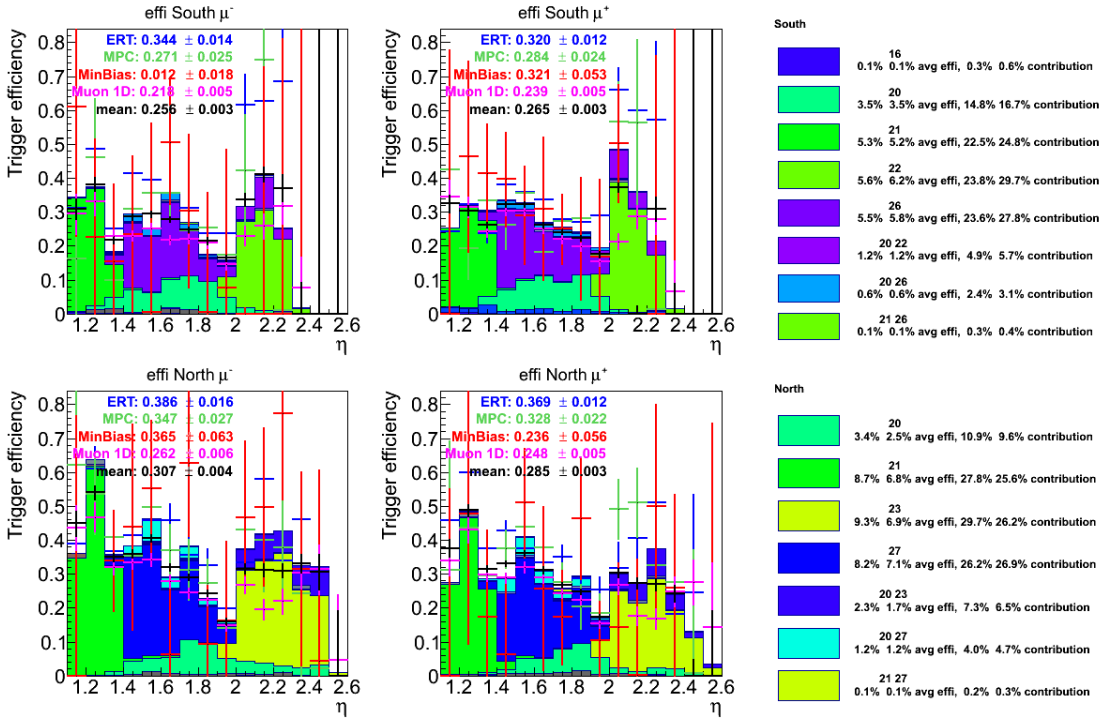

Figure 4.19: Taken from [29]. Total Trigger efficiency vs η. Different color data points with error bars are calculated compared to different reference triggers as labeled (with the average between them shown in black). The stacked histograms show the fractional contribution from each individual trigger with the largest contributing bits labeled in the legend. Efficiency values were scaled according to the course η bin **top W_{ness} bin evaluation** discussed in section 4.3.4. For reference, table 4.4 lists triggers associated with each trigger bit and 4.3 describes their detector criteria.

resulting efficiency from this method are shown in figure 4.19. The efficiency values are lower than other W_{ness} scaled methods (figs. 4.17, 4.18) due to the lower allowed p_T range, but not as low as the purely p_T based scaling (which, again, is considered a lower bound for efficiencies). Also, the uncertainties are high due to the limited statistics at high W_{ness}. But the shape and lack of discontinuities seems more reasonable.

In the end, the total efficiency values chosen for later stages of the analysis are those from the last $W_{ness} > 0.92$ method and the linear fit in W_{ness} extrapolation method as they are deemed most representative of true total trigger efficiencies. The final values for each eta range and for each arm and charge are listed for each of these methods are listed in tables 4.6 and 4.7. And again, the difference in results from some of the different techniques discussed in this section are ultimately used in estimating the systematic uncertainties associated with the trigger efficiencies. More about the use of these trigger efficiencies will be discussed in chapter 5.

η_{min}	η_{min}	μ^-	μ^+
South			
1.10	1.20	$0.296 \pm 0.008 \pm 0.035$	$0.314 \pm 0.007 \pm 0.056$
1.20	1.30	$0.310 \pm 0.008 \pm 0.038$	$0.300 \pm 0.007 \pm 0.057$
1.30	1.40	$0.254 \pm 0.006 \pm 0.038$	$0.260 \pm 0.005 \pm 0.037$
1.40	1.50	$0.315 \pm 0.002 \pm 0.091$	$0.313 \pm 0.002 \pm 0.002$
1.50	1.60	$0.336 \pm 0.003 \pm 0.099$	$0.338 \pm 0.002 \pm 0.004$
1.60	1.70	$0.318 \pm 0.002 \pm 0.087$	$0.315 \pm 0.002 \pm 0.004$
1.70	1.80	$0.315 \pm 0.002 \pm 0.082$	$0.306 \pm 0.002 \pm 0.005$
1.80	1.90	$0.353 \pm 0.002 \pm 0.082$	$0.330 \pm 0.002 \pm 0.008$
1.90	2.00	$0.186 \pm 0.001 \pm 0.053$	$0.188 \pm 0.001 \pm 0.005$
2.00	2.10	$0.637 \pm 0.007 \pm 0.068$	$0.629 \pm 0.006 \pm 0.057$
2.10	2.20	$0.660 \pm 0.006 \pm 0.076$	$0.668 \pm 0.007 \pm 0.062$
2.20	2.30	$0.653 \pm 0.007 \pm 0.071$	$0.682 \pm 0.006 \pm 0.063$
2.30	2.40	$0.676 \pm 0.008 \pm 0.071$	$0.704 \pm 0.007 \pm 0.075$
2.40	2.50	$0.676 \pm 0.009 \pm 0.071$	$0.000 \pm 1.000 \pm 0.000$
2.50	2.60	$0.000 \pm 1.000 \pm 0.000$	$0.000 \pm 1.000 \pm 0.000$
North			
1.10	1.20	$0.566 \pm 0.008 \pm 0.066$	$0.528 \pm 0.007 \pm 0.078$
1.20	1.30	$0.568 \pm 0.009 \pm 0.051$	$0.545 \pm 0.007 \pm 0.087$
1.30	1.40	$0.441 \pm 0.006 \pm 0.020$	$0.421 \pm 0.005 \pm 0.048$
1.40	1.50	$0.430 \pm 0.003 \pm 0.047$	$0.406 \pm 0.003 \pm 0.029$
1.50	1.60	$0.454 \pm 0.003 \pm 0.050$	$0.444 \pm 0.003 \pm 0.033$
1.60	1.70	$0.436 \pm 0.003 \pm 0.048$	$0.436 \pm 0.003 \pm 0.035$
1.70	1.80	$0.440 \pm 0.003 \pm 0.042$	$0.415 \pm 0.002 \pm 0.027$
1.80	1.90	$0.444 \pm 0.003 \pm 0.041$	$0.440 \pm 0.002 \pm 0.030$
1.90	2.00	$0.252 \pm 0.002 \pm 0.015$	$0.249 \pm 0.001 \pm 0.021$
2.00	2.10	$0.571 \pm 0.006 \pm 0.056$	$0.564 \pm 0.006 \pm 0.105$
2.10	2.20	$0.601 \pm 0.006 \pm 0.060$	$0.577 \pm 0.006 \pm 0.103$
2.20	2.30	$0.598 \pm 0.007 \pm 0.057$	$0.573 \pm 0.006 \pm 0.106$
2.30	2.40	$0.575 \pm 0.006 \pm 0.067$	$0.578 \pm 0.006 \pm 0.106$
2.40	2.50	$0.559 \pm 0.006 \pm 0.049$	$0.566 \pm 0.006 \pm 0.098$
2.50	2.60	$0.313 \pm 0.004 \pm 0.033$	$0.589 \pm 0.006 \pm 0.103$

Table 4.6: Taken from [29]. Total trigger efficiencies for the W candidate sample per arm and charge as a function of rapidity including statistical and systematic uncertainties based on the extrapolation to high wness in a coarse rapidity binning.

η_{min}	η_{min}	μ^-	μ^+
South			
1.10	1.20	$0.309 \pm 0.031 \pm 0.147$	$0.324 \pm 0.028 \pm 0.324$
1.20	1.30	$0.382 \pm 0.021 \pm 0.172$	$0.304 \pm 0.015 \pm 0.112$
1.30	1.40	$0.217 \pm 0.010 \pm 0.123$	$0.262 \pm 0.008 \pm 0.025$
1.40	1.50	$0.286 \pm 0.009 \pm 0.064$	$0.324 \pm 0.008 \pm 0.063$
1.50	1.60	$0.294 \pm 0.010 \pm 0.291$	$0.324 \pm 0.008 \pm 0.036$
1.60	1.70	$0.280 \pm 0.008 \pm 0.072$	$0.262 \pm 0.007 \pm 0.096$
1.70	1.80	$0.248 \pm 0.008 \pm 0.073$	$0.240 \pm 0.007 \pm 0.069$
1.80	1.90	$0.215 \pm 0.010 \pm 0.251$	$0.224 \pm 0.008 \pm 0.109$
1.90	2.00	$0.165 \pm 0.010 \pm 0.091$	$0.176 \pm 0.010 \pm 0.026$
2.00	2.10	$0.336 \pm 0.020 \pm 0.451$	$0.373 \pm 0.014 \pm 0.302$
2.10	2.20	$0.411 \pm 0.023 \pm 0.481$	$0.000 \pm 0.023 \pm 0.668$
2.20	2.30	$0.370 \pm 0.040 \pm 0.466$	$0.309 \pm 0.035 \pm 0.484$
2.30	2.40	$0.000 \pm 0.092 \pm 0.676$	$0.000 \pm 0.092 \pm 0.704$
2.40	2.50	$0.000 \pm 1.000 \pm 0.676$	$0.000 \pm 1.000 \pm 0.000$
2.50	2.60	$0.000 \pm 1.000 \pm 0.000$	$0.000 \pm 1.000 \pm 0.000$
North			
1.10	1.20	$0.449 \pm 0.037 \pm 0.464$	$0.377 \pm 0.026 \pm 0.406$
1.20	1.30	$0.541 \pm 0.021 \pm 0.079$	$0.488 \pm 0.018 \pm 0.082$
1.30	1.40	$0.349 \pm 0.011 \pm 0.096$	$0.316 \pm 0.010 \pm 0.177$
1.40	1.50	$0.359 \pm 0.012 \pm 0.075$	$0.330 \pm 0.008 \pm 0.279$
1.50	1.60	$0.405 \pm 0.011 \pm 0.079$	$0.362 \pm 0.009 \pm 0.093$
1.60	1.70	$0.320 \pm 0.011 \pm 0.281$	$0.311 \pm 0.010 \pm 0.136$
1.70	1.80	$0.290 \pm 0.011 \pm 0.157$	$0.268 \pm 0.008 \pm 0.175$
1.80	1.90	$0.243 \pm 0.010 \pm 0.250$	$0.247 \pm 0.009 \pm 0.198$
1.90	2.00	$0.160 \pm 0.010 \pm 0.095$	$0.173 \pm 0.008 \pm 0.103$
2.00	2.10	$0.316 \pm 0.015 \pm 0.260$	$0.303 \pm 0.014 \pm 0.307$
2.10	2.20	$0.312 \pm 0.019 \pm 0.311$	$0.273 \pm 0.016 \pm 0.407$
2.20	2.30	$0.310 \pm 0.021 \pm 0.302$	$0.269 \pm 0.019 \pm 0.321$
2.30	2.40	$0.331 \pm 0.028 \pm 0.259$	$0.242 \pm 0.025 \pm 0.341$
2.40	2.50	$0.306 \pm 0.051 \pm 0.381$	$0.000 \pm 0.048 \pm 0.566$
2.50	2.60	$0.000 \pm 0.193 \pm 0.313$	$0.000 \pm 0.192 \pm 0.589$

Table 4.7: Taken from [29]. Total trigger efficiencies for the W candidate sample per arm and charge as a function of rapidity including statistical and systematic uncertainties based on the fine rapidity binning at high W_{ness}.

4.4 Simulations

Existing knowledge of collision interactions can be leveraged to build an understanding of what to expect from our data. Simulated proton collisions and various resulting subprocesses can be used to estimate both kinematic distributions and detector responses within PHENIX. Extensive simulations were done during the development of this measurement to identify and estimate levels of prominent sources of background [28]. And further simulations were used in more detail in the analysis process to filter background and extract the final signal yield (This will be discussed in Ch. 5). The work of generating these simulations was done primarily by Ralf Seidl. The remainder of this section summarizes simulations and what they say about the composition of our dataset.

These simulations were done using PISA and PYTHIA (version 6.4). PYTHIA [42], is software suite that encodes a wide array of particle physics knowledge. It contains models used to generate particle events and propagate extensive sets of subsequent interactions according either analytically known behavior, or according to measured distributions if a certain process is not fully understood. PISA, the PHENIX Integrated Simulation Application, is a software framework that contains detailed geometric and material descriptions of the PHENIX apparatus contained in the collision room. These packages are used together to generate events, propagate their physical interactions in the experiment and ultimately simulate the response as seen by PHENIX detectors. Some detail of each of the underlying processes simulated is listed below.

4.4.1 Signal and Background Muons

Figure 4.20, shows the cross section of various sources of simulated real muons as a function of transverse momentum (p_T). The top plots show each source as labeled individually and the bottom plots show the sources stacked. These plots show the cross section of generated muon events according to their true p_T, without accounting for momentum smearing due to detector resolution. As can be seen, signal muons from W are dominant in the signal region of $16 < p_T < 60$, with moderate contribution from Z sources. When momentum smearing is taken into account however, background sources with a larger presence at low p_T are smeared into the target region (a problem which will prove even more significant for hadronic background).

4.4.2 Hadronic Background

As described in section 4.1.4, hadronic background consists mainly of hadrons decaying within the tracker volume. Figure 4.21 shows the cross section of various sources of simulated hadronic backgrounds as a function of transverse momentum (p_T) alongside the simulated muons from figure 4.20 for comparison. As

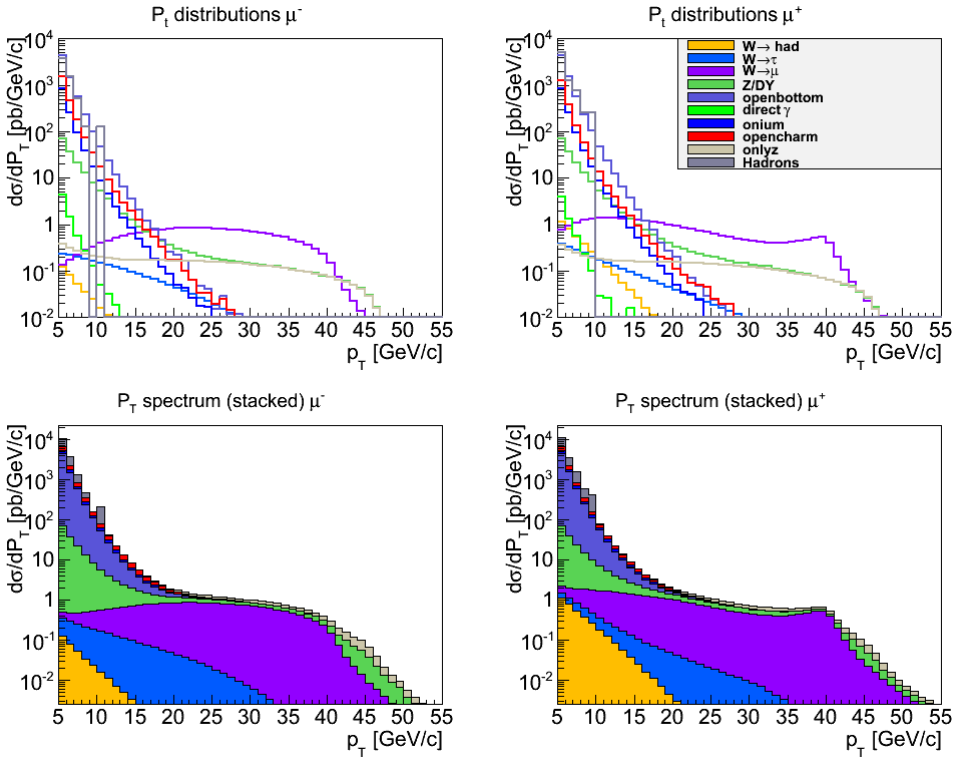

Figure 4.20: Top plots: Real muon cross sections for positive (left) and negative (right) muons as a function of p_T for the individual subprocesses. Bottom plots: Stacked cross sections of all subprocesses for positive (left) and negative (right) muons as a function of p_T.

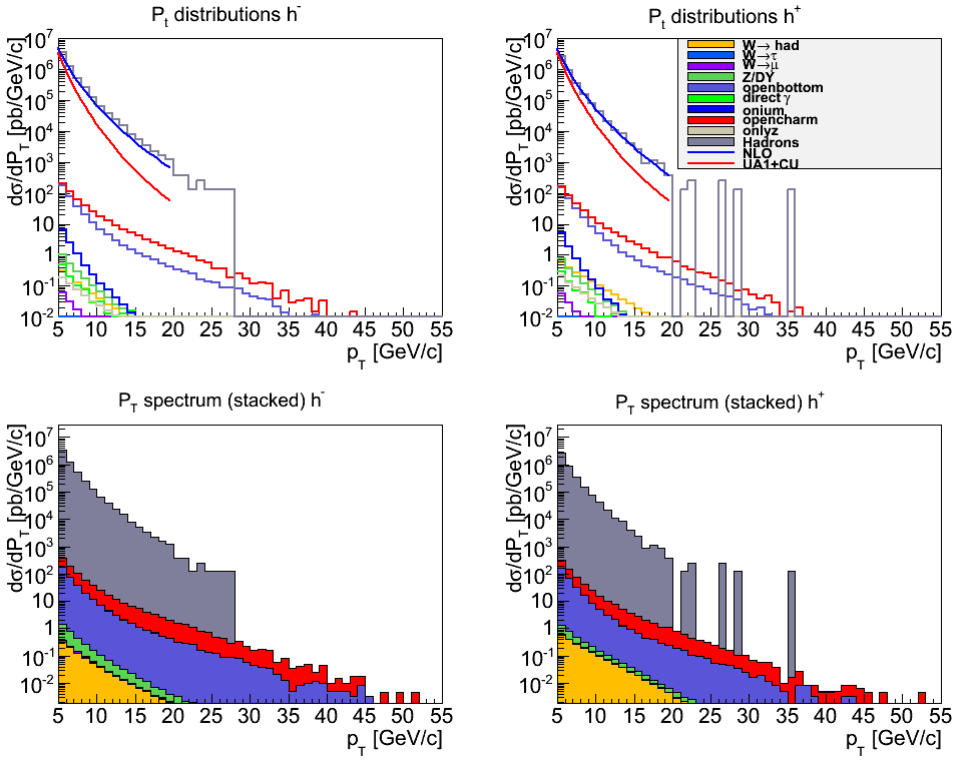

Figure 4.21: Top plots: Hadronic cross sections for positive (left) and negative (right)hadrons as a function of p_T for the sum of charged pions and kaons shown for individual subprocesses. Bottom plots: Stacked cross sections of all subprocesses for positive (left) and negative (right) hadrons as a function of p_T.

before, this is the cross section for true generated p_T without considering smearing. Notice that though the hadronic background falls off even more sharply with increasing p_T, the cross section is very large at low p_T. Once smearing is accounted for, this will prove the dominant background.

4.4.3 Combined Results

Events are generated for each of the above listed process categories and run through the PHENIX geometry with variations due to detector resolution taken in to account. The subprocesses are then scaled according to generated events and known process cross sections to match the dataset luminosity and added together. The resulting stacked distribution of events vs p_T is shown in figure 4.22 for each arm and muon charge combination. These simulations will be used to model data components in various steps of the analysis as described in chapter 5.

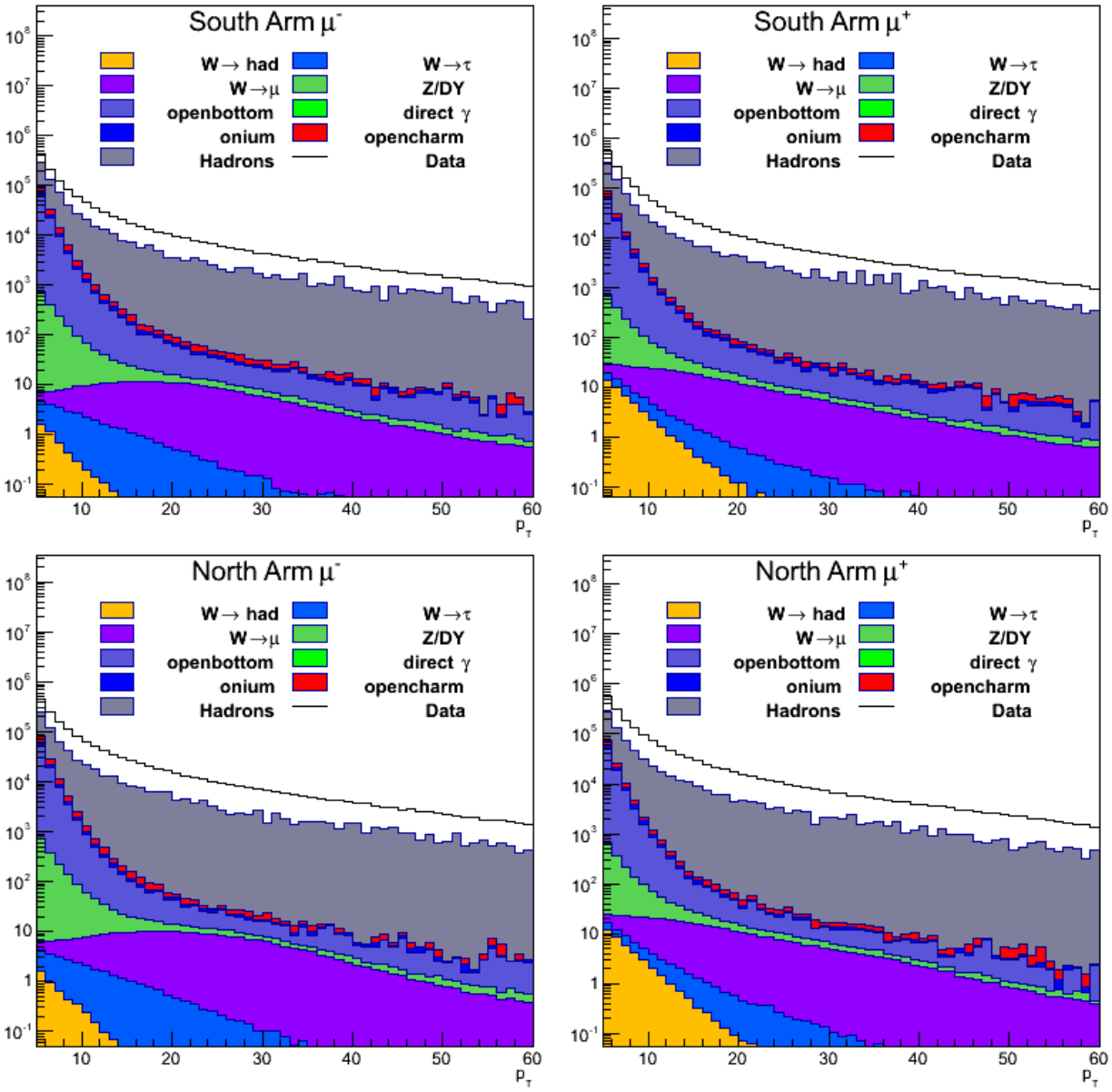

Figure 4.22: Stacked, hadronic cross sections for positive (left) and negative (right) muons as a function of the reconstructed p_T using basic cuts for the separate subprocesses created with Pythia + PISA as well as hadronic background as described in the text. The top panel displays the north muon arm, the bottom panel the south muon arm. The luminosity normalized data yields are also displayed for all contributing run 11 muon triggers.

4.5 Cosmic Data

In addition to pp collision data, a small set of cosmic muon events has been collected with the PHENIX detectors. This consists of data taken where the forward arm detectors and PHENIX Magnets are fully functioning, but RHIC is not colliding the beams. The purpose of this cosmic data is two fold: 1) to determine the cosmic ray background contribution to the A_L^W measurement(which is confirmed to be negligible [43] , and 2) to provide a data-driven measurement of p_T smearing and charge reconstruction efficiency.

The second point is of particular interest. As discussed previously, the W signal is dominant at high p_T but dominant background from low p_T is "smeared" to high p_T due to limited momentum resolution of the MuTr. Also, the charge of a reconstructed track is determined by the direction of bending in the magnetic field but, again due to limited resolution, a certain percentage of tracks are mis-identified as the wrong charge. These effects both have a significant impact on the analysis and final result. And both effects should be accounted for in the simulations. But because of their significance, a data-driven measurement is necessary to confirm the accuracy of how the effects are modeled in the simulations.

The following subsections will summarize p_T smearing and charge reconstruction results from the analysis of cosmic data taken in 2011. A full report of this analysis can be found in reference [43].

4.5.1 p_T Smearing

The strategy to extract the average p_T smearing (Δp_T) is to look at cosmic muons that travel through both forward arms. Any difference in reconstructed p_T between the arms (aside from a predicable, fixed energy loss associated with the muon traversing the PHENIX central magnet material) then is an indicator of smearing. The distribution of this difference in p_T (Δp_T) for all two-arm cosmic events from 2011 is shown in figure 4.23.

To compare the measured smearing with simulation, a dedicated set of cosmic events were generated and run through the PHENIX PISA simulation. The results are shown in figures 4.24 and 4.25 where, for positive and negative muons respectively, the width of the Δp_T distribution ($\sigma\Delta p_T$) is shown as a function of p_T for both simulated and measured values. These plots show that the cosmic data and simulations largely agree, with perhaps some statistically significant discrepancy in the higher p_T range of the negative muons. This consistency serves as confirmation of the validity of our simulations.

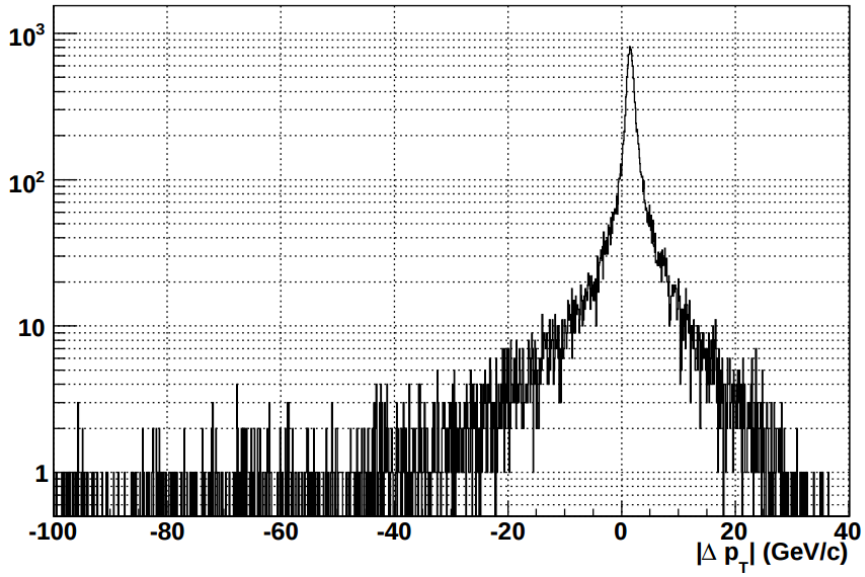

Figure 4.23: Taken from [43]. Distribution of difference in reconstructed p_T between arms in all two-arm cosmic events from the 2011 cosmic dataset.

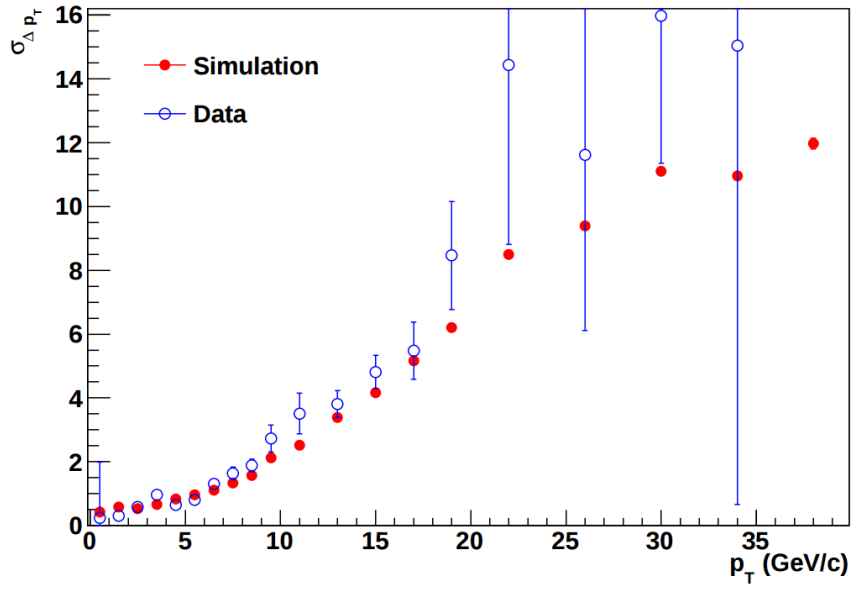

Figure 4.24: Taken from [43]. p_T smearing ($\Delta\sigma p_T$) as a function of p_T for **positive** muons. Measured results from cosmic data (blue) are compared with simulation (red).

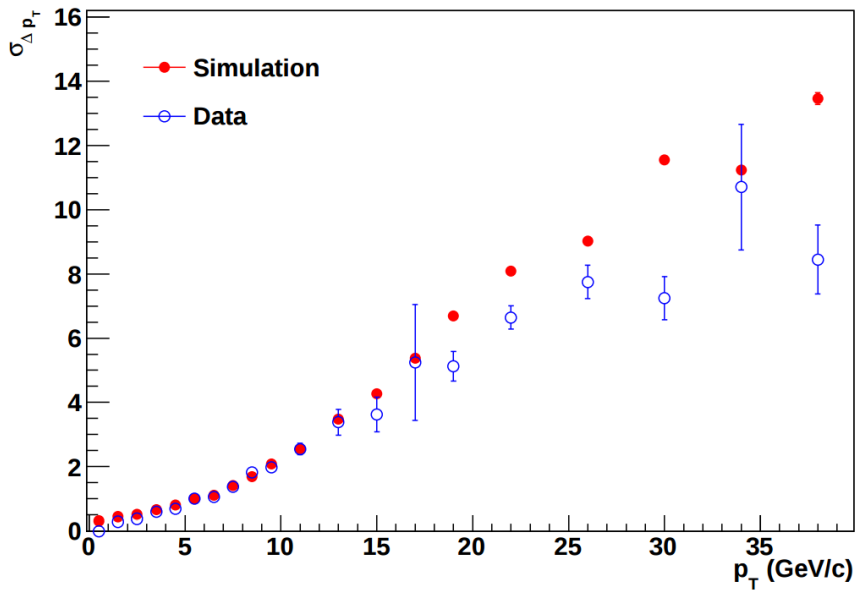

Figure 4.25: Taken from [43]. p_T smearing ($\Delta\sigma p_T$) as a function of p_T for **negative** muons. Measured results from cosmic data (blue) are compared with simulation (red).

4.5.2 Charge Reconstruction Efficiency

Charge reconstruction efficiency (CRE), again, is the rate at which the charge of particle is correctly identified from its reconstructed track (1 - CRE then is the rate of misidentification). The technique for measuring CRE with the cosmic data is very similar to the p_T smearing strategy: cosmic muons that go through both arms are selected and the charge determined by the reconstructed track is compared between the arms. Again, a simulation of cosmic muon events propagated through the PHENIX PISA simulation is compared with the results from the cosmic data.

Figures 4.26 (for μ^+), and 4.27 (for μ^-) show the comparison of these results. As expected, the efficiency trends downward with increasing p_T in both cases (higher momentum tracks have less bending in the magnetic field and thus a less distinct charge indicator). In the negative case, the simulation and cosmic data very closely agree. In the positive case, there is a discrepancy in the high p_T range where the cosmic data measured CRE falls below the simulated values. This discrepancy is not fully understood and because of it, the final A_L^W measurement is calculated with varying values of CRE and the resulting variation in A_L^W is included as a systematic uncertainty.

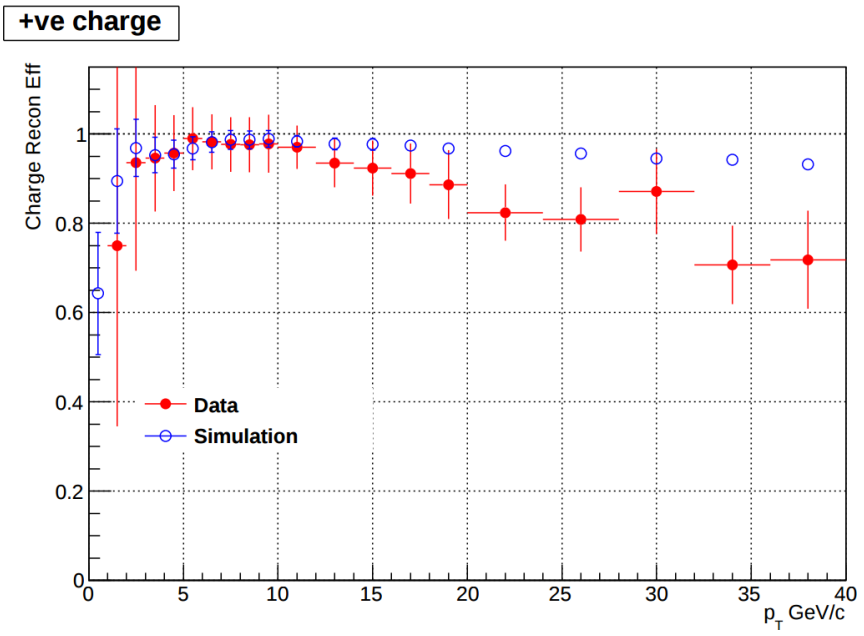

Figure 4.26: Taken from [43]. Charge reconstruction efficiency as a function of p_T for **positive** muons. Measured results from cosmic data (red) are compared with simulation (blue).

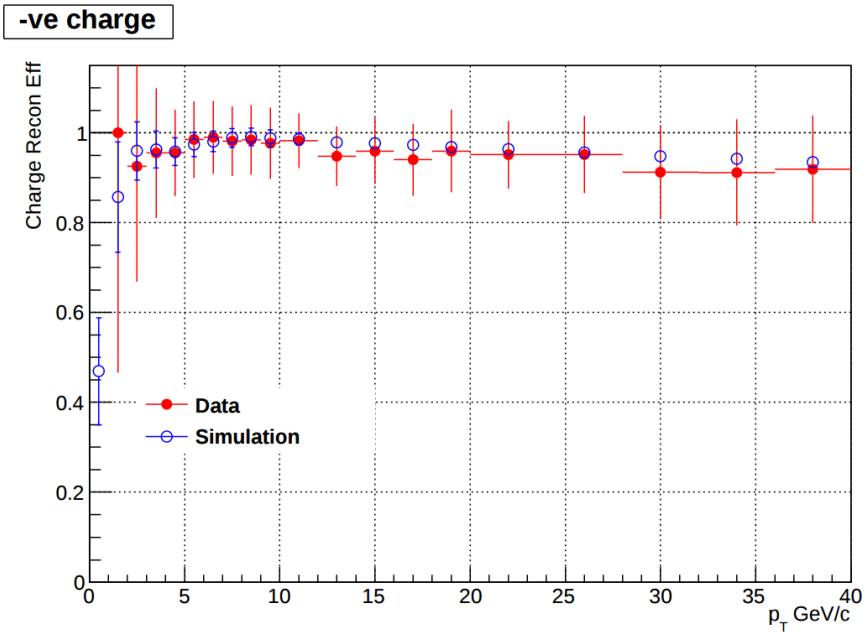

Figure 4.27: Taken from [43]. Charge reconstruction efficiency as a function of p_T for **negative** muons. Measured results from cosmic data (red) are compared with simulation (blue).

Chapter 5

A_L^W Analysis

As described in chapter 2, the measurment of interest is the single spin asymmetry in W boson production, A_L^W, from polarized pp collisions. And again, section 2.2 details how this asymmetry relates to the spin dependant quark and antiquark distributions. This chapter will present the strategy used to the extract a value for A_L^W from the 2013 dataset described in chapter 4.

To ultimately calculate A_L^W one needs to count the yields of signal $W \rightarrow \mu$ events relative to each permutation of beam helicities (this is more specifically described in section 5.2). The directly observed yield of events in our dataset, however, includes signal events diluted by background events. In fact, as described in section 4.1.4 and 4.4, background processes dominate signal events in our dataset by a factor of ¿ 200. The primary challenge of this analysis then is to filter out as much background as possible and then to accurately characterize the remaining yield of background and signal events in order to calculate A_L^W. The analysis strategy to accomplish this falls in to two basic steps each with two parts:

1. **Signal Yield Extraction**

   (a) **Event Preselection** - Use a likelihood ratio technique to statistically distinguish between signal-like and background-like events and select a subset of events with more signal concentration.

   (b) **Signal to Background Ratio** - Determine the ratio of signal and background events (and thus determine the signal yield) in the selected data by comparing distributions from simulation for each component.

2. **Single Spin Asymmetry Calculation**

   (a) **Raw Asymmetry** - Calculate the single-spin asymmetry of yields according event-level beam spin configurations.

   (b) **Scaling Factors** - Use polarization percentages, efficiencies and background dilution factors to scale the raw asymmetries to obtain the final values for this measurement.

The following sections will detail each of these steps and discuss further tests and validation.

5.1 Signal Yield Extraction

5.1.1 Event Preselection

The first step in the analysis is to select a subset of data with a higher percentage of signal content. This is desirable because it's difficult to precisely identify the yield of signal events when they are dominated by background. Once a subset is chosen with a more comperable proportion of signal and background event, however, the procedure in 5.1.2 can be followed to characterize the signal yield.

This reduced dataset is selected by calculating a "likelihood ratio" for each event and applying a cut. The ratio is a way to quantitatively contrast signal and background events. The concept is as follows: Events stemming from different underlying processes have, on average, different kinematic signatures; meaning there are distinct differences in the distribution of values observed for the properties of reconstructed tracks (here these properties refer to the kinematic variables listed in section 4.2.2). In many particle physics measurements, the difference is distributions are so distinct that signal events produce a Jacobian peak that allows straightforward fitting of a signal curve on top of a background curve. The Jacobian peak is suppressed in this dataset because of a high rate of background events relative to signal, and because there are only subtle differences in the kinematic distributions and limited resolution with which to resolve those differences. To address this limitation, the differences arising in several kinematic distributions are used simultaneously to increase distinguishing power.

The variables chosen as input for the likelihood ratio are listed in table 5.1. This set of variables was chosen from the set of all possible kinematic variables to maximize the distinguishing power offered by each variable, while minimizing the correlation between the group of variables. It's desirable to avoid correlation because two highly correlated variables offer little additional information together than just one of them alone. Further, the same information coming from two variables would over-weight that information relative to information coming form other uncorrelated variables causing a bias. Figure 5.1 shows the relative correlation of each of the selected variables separately among events in the data and events from the signal muon simulation. There is very little correlation between the variables.

Name	(Unit) Description
χ^2	The result of the Kalman fitter reconstructing the track
DG0	(cm) A Track matching variable (matching between MuID and MuTR) associated with the MuID road, at MuID station 3.
DDG0	(degree) The opening angle between the MuID track road, and the MuTr projection onto the MuID
DCA_r	(cm) Distance of closest approach between the track and beam axis
Rpc1dca	Distance of closest approach between projected MuTR track onto the RPC 1 and the closest hit cluster on RPC 1
Rpc3dca	Distance of closest approach between projected MuTR track onto the RPC 3 and the closest hit cluster on RPC 3
$fvtx_{d\phi}$	The ϕ residual between MuTR track and FVTX track
$fvtx_{d\theta}$	The θ residual between the MuTR track and FVTX track
$fvtx_{dr}$	The radial residual between the MuTR track and the FVTX track
$fvtx_{conebits}$	The number of FVTX clusters inside a cone around the track defined by: $0.04rad < dR < 0.52rad$ where $dR = \sqrt{d\eta^2 + d\phi^2}$

Table 5.1: Description of event level variables used in the likelihood ratio calculation.

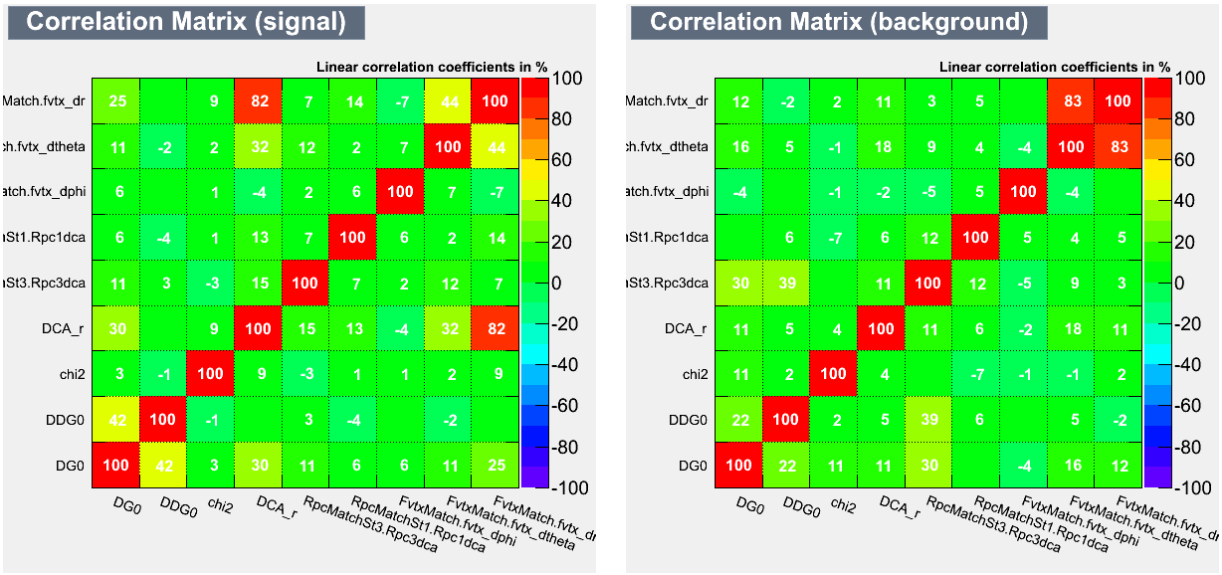

(a) Simulated W Boson μ events

(b) Real data proxy for hadronic background

Figure 5.1: Taken from [32]. In panel (a) Correlations are shown between kinematic variables, produced from the signal simulation. In panel (b) correlations are shown for the real data proxy for hadronic background. Variables that are correlated are combined in two dimensional probability distribution functions, i.e. DG0 and DDG0 and DCA_r and χ^2.

Once the variables are chosen, the expected distributions for signal events and background events must me modeled separately. The simulations described in section 4.4 are used to model signal events. And the background is roughly modeled by the dataset itself. At this point, this is a reasonable approximation

because even after the basic cuts background events dominate signal events by roughly a factor of 100 (though the background will have to be modeled more closely in section 5.1.2). Histograms are produced of event yields with respect to each variable from the simulated data and real dataset, respectively. Then, each distribution is separately normalized to effectively become a probability density(PDF) for the events with respect to that variable. These PDF's, $p_i(x_i)$ for each variable x_i, will be the input used to calculate the likelihood ratio (and exist separately for signal(modeled by simulation) and background(modeled by the dataset)).

Next, a "likelihood distribution", λ, can then be constructed as the product of the PDF for each of the variables:

$$\lambda(x_1, x_2, \cdots, x_n) = p_1(x_1)p_2(x_2)\cdots p_n(x_n) \tag{5.1}$$

where $\lambda(\cdots)$ is the likelihood as a function of the n kinematic variables $x_1 \cdots x_n$, each with a normalized distribution $p_i(x_i)$. Again, λ is composed separately for signal events (λ_{sig}) and background events (λ_{bkg}). These likelihoods then are distributions that range between 0 and 1 and represent how "average" the kinematic values for a given event are compared with the kinematic distributions between all events. The larger the value, the more central the event is.

With these likelihoods in place, a ratio is then constructed as follows:

$$W_{ness}(x_1 \cdots x_n) = \frac{\lambda_{sig}(x_1 \cdots x_n)}{\lambda_{sig}(x_1 \cdots x_n) + \lambda_{bkg}(x_1 \cdots x_n)} \tag{5.2}$$

This is again a distribution that ranges between 0 and 1. It can be interpreted as telling if an event is relatively more like the average signal event ($W_{ness} \to 1$) or more like the average background event ($W_{ness} \to 0$). Hence, as it describes if an event is like the W boson signal of interest, this ratio is so called "W_{ness}".

Not all of these variables, however, have information available for every event. In particular, the RPC 1, RPC3 and FVTX variables are limited to the partial θ coverage of each detector respectively. In order to avoid cutting any data while still taking advantage of additional variables, the W_{ness} calculation is split and done separately for event subsets matching each detector availability permutation. This results in $3 \times 2 = 6$ W_{ness} calculations for (RPC 1 only / RPC 3 only / Both) $\times$ (no FVTX / yes FVTX) conditions. The separate calculations are used to assign a W_{ness} value to each event depending on which condition it satisfies. A distribution of W_{ness} for all events can be seen for both signal and background in figure 5.2.

Note the increasing concentration of signal relative to background in the high W_{ness} region. In order to

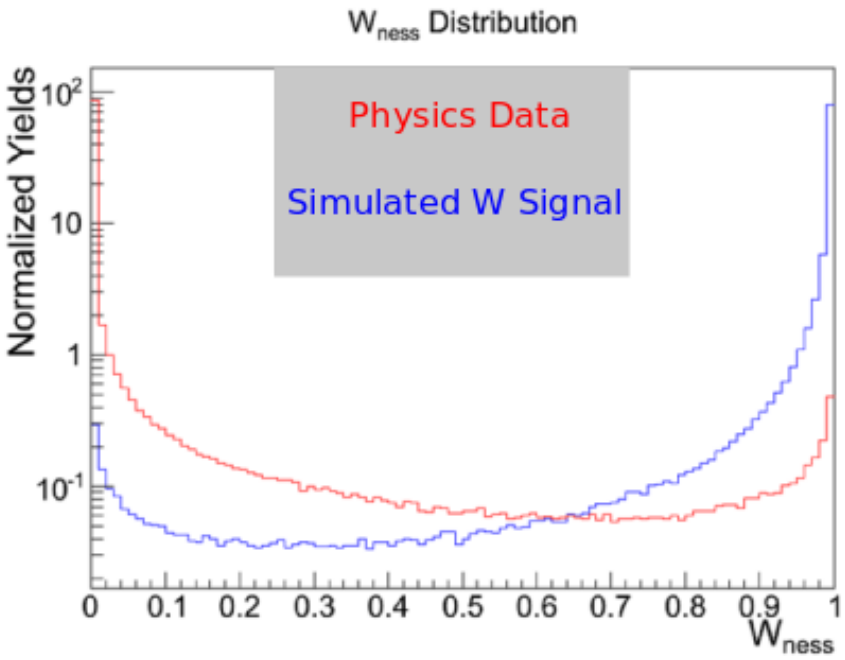

Figure 5.2: Taken from [32]. Distributions of W_{ness} are shown for the recorded data in red, and the simulated data in blue. Note that the vertical is plotted on a log scale. The two distributions have been normalized to total area.

filter out background then, a cut threshold is chosen in W_{ness} and the subset of data is selected of events with W_{ness} values greater than the threshold. There tradeoff when choosing a threshold value though: A higher threshold offers a higher signal concentration which leads to lower systematic uncertainty when determining the signal yield. But a higher threshold also selects a smaller subset of events meaning higher statistical uncertainty. Details explaining this threshold value selection are discussed in section 5.1.2.3.2. For now, it will be taken for granted that a cut of $W_{ness} > 0.92$ is applied to select a reduced dataset.

5.1.2 Signal to Background Ratio

The reduced dataset has a higher concentration of signal events, but still contains background events as well. A_L^W is by definition an asymmetry of signal events. And background events are expected to have no asymmetry. So an asymmetry calculated from events in the reduced dataset will be the true A_L^W of signal events diluted by background events with 0 asymmetry and must be adjusted according to the relative amount of signal and background present.

The approach taken to determine this ratio of signal to background events in the reduced dataset is summarized as follows: As in the event preselection, the distribution of events with respect to certain kinematic variables will be modeled for signal events and background events, but this time in more detail for

each subprocess that contributes to the dataset. Intrinsically, the dataset consists of some certain percentage of events coming from each subprocesses (which is what needs to be determined). It follows that the shape and magnitude of a kinematic variable's distribution for all events in the dataset is determined by the sum of that variables shape for each of the subprocess scaled in magnitude according to the respective percentage of the dataset. Now working backward from this conceptually, if the shape of a kinematic distribution can be accurately modeled for each subprocess, then a fit can be performed to determine what relative magnitude of each subprocess produces a summed distribution that best matches the actual distribution from the reduced dataset. This fit then provides the needed value of the relative yield of signal and background.

This procedure uses two kinematic variables that have particularly distinctly shaped distributions for signal and background events: η and $dw_{23}23$. As described in section 4.2.2, η is the rapidity of the candidate track. dw_{23} is constructed as follows.

$$dw_{23} = p_T \times sin(\theta) \times d\phi_{23} \tag{5.3}$$

The idea of this variable is to compare the measured azimuthal bending to the conceptual azimuthal bending due to the radial MuTR Magnet. $d\phi_{23}$ represents the measured bending, and the reconstructed momentum of the track can be used to calculate the expected bending due to the magnet field, which is proportional to $1/(p_T sin(\theta))$. If $d\phi_{23}$ and p_T are measured perfectly for a muon track, then the distribution of the product $p_T \times sin(\theta) \times d\phi_{23}$ would converge to a constant value. More realistically, the true muons do have a relatively narrow distribution of dw_{23} but the less consistent tracking of the scattered hadronic events lead to a distinctly wider distribution. This results in dw_{23} being one of our most sensitive variables for distinguishing real muons from the dominant hadronic background, thus making it valuable for this signal / background fit. Section 5.1.2.1 will describe what subprocesses are included in the dataset and how the shapes of η and dw_{23} are determined for each.

Once the distributions are obtained for each process, the fit performed to determine the relative proportion of each constituent is an unbinned Maximum Likelihood Fit (MLF) performed simultaneously in both η and dw_{23}. A description of this fit and its results are found in section 5.1.2.2.

It will be shown later (section 5.3) that this procedure to determine the signal to background ratio provides a significant contributions to the systematic uncertainty of the final result, and thus efforts were made accurately understand and to minimize sources of uncertainty in the procedure. Some of the tests and studies will be discussed in section 5.1.2.3.

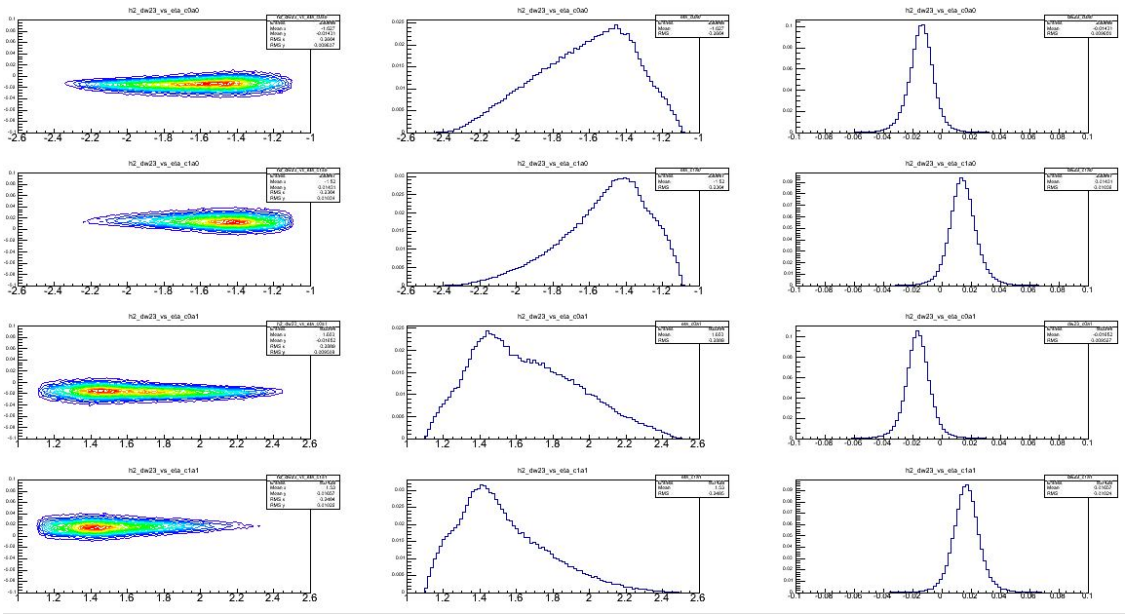

Figure 5.3: Distributions and pdf for $W/Z \rightarrow \mu$ events extracted from Pythia+Pisa simulation: η versus dw_{23} distributions (left), signal pdf as function of η (middle) and as function of dw_{23} (right), for positive and negative muons reconstructed in South arm, first and second row respectively, and in the North arm, third and fourth rows.

5.1.2.1 Composing PDF's

As described in the previous section, the EML fit to determine relative signal and background yields in the reduced dataset relies on accurately modeling the shape of η and dw_{23} distributions for events from each subprocess in the dataset. This section will detail how each subprocess is modeled and will show the final η and dw_{23} PDF's used as input to the EML fit in section 5.1.2.2.

For this signal to background ratio fit, the data is divided into the three categories of processes introduced in section 4.1.4: 1) Signal muons 2) Background muons 3) Hadronic background ("fake muons" events). Separately, each of these categories will be modeled in η and dw_{23} and ultimately the three processes will correspond to three relative magnitude parameters to be determined by the EML fit. Below is listed, one by one, how each process is modeled:

5.1.2.1.1 For Signal Muons: The $W \rightarrow \mu$ simulations described in section 4.4 and used in the event preselection are also used to model the signal muon η and dw_{23} distributions. PDF's of the distributions can be taken directly from normalized histograms of simulation events that pass a $W_{ness} > 0.92$ cut to match the reduced dataset. The resulting PDF's are shown in figure 5.3.

5.1.2.1.2 For Background Muons: The distributions for background muons will also be modeled with simulated data. However, as discussed in section 4.4 the are a multiple processes other than W decay that produce non-signal muons. Each process must be simulated separately and then combined with weights according to the respective cross section of each process. This process is described in section [44]. The weighted combination of events can then be used directly to model η and dw_{23}, again for only events in the $W_{ness} > 0.92$ region.

5.1.2.1.3 For Hadronic Background: In the event preselection step, the dataset was used directly as an approximate model of the total background. This approximation was valid because the full dataset consists of 95% background events (most of which are hadronic background events). After event preselction, such an approximation is no longer valid. In the reduced dataset, hadronic background events will be found to be a only a slight majority of the total event yield. As discussed in the simulation section (4.4), the hadron simulations are not as reliable as the muon simulations. So a proceedure was employed to derive the shape of the hadronic background PDF's from the full dataset.

Again, the goal is to model the distributions of η and dw_{23} for hadronic events in the reduced data set (events with $W_{ness} > 0.92$). The lower $W_{ness} < 0.92$ region is dominated by hadronic background, so the two distributions are considered as a function of W_{ness} in this region, and then extrapolated to the high $W_{ness} > 0.92$ region.

In the case of η, the shape of the distribution does not vary with W_{ness}. So the η distribution is used directly from the low W_{ness} region, specifically $0.1 < W_{ness} < 0.9$.

In the case of dw_{23}, the shape does vary with W_{ness}. So a fit is performed to parameterize this variance and the shape is extrapolated from $0.1 < W_{ness} < 0.9$ to $W_{ness} > 0.92$. This fit has two steps. Because W_{ness} is more consistent as a function of dw_{23}, and because the distribution of interest is dw_{23}, a one dimensional fit is performed to parameterize the W_{ness} distribution. Next, the obtained parameters for W_{ness} are fixed in a two dimensional dw_{23} vs W_{ness} fit. This fit will provide not only parameterization for dw_{23}, but the variance in these parameters as a function of W_{ness}.

The functional form used for the one dimensional W_{ness} fit is a 4^{th} degree polynomial (as seen in equation 5.4). A plot showing the data points and the W_{ness} fit results are shown in the bottom right panel of figure 5.4 for the example of negative muons in the South arm. As mentioned, the obtained parameters of this 4^{th} degree polynomial are then fixed the the two dimensional dw_{23} vs W_{ness} fit.

$$pol_4(W_{ness}; C_0, C_1, C_2, C_3, C_4) = C_0 + C_1 W_{ness} + C_2 W_{ness}^2 + C_3 W_{ness}^3 + C_4 W_{ness}^4 \tag{5.4}$$

The functional form used to model the dw_{23} distribution is a coaxial double Gaussian (sum of two Gaussian functions with different widths and the same mean). For a one dimensional dw_{23} distribution, the function (referred to as $f_{1D}(dw_{23})$ could be written:

$$f_{1D}(dw_{23};\mu,\sigma_1,\sigma_2,C_{rel},C_{scale}) = C_{scale} \times \left(e^{\frac{1}{2}\left(\frac{dw_{23}-\mu}{\sigma_1}\right)^2} + C_{rel} \times e^{\frac{1}{2}\left(\frac{dw_{23}-\mu}{\sigma_2}\right)^2} \right) \tag{5.5}$$

Where μ is the mean of both Gaussians, σ_1 and σ_2 are the respective widths of the Gaussians, C_{rel} is a constant that determines the relative weight of each Gaussian, and C_{scale} is a constant fixing the magnitude of the total distribution. C_{scale} for the distribution of dw_{23} for any small range in W_{ness} would then match the height of the W_{ness} distribution for that range (yield of events within the range). This height of the W_{ness} distribution is determined from pol_4, so for the two dimensional distribution vs dw_{23} and W_{ness}, f_{1D} is normalized and then multiplied by $pol_4(W_{ness})$. Additionally, to account for the variation in the shape of dw_{23} as a function of W_{ness}, constants from eq. 5.5 are assumed to be linear functions of W_{ness}. The constants from eq. 5.5 are then adapted to two dimensions as follows where all k constants will be determined by the two dimensional fit.

$$\begin{aligned}
\mu(W_{ness};k_{0\mu},k_{1\mu}) &= k_{0\mu} + k_{1\mu}W_{ness} \\
\sigma_1(W_{ness};k_{0\sigma_1},k_{1\sigma_1}) &= k_{0\sigma_1} + k_{1\sigma_1}W_{ness} \\
\sigma_2(W_{ness};k_{0\sigma_2},k_{1\sigma_2}) &= k_{0\sigma_2} + k_{1\sigma_2}W_{ness} \\
C_{rel}(W_{ness};k_{0C_{rel}},k_{1C_{rel}}) &= k_{0C_{rel}} + k_{1C_{rel}}W_{ness} \\
C_{scale}(W_{ness};...) &= pol_4(W_{ness}) \times \left(\frac{1}{\sqrt{2\pi}\sigma_1(W_{ness}) + C_{rel}(W_{ness})\sqrt{2\pi}\sigma_2(W_{ness})} \right)
\end{aligned} \tag{5.6}$$

In the $C_{scale}(W_{ness})$ equation, k constants are not written for brevity but still exist. Also, $pol_4(W_{ness})$ does depend on the C_n constants but they are fixed by the previous 1D W_{ness} fit. So the final function that is fit to the two dimensional dw_{23} vs W_{ness} distribution is written in equation 5.7 in terms of the equations in 5.4 and 5.6 (with, again, k and C_n constants omitted for brevity).

$$\begin{aligned}
&f_{2D}(dw_{23},W_{ness}) = \\
&\quad C_{scale}(W_{ness}) \times \left(e^{\frac{1}{2}\left(\frac{dw_{23}(W_{ness})-\mu(W_{ness})}{\sigma_1(W_{ness})}\right)^2} + C_{rel}(W_{ness}) \times e^{\frac{1}{2}\left(\frac{dw_{23}(W_{ness})-\mu(W_{ness})}{\sigma_2(W_{ness})}\right)^2} \right)
\end{aligned} \tag{5.7}$$

The results of this 2D fit is shown in figure 5.4. The left column shows 1D projections of $dw_2 3$ for the data along with the fit result for increasing subranges in $W_n ess$. The central column shows the linear W_{ness} variance of the double Gaussian parameters (μ, σ_1, σ_2 and C_{rel} respectively). The right column features, in the bottom two panels, the fit results plotted with the data points in 2D and the 1D projection of W_{ness} along with the pol_4 fit.

Once the k parameters are determined by the fit, they can be used to extrapolate the $dw_2 3$ shape to the target $W_{ness} > .92$ region by evaluating the W_{ness} dependent double Gaussian parameters at the mean W_{ness} of the data in the target region. The result of this extrapolation is in figure 5.5 where extrapolated dw_{23} PDF's are shown for each arm and charge. Additionally, a cross check was performed between 4 analyzers who all followed this procedure with independently written code. The results from each analyzer is shown in different colors and they are generally in very close agreement.

5.1.2.1.4 Final PDF's The final PDF's to be used in the signal to background ratio fit are shown in figure 5.6. The top row shows dw_{23} and the bottom row shows η for hadronic background(left column), background muons(middle column), and signal muons(right column). Again, each distribution was obtained as described above: signal and background muons from simulation and hadronic background from data extrapolation. The fit that uses the distributions to determine the relative contributions of each component is described in the following section.

5.1.2.2 Extended Maximum Likelihood Fit

Once these distributions are obtained for each component of the data, an Extended Maximum Likelihood (EML) Fit is used to determine the ratio of each component present in the dataset. EML fits are a well established fitting technique that applies probabilistic principles to establish a "likelihood" for possible ratios of components. This likelihood is then maximized to estimate the ratios that best match the data. An early proposal of this technique can be found in reference [45].

Our fit is two dimensional for dw_{23} and η. One dimensional distributions for each of these variables for each component are converted (normalized) to PDF's which are the direct input to the fit. These input distributions can be found in the previous section.

Because the background muons can be very similar to signal muons in these distributions, the choice is made to fix the ratio of background muons to a constant value in the fit. This difficulty and uncertainty in the fit between the two. The scale value is chosen by scaling the effective luminosity generated in the simulation to match the luminosity of the data.

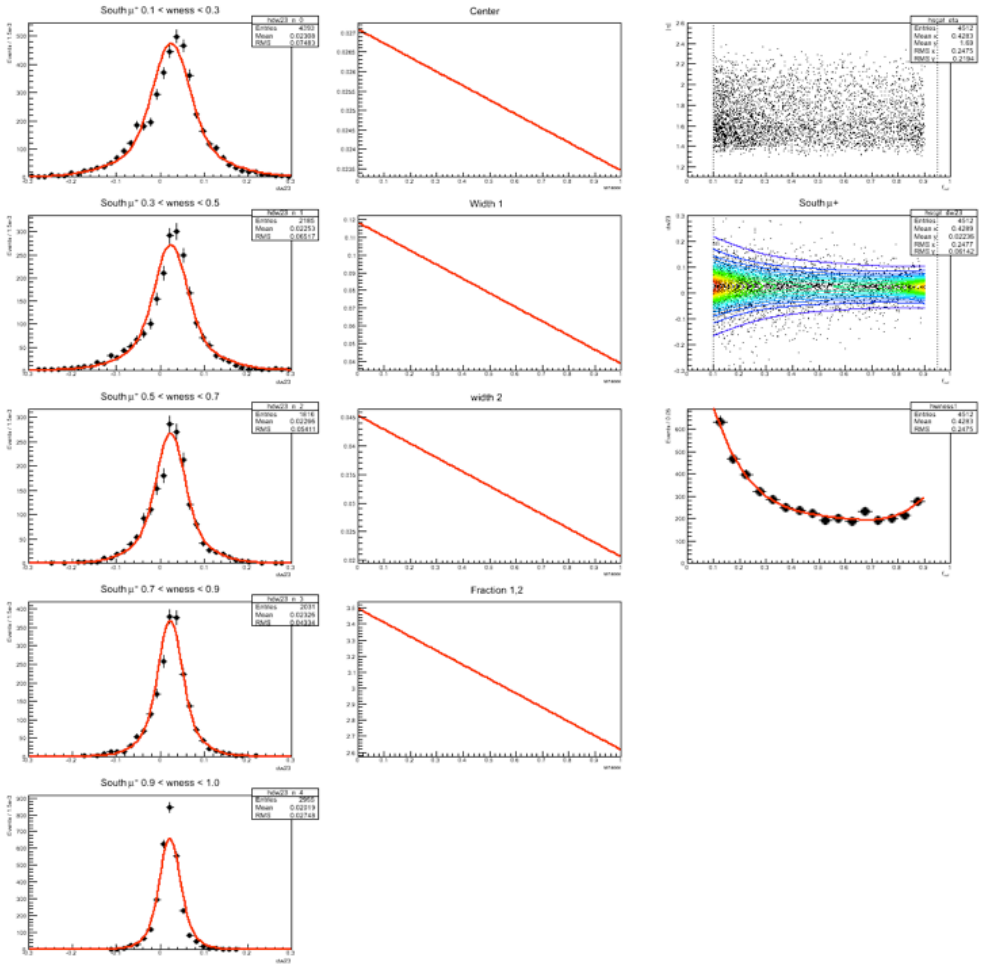

Figure 5.4: Distribution for the hadronic background for negative muon candidates in the South arm. Each set of panels show the W_{ness} distribution (right column, bottom plot), the 2D dw_{23} versus W_{ness} fit (right column, middle plot) and the 2D histogram eta versus dw_{23} (right column, top plot). In each set of panels the first columns show the projection into one dimension of the 2D dw_{23} versus W_{ness} fit in different cut in W_{ness}, compared with the corresponding 1D dw_{23} histogram, while the middle columns show the parameters used in the 2D dw_{23} function versus W_{ness}

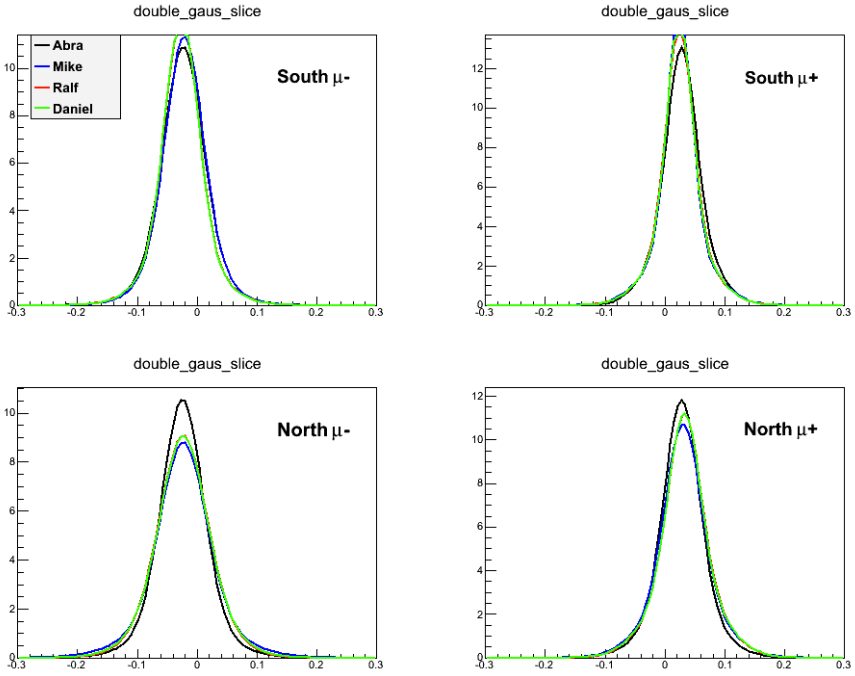

Figure 5.5: Hadronic background dw_{23} PDF's. Generated using 2D dw_{23} vs W_{ness} fit results extrapolated to the $W_{ness} > 0.92$ region for each arm and charge. Results from each analyzer shown in different colors as labeled.

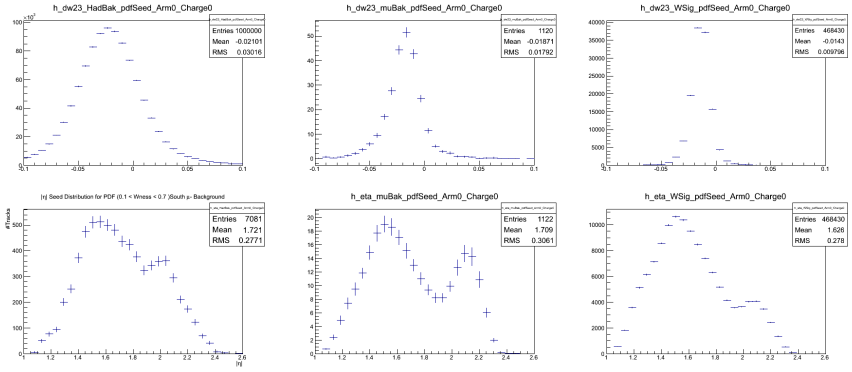

Figure 5.6: Input PDF's for EML fit. dw_{23}(top row) and η(bottom row) distributions for the $W_{ness} > 0.92$ range for hadronic background(left column), background muons(middle column) and signal muons(right column).

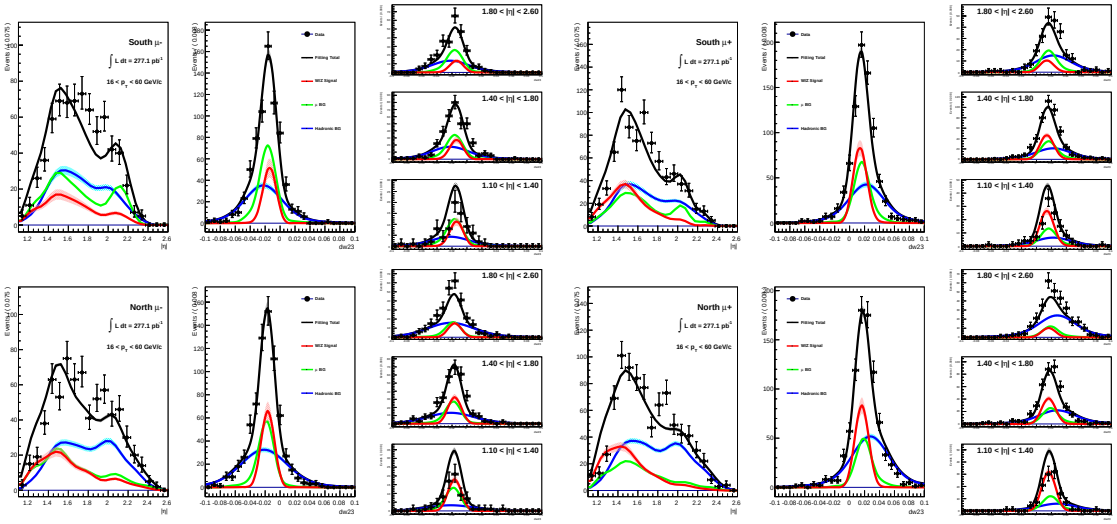

Figure 5.7: Fit results for the signal to background ratio for South muon minus (top left), South muon plus (top right), North muon minus (bottom left), North muon plus (bottom right). Each set of of plots shows the fit results for the η distributions (left) and for the dw_{23} in one η bin (middle) and the 3 η bins mentioned in the text (right columns).

Final fit values for component yields and uncertainties resulting from the EML fit are shown alongside the final A_L^W results in the results chapter: tables 6.1 and 6.2. The fit results are also plotted here in 5.7 where each component's distribution is scaled and plotted along with the resulting sum of components compared with the data points. One important note is that the reduced χ^2 of the fit is somewhat large. Extensive studies have been made to understand and improve this fit accuracy. These efforts will be discussed in the next section (5.1.2.3). But as it stands, this fit uncertainty is accounted for in the final systematic uncertainty and is, in fact, one of the largest contributions. More is discussed about the final uncertainty in section 5.3.

5.1.2.3 Further Tests and Studies

The value of the extracted signal yield from the EML fit is used to directly scale the final A_L^W value and is thus very important. Many studies have been done attempting to understand and characterize the behavior and uncertainty of this. This section will discus some of this work.

5.1.2.3.1 Simulation Consistency Test ("PEPSI Challenge") This is the most significant test used to understand and estimate uncertainty of the EML fit. In the EML fit, simulation is used to model the signal and background muons, and data is extrapolated to model the background hadronic events. The simulation consistency test (called the "PEPSI challenge" internally in reference to the PEPSI $e-p$

simulation software familiar to collaborators from previous experiments) consists of using simulation to model all three components, and instead of fitting these modeled distributions to the dataset, a simulated dataset is constructed with a weighted combination of of the component simulations. This allows the analyzer to check the results of the fit against known results of the simulated dataset and evaluate the fit accuracy directly. In both the the real EML fit and this PEPSI challenge, the background muon yield is a fixed parameter determined by scaling the simulation event yield to match the luminosity of the dataset. The simulated dataset is similarly built: the signal muons and hadronic event simulations can also be scaled to show expected yields and the three are combined, against which the yields determined by the EML fit can be evaluated.

Figure 5.8 shows the extrapolation procedure to determine the hadronic background PDF applied to the PEPSI challenge dataset. For each arm/charge combination, dw_{23} distributions in progressive slices in W_{ness} are shown. The black data points are the combined simulation dataset and the blue histogram is the scaled background hadronic event simulation. The interesting indicator then is the red curve, which represents the results of the two dimensional dw_{23} vs W_{ness} extrapolation. The fit range is $0.1 < W_{ness} < 0.9$ and the extrapolated target region is $W_{ness} > 0.9$, shown in the lower panel. The match between the red curve and the blue histogram in the lower panel can be evaluated to judge the accuracy of the extrapolated hadronic background dw_{23} PDF. The green and purple curves are one dimensional fits to the hadron component and total simulation data, respectively, in each slice and are just shown for reference of how the extrapolation fit (red curve) compares to each.

The results of the final EML fit to determine the relative contributions for the PEPSI challenge is shown in figure 5.9. Each dimension of the two dimensional fit is shown for each arm/charge. Curves representing the PDF's of each component scaled according to the fit results and the sum of the three are shown (and labeled) in the plots. And histograms representing the simulation yields in the target region are shown for the signal muon (orange angle-hashed) and hadronic background (blue-grey horizontal-hashed) components. The histograms can be compared with the respective fit result curves.

As can be seen qualitatively, the determined signal yield (integral of the purple curve) matches the yield from the signal simulation (integral of the orange curve) fairly well in the μ^+ case (right panels), but that the signal is overestimated by the fit in the μ^- case (left panels). As a further, more basic consistency check, this same PEPSI procedure is followed using not the extrapolated hadronic dw_{23} PDF but rather the PDF from the hadronic simulation directly. In this case, it's truly a matter of adding η and dw_{23} PDF's from the three components according to the proper luminosity scaling then performing the EML fit with the same PDF's as input to re-extract the same relative scaling factors. As expected, this test is accurate in reproducing the

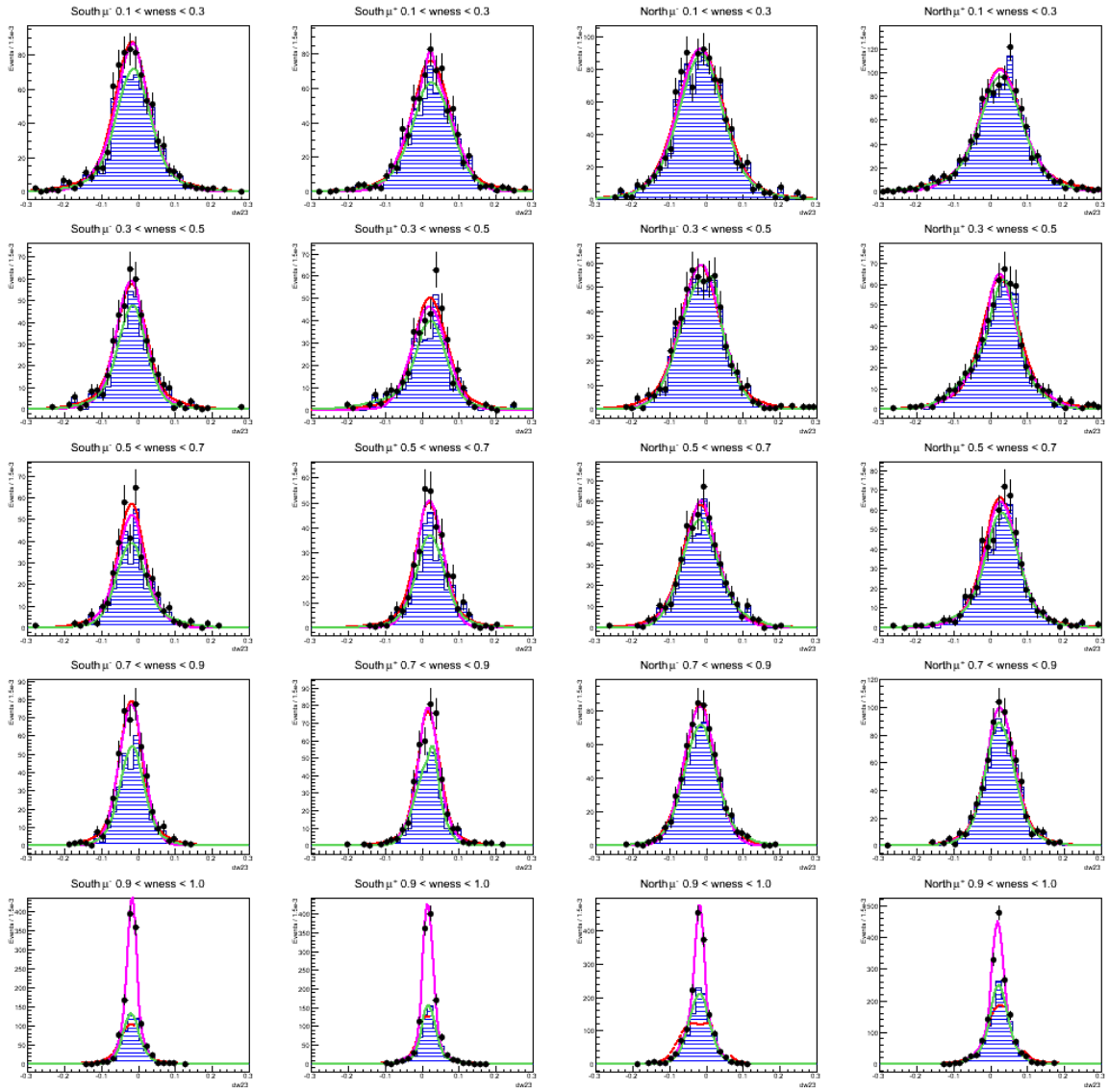

Figure 5.8: Taken from [44]. Hadronic (blue, filled histograms) and MC data (black points) dw_{23} distributions for South μ^-, South μ^+, North μ^- and North μ^+ from left to right. From top to bottom the individual wness slices are shown, of which the first 4 (0.1 - 0.9) are used to fit the dw23 and wness dependence and extrapolate into the signal region (bottom row). The projection of these fits into all slices is shown in red, individual fits in the slices are displayed in purple and individual fits to only the hadronic contributions are displayed in green.

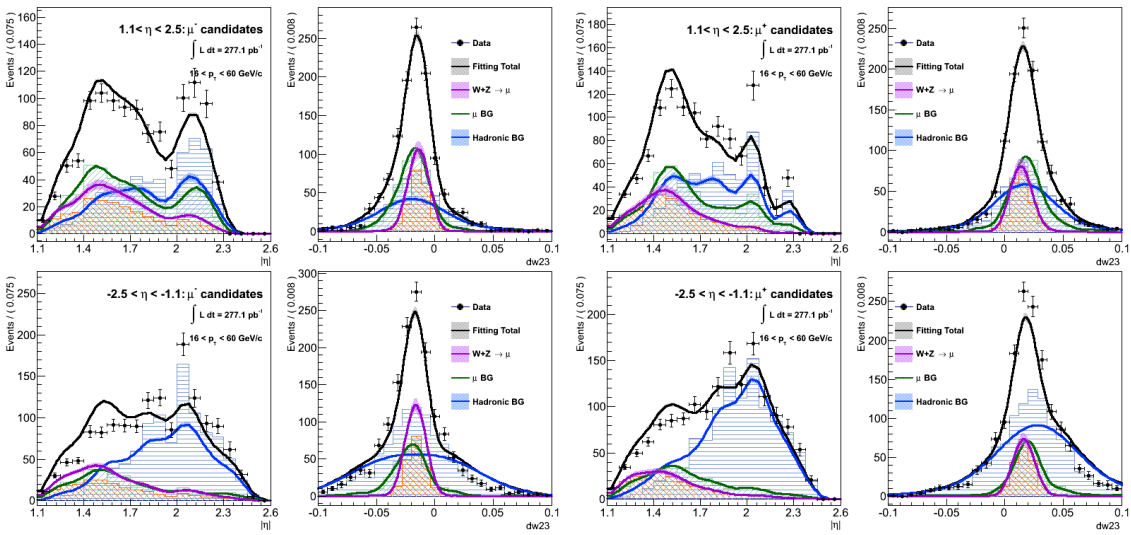

Figure 5.9: Taken from [44]. Fit results for the PEPSI challenge with a minimal wness selection of 0.85 for South μ^- (top left), South μ^+ (top right), North μ^- (bottom left), North μ^+ (bottom right). Each set of of plots shows the fit results for the η distributions (left) and for the dw_{23} in one η bin (middle) and the 3 η bins mentioned in the text (right columns). The full lines are the results of the fit while the shaded, filled histograms display the contributions actually contained in this MC set.

true ratio of the components. The amount of overestimation found in the first method (which matches the procedure used on the real data) relative to this second method is then taken as an estimate of the (lower bound of) the systematic uncertainty associated with this hadronic extrapolation and EML fit procedure.

5.1.2.3.2 Varying the W_{ness} Threshold Another aspect of the signal and background characterization that was studied is the effect of varying the W_{ness} value used to select the reduced dataset. Varying this threshold has strong implications of the uncertainty of the final result. The higher the threshold, the higher the concentration of signal in the reduced dataset. And the EML fit uncertainty reduces with higher signal concentration. But a higher threshold also results in a lower total yield of events and thus higher statistical uncertainty.

The PEPSI challenge is used as to test the effects of varying this threshold. With simulated data for all components, the entire PDF composition and EML fit procedure is done using different reduced datasets from a range of W_{ness} threshold values. The resulting range of ratio of signal and background yield determined by the fits are shown in figure 5.10. The green line and band are the ratio values and uncertainty bands. The pink line is shown for reference: it is the known, true signal to background ratio from the simulated components. Note the X axis is 1-W_{ness}Thr and a logarithmic scale. So left on the axis is higher threshold values.

These values of signal to background ratio and associated uncertainties (both systematic from the fitting

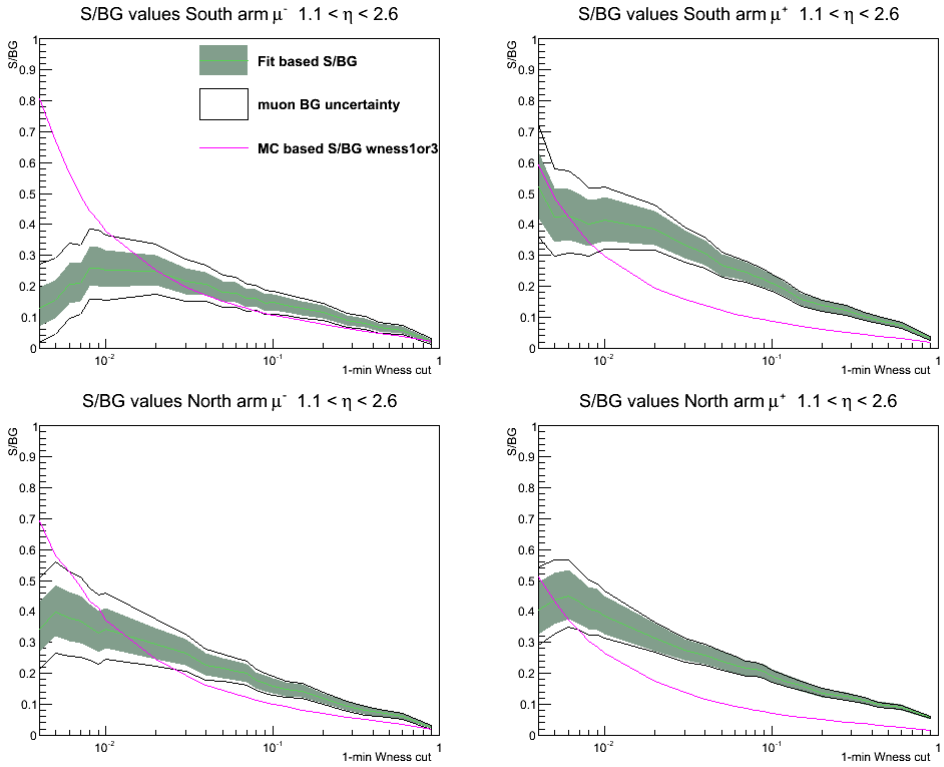

Figure 5.10: Taken from [44]. Signal to background ratios for varying W_{ness} thresholds using simulated data for all components. The X axis is (1 - W_{ness}Threshold) so left on the axis corresponds to a higher W_{ness} threshold (eg. 0.01 on the axis corresponds to a W_{ness} threshold of 0.99). Shown are ratios from the PDF EML fit procedure(green lines and uncertainty) and ratios calculated directly from the simulated components. Shown for each arm and charge.

procedure and statistical from the yield of the reduced dataset) can be propagated through the rest of the A_L^W calculation to determine the effect on the final figure of merit (sum of statistical and systematic uncertainty). The optimal W_{ness} threshold is the one that minimizes the figure of merit(FOM). Figure 5.11 shows the resulting FOM for the varying W_{ness} thresholds (again with results from using the simulations directly to calculated SBR in pink for reference). The fitting procedure (green) is fairly flat over a range of W_{ness} cuts with a minimum that is consistent with the currently used cut of 0.92, but also would be consistent larger thresholds. The purely simulation driven results on the other hand have minimums at much higher threshold, or even continue trending downward with higher threshold without a minimum. While, again, this study is done with only simulations, not the real dataset, these trends are used to inform the selection of W_{ness} cut. So in addition to the W_{ness} threshold of 0.92, the analysis is also performed with a threshold of 0.99 and in fact, the final A_L^W results reported in chapter 6 are from the $W_{ness} > 0.99$ reduced dataset. Table 5.2 lists the signal to background ratios for various η ranges compared between the 0.92 and 0.99 thresholds.

W_{ness} Cut	η Range	South μ^-	South μ^+	North μ^-	North μ^-
0.92	1.1 -2.6	0.21	0.30	0.26	0.30
0.99		0.30	0.50	0.45	0.50
0.92	1.1 -1.4	0.34	0.60	0.57	0.86
0.99		0.44	0.91	0.75	1.18
0.92	1.4 -1.8	0.23	0.34	0.30	0.33
0.99		0.33	0.55	0.50	0.54
0.92	1.8 -2.6	0.15	0.11	0.13	0.08
0.99		0.21	0.19	0.27	0.16

Table 5.2: Signal to background ratios for varying η ranges for each arm and charge compared for 0.99 and 0.92 W_{ness} thresholds.

5.2 Single Spin Asymmetry Calculation

Now for the calculation of the final value of interest: single spin asymmetry in W production (A_L^W). This asymmetry is a "single" asymmetry because it considers the helicity of one beam but averages over possible helicities of the other beam. A_L^W is written as:

$$A_L^W = \frac{\sigma^+ - \sigma^-}{\sigma^+ + \sigma^-} \propto \frac{n^+ - n^-}{n^+ + n^-}$$

Where $n^{+(-)}$ is the observed yield from events with positive (negative) helicity of the polarized beam. The later equation is defined as the raw asymmetry ϵ_L and will be discussed in section 5.2.1. But it neglects

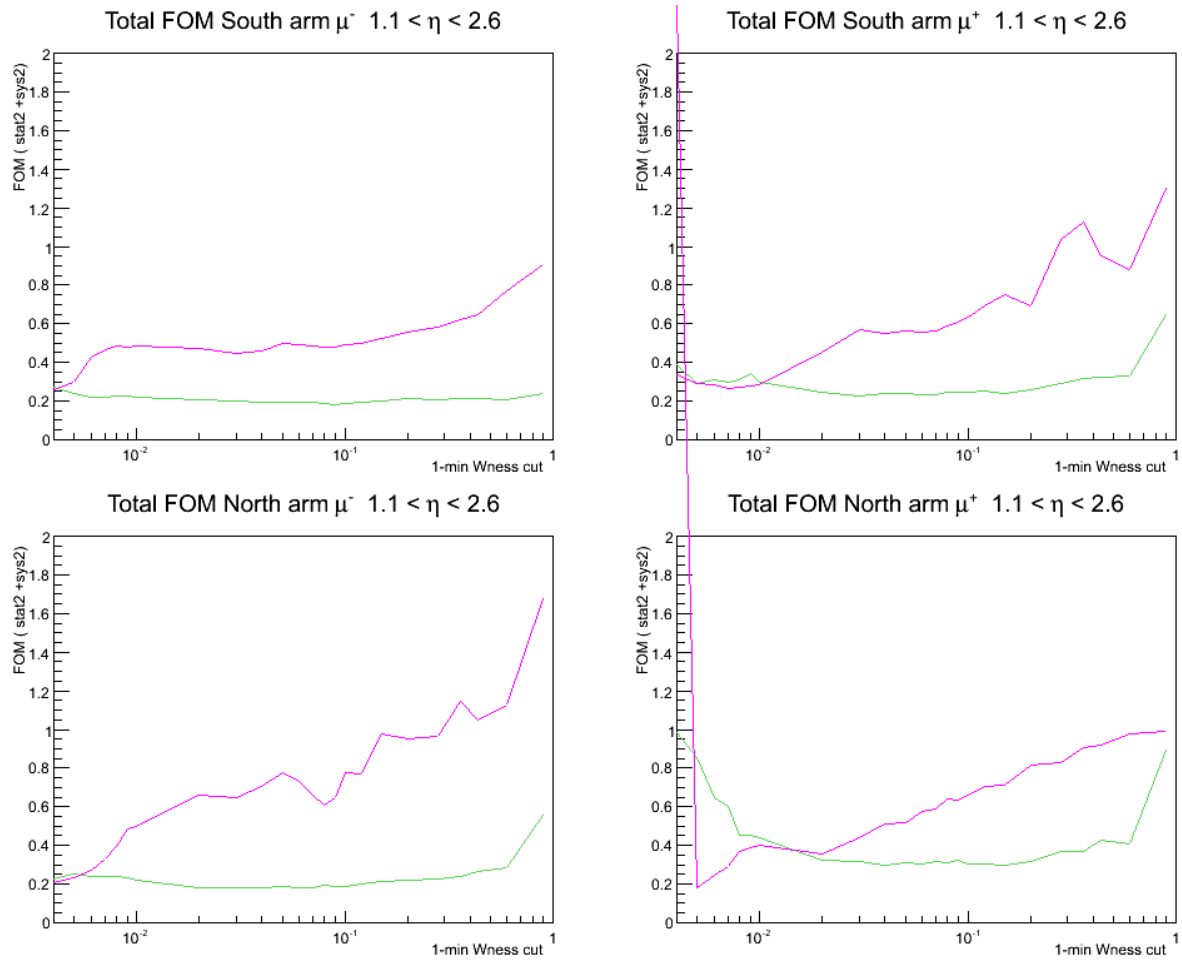

Figure 5.11: Taken from [44]. Figure of merit distributions as functions of the minimum wness selection for each arm and charge. The figure of merits are shown as derived using the fit based signal to background values (green curves) and those calculated from the simulation directly (purple lines).

certain correction factors. Because the asymmetry is calculated with the reduced dataset, which is not pure signal events but also contains backgrounds with no inherent asymmetry, a "dilution factor" must be applied to the raw asymmetry. Also, the beam is not fully polarized so a scale factor for the polarization level is also applied. This scaling is discussed in section 5.2.2.

5.2.1 Raw Asymmetry

A simple raw single spin asymmetry is generally written as:

$$\epsilon_L = \frac{n^+ - n^-}{n^+ + n^-}$$

At PHENIX, Signal is observed separately in the North and South arms so yields can be counted and

asymmetries calculated separately. Additionally, there are four possible helicity combinations of the two polarized beams, and for a single spin asymmetry one must average over helicity of one of the beams. Between these permutations, the following yields can be counted:

$$n_N^{++}, n_N^{+-}, n_N^{-+}, n_N^{--}, n_S^{++}, n_S^{+-}, n_S^{-+}, n_S^{--}$$

Where the +'s and −'s represent the helicity of the blue and yellow beams ($n_{<arm>}^{<blue><yellow>}$). Observed yields of events passing a $W_{ness} > 0.92$ cut are shown in 5.12. Note that yields are listed separately for positive and negative charges. The asymmetries will also be segmented according to charge and calculated separately, but the remainder of this section will discuss the asymmetry calculation without specifying charge.

To consider the polarization of the blue beam and average over the yellow beam in the North, for example, one would take $n_N^{+} = n_N^{++} + n_N^{+-}$ and $n_N^{-} = n_N^{-+} + n_N^{--}$. Raw single spin asymmetries then can be written in terms of these yields. At this point it's useful to convert from an arm notation to a rapidity-relative-to-beam notation because the result of interest is asymmetry as a function of rapidity relative to the polarized beam. So in the following raw asymmetries, the superscript is of the format $B(Y)\eta+\{-\}$ indicating the polarization of the Blue(Yellow) beam is considered and events are observed at positive {negative} rapidity relative to that beam.

$$\epsilon_L^{B\eta+} = \frac{(n_N^{++} + n_N^{+-}) - (n_N^{-+} + n_N^{--})}{(n_N^{++} + n_N^{+-}) + (n_N^{-+} + n_N^{--})}$$

$$\epsilon_L^{B\eta-} = \frac{(n_S^{++} + n_S^{+-}) - (n_S^{-+} + n_S^{--})}{(n_S^{++} + n_S^{+-}) + (n_S^{-+} + n_S^{--})}$$

$$\epsilon_L^{Y\eta+} = \frac{(n_S^{++} + n_S^{-+}) - (n_S^{+-} + n_S^{--})}{(n_S^{++} + n_S^{-+}) - (n_S^{+-} + n_S^{--})}$$

$$\epsilon_L^{Y\eta-} = \frac{(n_N^{++} + n_N^{-+}) - (n_N^{+-} + n_N^{--})}{(n_N^{++} + n_N^{-+}) - (n_N^{+-} + n_N^{--})}$$

And, as mentioned, each of these raw asymmetries can be calculated separately for positive and negative muons. The results are shown in figure 5.13. These raw asymmetries then need to be scaled (as discussed in the next section) and combined for the blue and yellow beams to give the final asymmetry values.

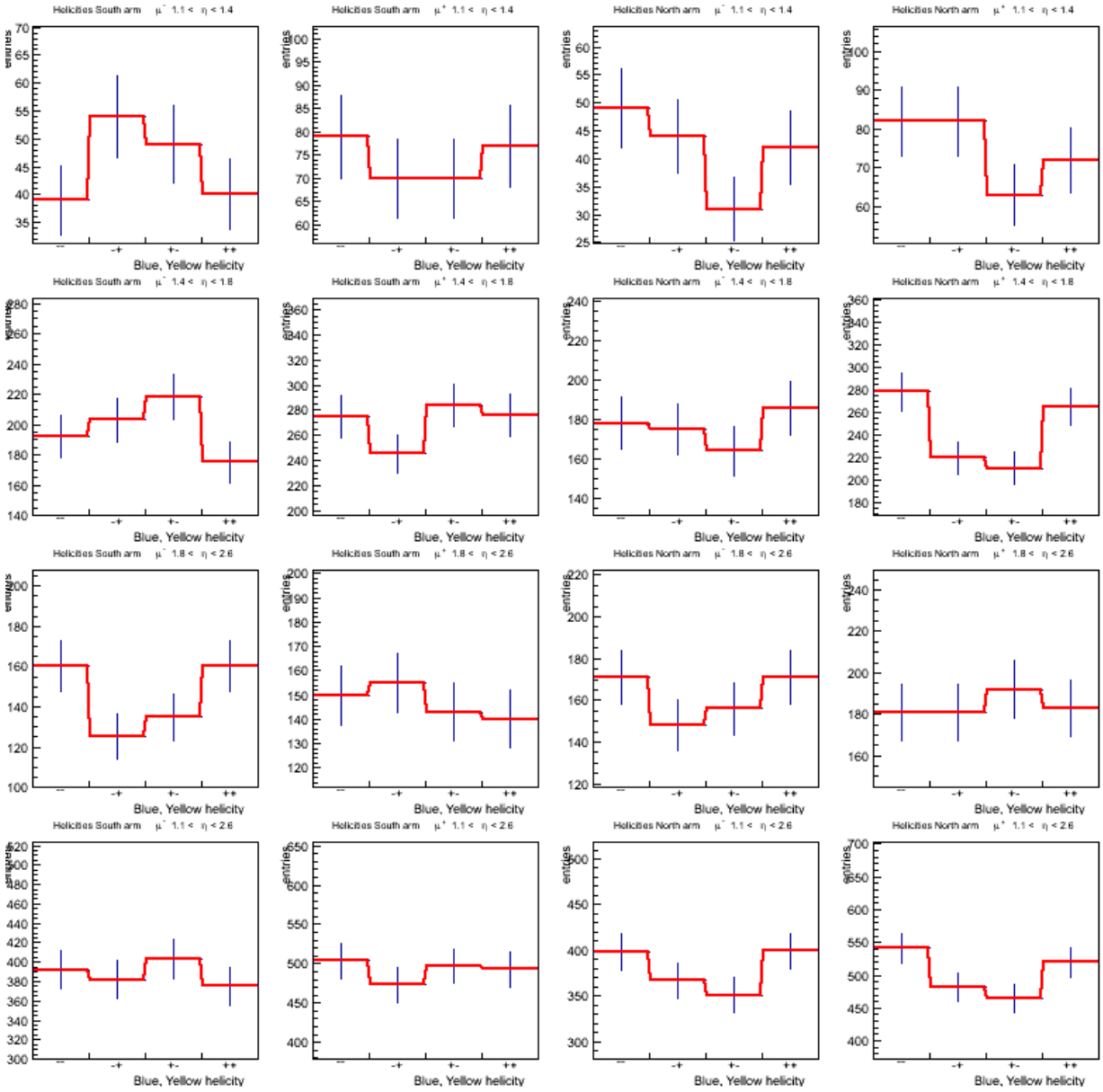

Figure 5.12: Taken from [44]. Each plot shows helicity dependent yields of the $W_{ness} > 0.92$ reduced dataset for varying η ranges and arm/charge combinations. The top row is for $1.1 < \eta < 1.4$, the second row is $1.4 < \eta < 1.8$, the third $1.8 < \eta < 2.6$, and the last row is for the full $1.1 < \eta < 2.6$ range. The columns show South μ^-, South μ^+, North μ^- and North μ^+ yields respectively.

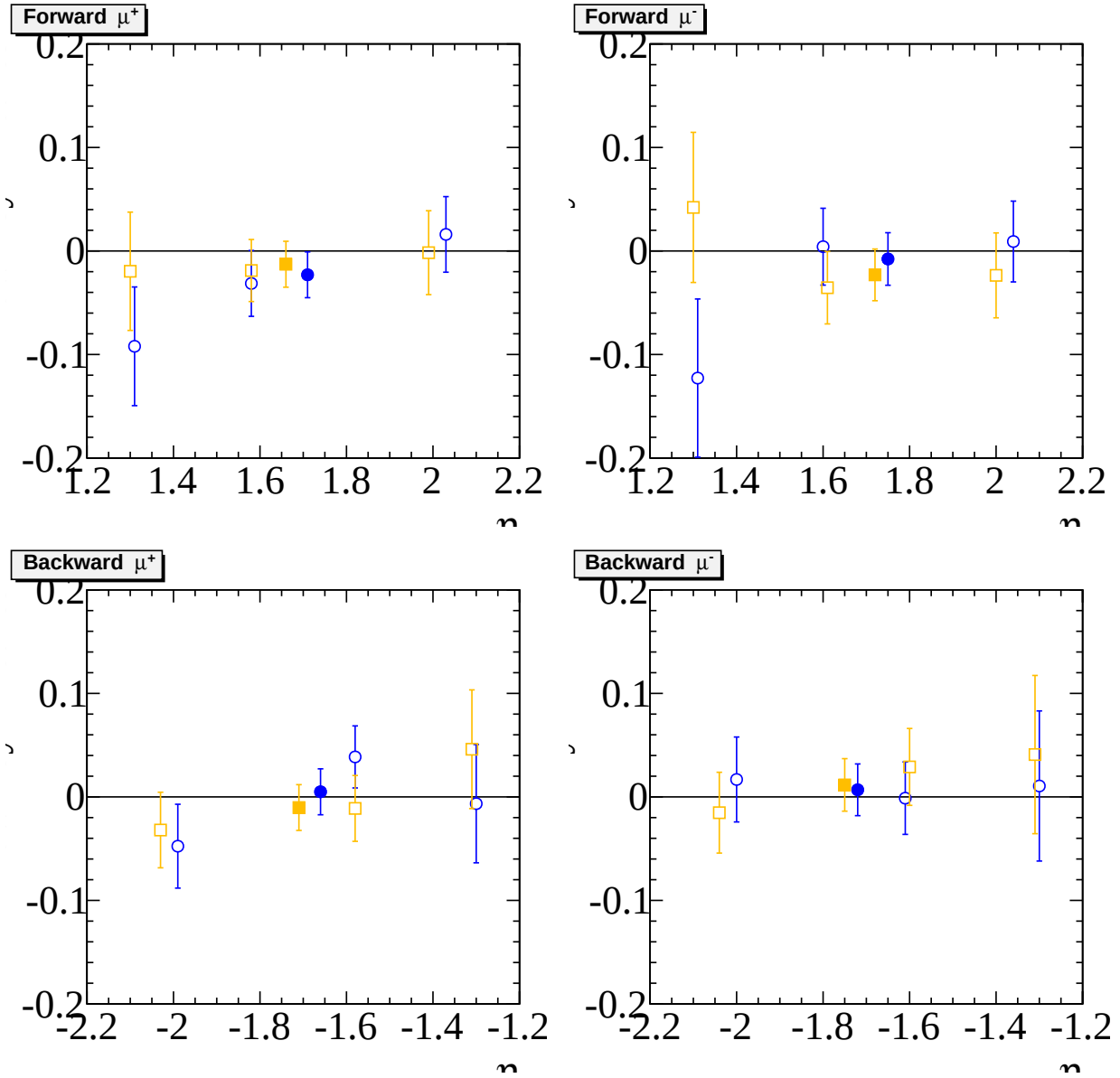

Figure 5.13: Taken from [44]. Raw asymmetries, ϵ_L, for the Blue (blue symbols) and Yellow (orange symbols) beams in the forward (top) and backwards (bottom) direction relative to the polarized beam for $W_{ness} > 0.92$. The different points show the different rapidity bins (open symbols) and their average (full symbols).

5.2.2 Scaling Factors

The calculation for the raw asymmetry would be a valid A_L^W if the beam was fully polarized and if the events used to calculate the raw asymmetry were purely signal events. Neither of these conditions is true and factors must be applied to account for each. The final asymmetry is written in terms of the raw asymmetry as:

$$A_L^W = \frac{1}{P} \cdot D \cdot \epsilon_L$$

Where P is the polarization level of the polarized beam and D is the "dilution factor" of the events in the raw asymmetry as defined below. Note that this dilution factor exists because the background has no inherent asymmetry in production.

$$D = 1 + \frac{n_{background}}{n_{signal}}$$

As discussed in section 4.1.2, the polarization values averaged over runs are 50.5±0.2% for the blue beam and 55.4±0.2% for the yellow beam. The dilution factors come from the signal to background ratios as calculated in section 5.1.2. The raw asymmetry values and the corresponding corrections according to these factors are found in the results chapter in section 6.1.

5.3 Systematic Uncertainty

The systematic uncertainty on the final A_L^W values comes primarily from charge reconstruction uncertainties and from systematics associated with the signal to background ratio estimation. The SBR related sources of uncertainty are described in the following list and table 5.3 shows the corresponding values.

- **Momentum Smearing in the MuTr**
  - As previously described, the limited momentum resolution of the MuTr resulting in smeared reconstructed momentum is modeled in the simulations used in the EML fit. And as discussed in section 4.5.1, the simulations were compared with cosmic data to ensure the proper level of smearing. To account for possible uncertainty in this proceedure, the constant defining smearing is varied by a factor of two. The resulting simulated events with varied smearing are then processed through the EML fit. The variation the signal yield from the fit is then taken as a systematic uncertainty.
- **Fixed Muon Background Yield**

	etabin	stat	smear	μBG	Trigeffi	combined
N^+	0	$1.18^{0.20}_{0.18}$	$^{0.04}_{0.00}$	$^{0.17}_{0.16}$	$^{0.00}_{0.37}$	$1.18^{0.26}_{0.44}$
N^-	0	$0.75^{0.15}_{0.14}$	$^{0.19}_{0.00}$	$^{0.17}_{0.16}$	$^{0.00}_{0.33}$	$0.75^{0.30}_{0.39}$
S^+	0	$0.91^{0.16}_{0.15}$	$^{0.05}_{0.00}$	$^{0.17}_{0.15}$	$^{0.04}_{0.09}$	$0.91^{0.24}_{0.23}$
S^-	0	$0.44^{0.11}_{0.10}$	$^{0.04}_{0.00}$	$^{0.14}_{0.12}$	$^{0.01}_{0.28}$	$0.44^{0.18}_{0.32}$
N^+	1	$0.54^{0.09}_{0.08}$	$^{0.02}_{0.00}$	$^{0.08}_{0.07}$	$^{0.00}_{0.14}$	$0.54^{0.12}_{0.18}$
N^-	1	$0.50^{0.10}_{0.09}$	$^{0.12}_{0.00}$	$^{0.12}_{0.10}$	$^{0.00}_{0.19}$	$0.50^{0.20}_{0.23}$
S^+	1	$0.55^{0.10}_{0.09}$	$^{0.03}_{0.00}$	$^{0.10}_{0.09}$	$^{0.08}_{0.06}$	$0.55^{0.16}_{0.14}$
S^-	1	$0.33^{0.08}_{0.07}$	$^{0.03}_{0.00}$	$^{0.10}_{0.09}$	$^{0.01}_{0.20}$	$0.33^{0.14}_{0.23}$
N^+	2	$0.16^{0.03}_{0.02}$	$^{0.01}_{0.00}$	$^{0.02}_{0.02}$	$^{0.04}_{0.00}$	$0.16^{0.05}_{0.03}$
N^-	2	$0.27^{0.05}_{0.05}$	$^{0.07}_{0.00}$	$^{0.06}_{0.06}$	$^{0.03}_{0.05}$	$0.27^{0.11}_{0.09}$
S^+	2	$0.19^{0.03}_{0.03}$	$^{0.01}_{0.00}$	$^{0.03}_{0.03}$	$^{0.08}_{0.00}$	$0.19^{0.09}_{0.04}$
S^-	2	$0.21^{0.05}_{0.05}$	$^{0.02}_{0.00}$	$^{0.07}_{0.06}$	$^{0.05}_{0.11}$	$0.21^{0.10}_{0.13}$
N^+	3	$0.50^{0.08}_{0.08}$	$^{0.02}_{0.00}$	$^{0.07}_{0.07}$	$^{0.00}_{0.12}$	$0.50^{0.11}_{0.16}$
N^-	3	$0.45^{0.09}_{0.08}$	$^{0.11}_{0.00}$	$^{0.10}_{0.09}$	$^{0.00}_{0.16}$	$0.45^{0.18}_{0.20}$
S^+	3	$0.50^{0.09}_{0.08}$	$^{0.03}_{0.00}$	$^{0.09}_{0.08}$	$^{0.03}_{0.08}$	$0.50^{0.13}_{0.14}$
S^-	3	$0.30^{0.07}_{0.07}$	$^{0.03}_{0.00}$	$^{0.09}_{0.08}$	$^{0.02}_{0.18}$	$0.30^{0.12}_{0.21}$

Table 5.3: Various contributions to the signal to background uncertainty as it will enter the final asymmetries based on $W_{ness} > 0.99$.

  - The yield of muons simulated from background sub-processes is fixed in the EML fit. In principle, the accuracy of this is limited by how well our simulations accurately model the processes. Tests were done by considering dimuon processes. Dimuon events are more easily identified in the data and have a clear signal that can be compared with the yield of the simulated subprocesses. The simulations are tuned and fit to the data to match these signals and in this way the simulation is validated. The errors of the fit to data for each of the processes then are added in quadrature an taken as systematic uncertainty.

- **Trigger Efficiencies**
  - Trigger efficiences are discussed more thoroughly in section 4.3. They enter the analysis through scaling the signal and background muon simulations. Recall that two methods are used to calculate the total trigger efficiencies, the two methods are separately applied to both simulations and the EML fit is performed. Variations between the resulting yields are taken as the systematic uncertainty.

The other dominant systematic uncertainty contribution comes from the charge reconstruction efficiency. As discussed in the cosmic data section (4.5.2), while simulations suggest a charge reconstruction misidentification of only a few percent, the cosmic data shows efficiencies as low as 80%.

The uncertainties from each of the sources are combined to estimate the total systematic uncertainty of the final asymmetries using a Gaussian sampling technique. The value of each underlying source is varied randomly according to a Gaussian with a width matching that sources uncertainty. Then the varied values are propagated through the A_L^W calculation to produce a varied A_L^W value. This procedure is repeated many times to produce a distribution of A_L^W values. The width of this distribution is then taken as the A_L^W uncertainty. This same procedure is used with the systematic uncertainty contributions mentioned above as well as for the statistical uncertainty. Figure 5.14 shows the A_L^W distributions resulting from this sampling for both systematic(solid lines) and statistical(dashed lines) uncertainties. The final uncertainty values then are quoted with the results in section 6.1.

5.4 W Cross Section

An important check and validation of the procedures used to calculate A_L^W is a measurement of the $W^{\pm}$ cross sections. Measuring a cross section is a matter of counting a yield of events and dividing by the luminosity of the dataset and the efficiency of the process used to count the signal yields (which includes various experimental efficiencies as well as cut efficiencies associated with the analysis).

In this case, the signal yields will be taken from the EML fit on the reduced dataset as described in section 5.1.2. The luminosity is calculated as described in section 4.1.1. The efficiency of collecting signal events is estimated with the signal muon simulations. It includes track reconstruction efficiency, acceptance and analysis cut efficiencies, and trigger efficiencies. And lastly, as our signal event count includes both Z as well as W boson events, an estimated Z yield must be subtracted.

Table 5.4 shows generated events and analysis cut efficiencies determined from simulation. Additionally it shows trigger efficiencies, charge reconstruction effects, and the contribution from Z to be subtracted. These efficiencies can then be used along with the signal yield from the reduced dataset and the data luminosity to calculate the $W^{\pm}$ cross sections.

The systematic uncertainties for the cross section come from factors from several steps in the analysis process. The following list describes how the uncertainty is estimated for each of these factors. Some of these factors are uncertainties for the asymmetry calculation as well and their descriptions can be found in section 5.3.

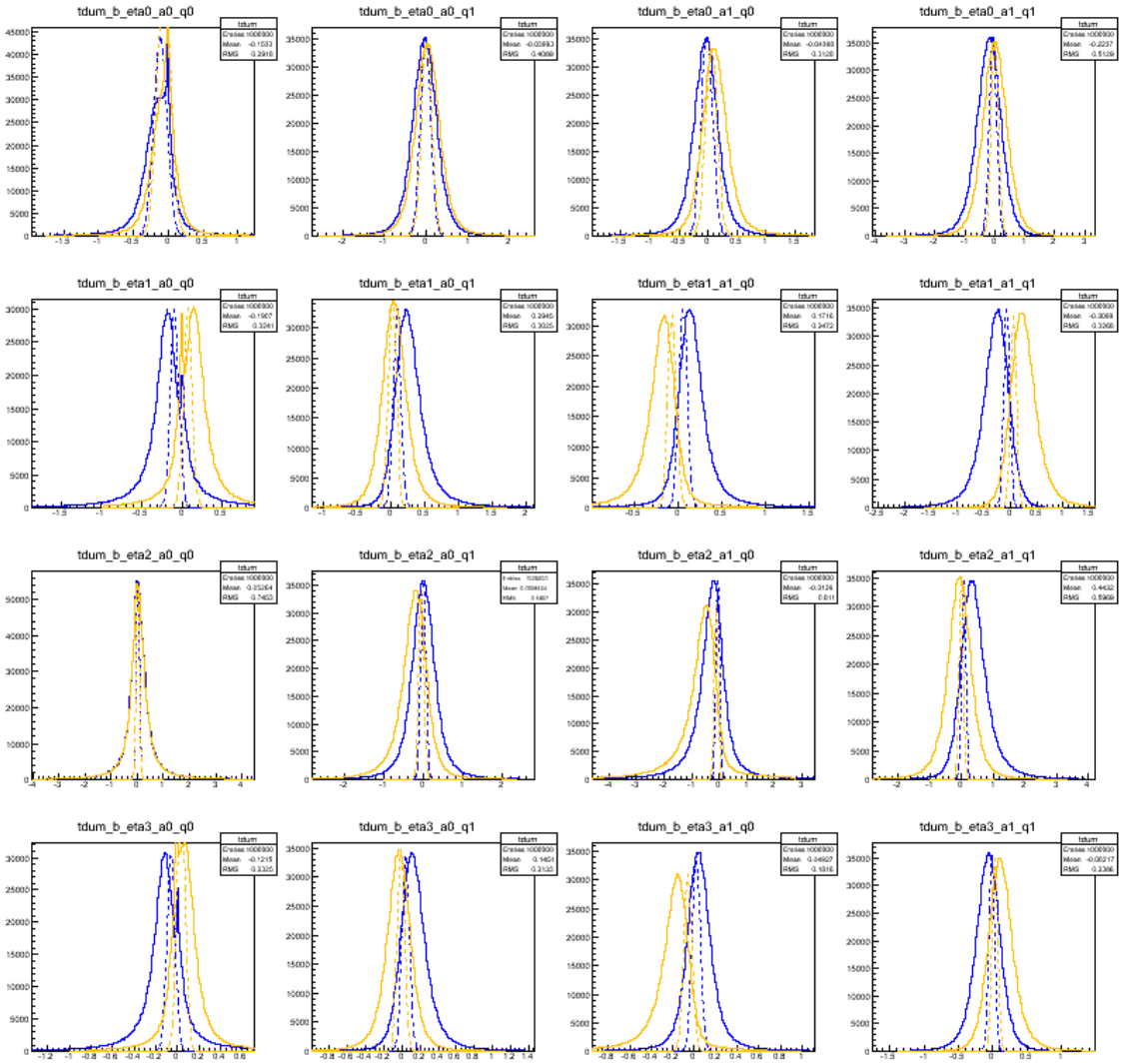

Figure 5.14: Taken from [44]. Asymmetry distributions when sampling asymmetries around their central value according to statistical uncertainties and charge reconstruct on uncertainties and background correcting them via sampling signal to background values according to their uncertainties when including fit, smearing and muon uncertainties in it. For each arm, charge and eta bin, the blue and yellow curves show the distributions while the dashed distributions show the distributions of the statistical uncertainties only normalized to the same height.

Table 5.4: Pythia+PISA based $W \to \mu$ acceptance and efficiencies as well as z fractions for the 2013 running period

Arm, Charge	South μ^-	South μ^+	North μ^-	North μ^+
charge ratio	0.240	0.760	0.240	0.760
BR:	0.106	0.106	0.106	0.106
total W gen		338100000		
gen events	599741	1901861	599741	1901861
rec events	465256	463108	375262	363348
cut/acc effi	5.430e-02	1.705e-02	4.380e-02	1.337e-02
trig/etc effi	2.763e-01	2.856e-01	3.316e-01	3.356e-01
total effi	1.501e-02	4.868e-03	1.452e-02	4.489e-03
diag charge effi	9.809e-01	9.805e-01	9.902e-01	9.900e-01
Z fraction	1.703e-01	1.627e-01	1.678e-01	1.549e-01

- **Momentum Smearing in the MuTr**
  - As described in section 5.3
- **Fixed Muon Background Yield**
  - As described in section 5.3
- **Trigger Efficiencies**
  - As described in section 5.3
- **Signal to Background Ratio - EML Fit**
  - As discussed in section 5.1.2.3.1, a test is done of performing the EML fit with only simulated data for all components. The fit consistently overestimated the actual yield of the signal muon simulation. The amount of this discrepancy is taken as another systematic contribution (but only in one direction because of consistent overestimation)
- **Dependence on Reference Run**
  - The Simulations are tuned to match sample data. To account for different rate-dependent responses, three "reference" runs are chosen from the 2012 run with low, medium and high rates. Simulations are then separately produced that are tuned to each of these reference runs. Again, the EML fit is performed and signal yields extracted for each case and the resulting variation is taken as systematic. As a note, however, the simulation does take rate dependent effects in to account in principle. So it's possible this contribution is an unnecessary overestimation of uncertainty.
- **Charge Reconstruction Efficiency**
  - As discussed in section 4.5.2, simulations show a higher charge reconstruction efficiency than measured in cosmic data which at the highest p_T dips to around 80%. To test conservatively, a CRE of 80% is propagated through the analysis and resulting variation is taken as a systematic.

- **Z Cross section**
  - At PHENIX, it's not possible to distinguish the contribution of Z events from the W signal. So the Z contribution is subtracted from the signal according to simulation, so the Z events are also simulated and accounted for in the analysis. But in addition to using PYTHIA as an event generation a RHIC tuned event generator, called RHICBOS, can separately be used for simulations. The difference in Z cross section, and resulting Z yield, between the two generators is then used as a systematic contribution.
- **Luminosity**
  - The luminosity calculation discussed in section 4.1.1 is based on previous PHENIX measurements. Similarly, the systematic uncertainty associated with luminosity is based on uncertainties from previous measurements. The 2009 $W \rightarrow e$ analysis[46], whose luminosity calculation was followed, has published a luminosity uncertainty of 15%. This uncertainty is used as a conservative estimate of the systematic uncertainty for luminosity.

The results of these uncertainty estimates are found in figures 5.15(for $W_{ness} > 0.92$) and 5.16(for $W_{ness} > 0.99$). Similar to the asymmetry systematics calculation, a Gaussian sampling is performed to combine the various contributions to a final cross section uncertainty (also seen in figures 5.15, 5.16). The final results for the $W^{\pm}$ cross sections can then be seen in figures 5.17 ($W_{ness} > 0.92$) and 5.18($W_{ness} > 0.99$) along with the cross section results from previous PHENIX measurements (other labeled data points) and multiple cross sections calculated from theory.

As can be seen, the systematic uncertainties are larger than previous PHENIX measurements, which is expected given the lower signal occurance and high background at forward rapidity. In both W_{ness} cuts, the measured values tend to be larger than theoretical calculations but are consistent within uncertianty bands. A significant discrepancy would be a sign that the analysis procedure had faults that would need revision. In the case of $W_{ness} > 0.92$, the results are barely within uncertainty bands of the theory values while the 0.99 cut has better consistency and smaller uncertainties. This is taken as further validation of the choice of 0.99 for the W_{ness} threshold.

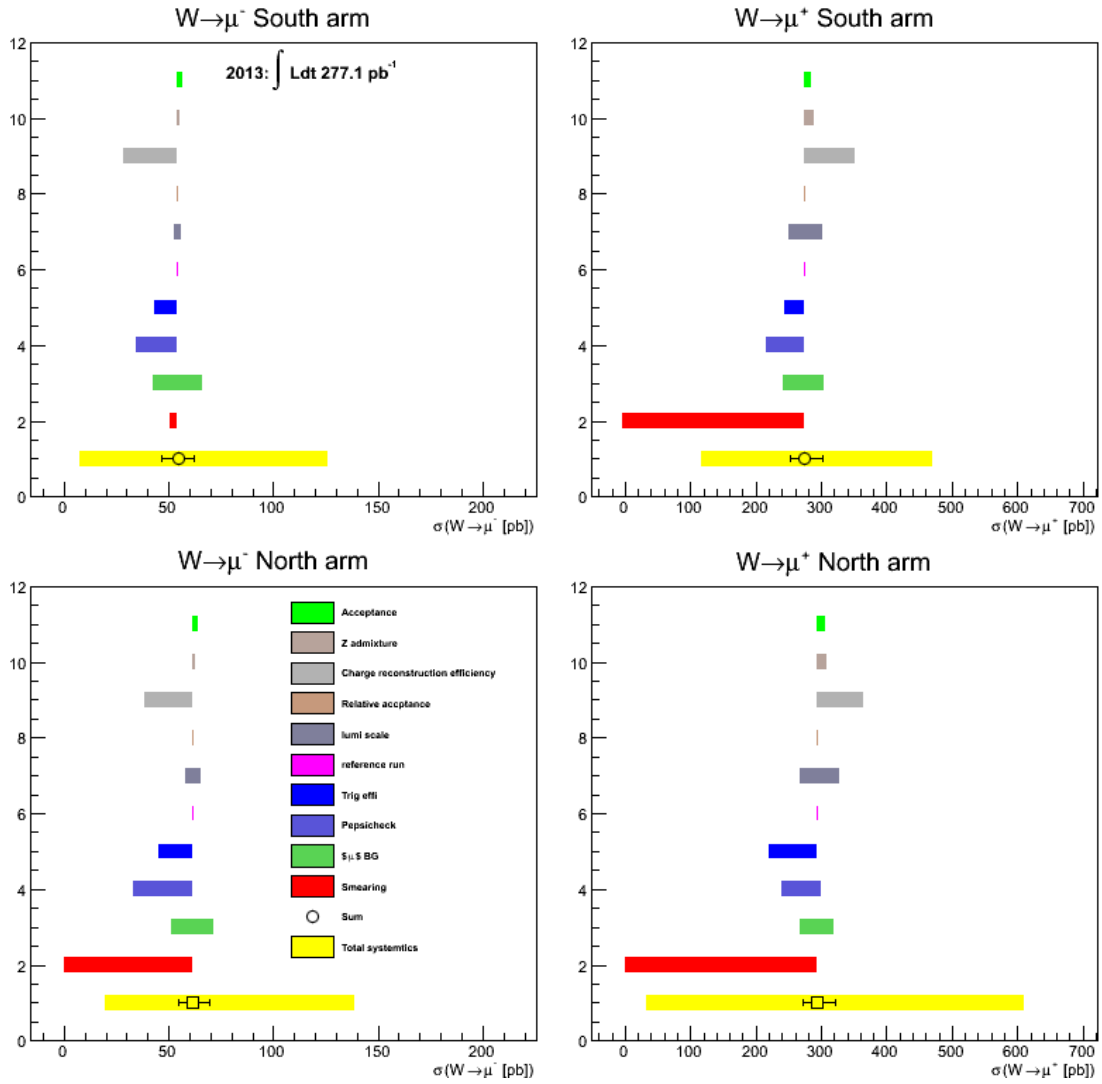

Figure 5.15: Individual systematic uncertainty contributions for each arm and charge when using a wness selection of 0.92.

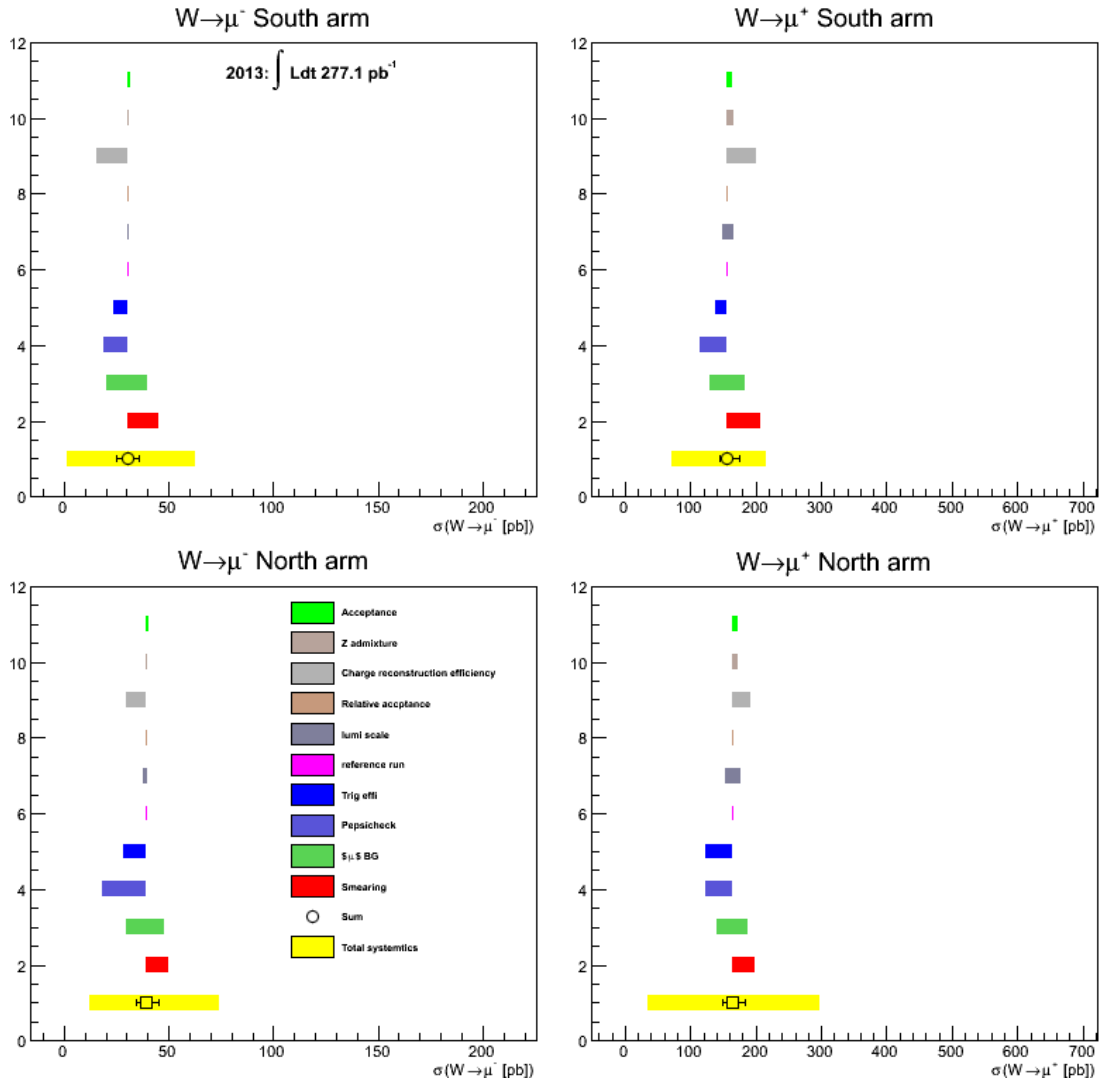

Figure 5.16: Individual systematic uncertainty contributions for each arm and charge when using a wness selection of 0.99.

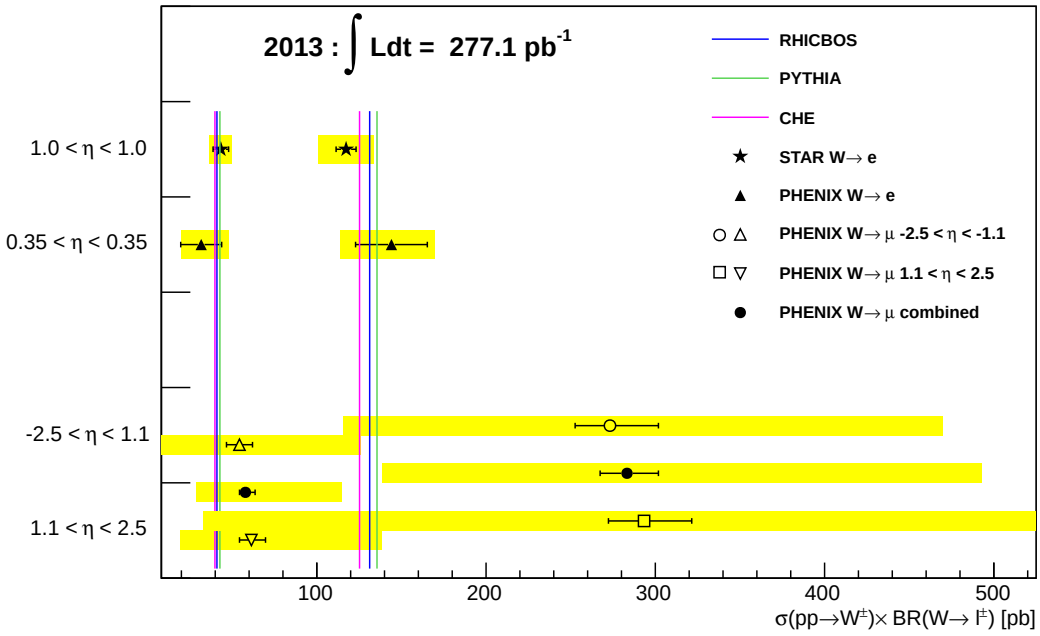

Figure 5.17: Extracted $pp \to W \times \mathrm{BR}(W \to l)$ cross sections for forward (downward open triangles and squares) and backward muons (upward open triangles and circles) when slecting wness values above 0.99 as well as combined (filled circles). For comparison the published results from PHENIX (filled triangles) and STAR (filled stars) as well as predictions by NLO generators CHI (purple lines) and RHICBOS(blue lines) and Pythia6.4 (green lines) are shown.

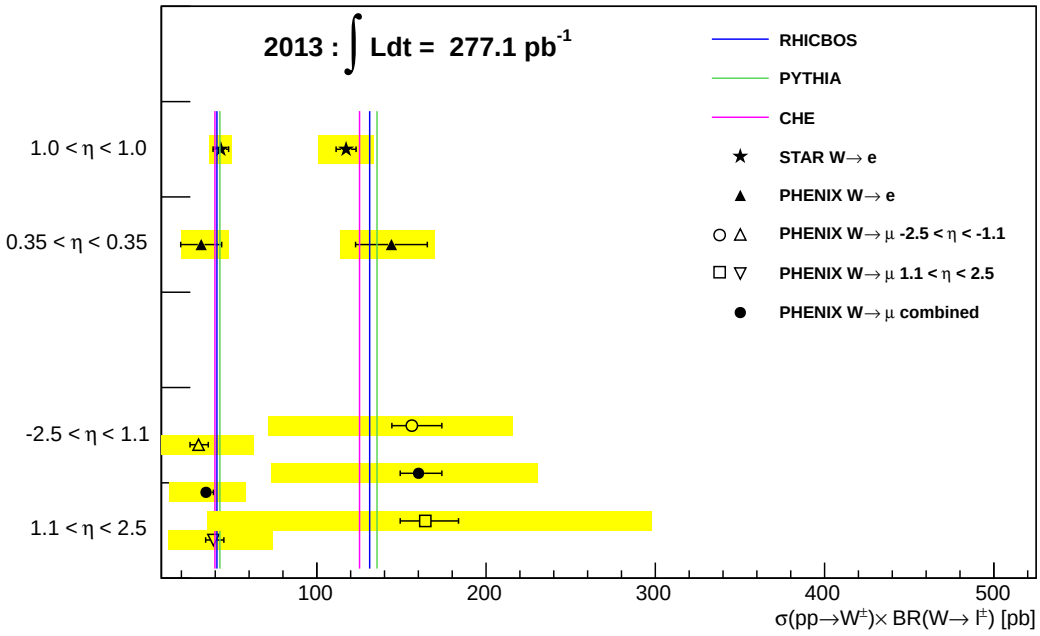

Figure 5.18: Extracted $pp \to W \times \mathrm{BR}(W \to l)$ cross sections for forward (downward open triangles and squares) and backward muons (upward open triangles and circles) as well as combined (filled circles) when slecting wness values above 0.99. For comparison the published results from PHENIX (filled triangles) and STAR (filled stars) as well as predictions by NLO generators CHI (purple lines) and RHICBOS(blue lines) and Pythia6.4 (green lines) are shown.

Chapter 6

Results and Outlook

6.1 A_L^W Results and Projected Impact

The following results are PHENIX preliminary results that were presented at the 21st International Symposium on Spin Physics, 2014 in Beijing[1]. The results are presently being prepared for publication in Phy. Rev. Lett. . Below are plots showing final values for A_L^W (along with statistical and systematic uncertainties) as a function of η separately for positive and negative charge. Two cases are shown: Figure 6.1 shows A_L^W in three η bins. Figure 6.2 combines the result to one η bin. In both cases, results from other RHIC measurements at central rapidity ranges are shown as well as predicted curves from various global fits. The asymmetry values are also listed in tables 6.2 and 6.1 for the three η bin and the combined η bin case respectively.

As can been seen, the systematic uncertainty dominates over statistical uncertainty and the magnitude of the uncertainty is large. Most of the data points are within error bounds of the theoretical predictions with the exception of some discrepancy in the negative rapidity of the W^+ case. As described in section 2.1.5, these A_L^W measurements will be used as input to global fits in order to constrain spin-dependent parton distribution functions. This discrepancy is a possible qualitative indicator that our data points capture information not yet contained in the theoretical models. However, a more quantitative assessment of the impact of this measurement on parton helicity distributions follows below.

While the new PHENIX data have not been included in the fit at this point in time, the DSSV group has projected the impact PHENIX and STAR data(the same STAR data points seen as reference in figures 6.2, 6.1) will have on the uncertainties for the quark and anti-quark helicity distributions. The results of this analysis are shown in figure 6.3. The error bounds from the DSSV analysis without the W-data are shown in yellow and the error bounds including the projected W-data from PHENIX and STAR are shown in red. As the STAR data points have already been published, their impact has been evaluated directly. Figure 6.4 shows (left) the difference in the NNPDF global-fit-derived $\Delta\bar{u}$ and $\Delta\bar{d}$ spin-dependent PDF's before (green) and after (red) including the STAR data points. The NNPDF results including this STAR data as well as

[1]Talk by Dr. Francesca Giordano, UIUC

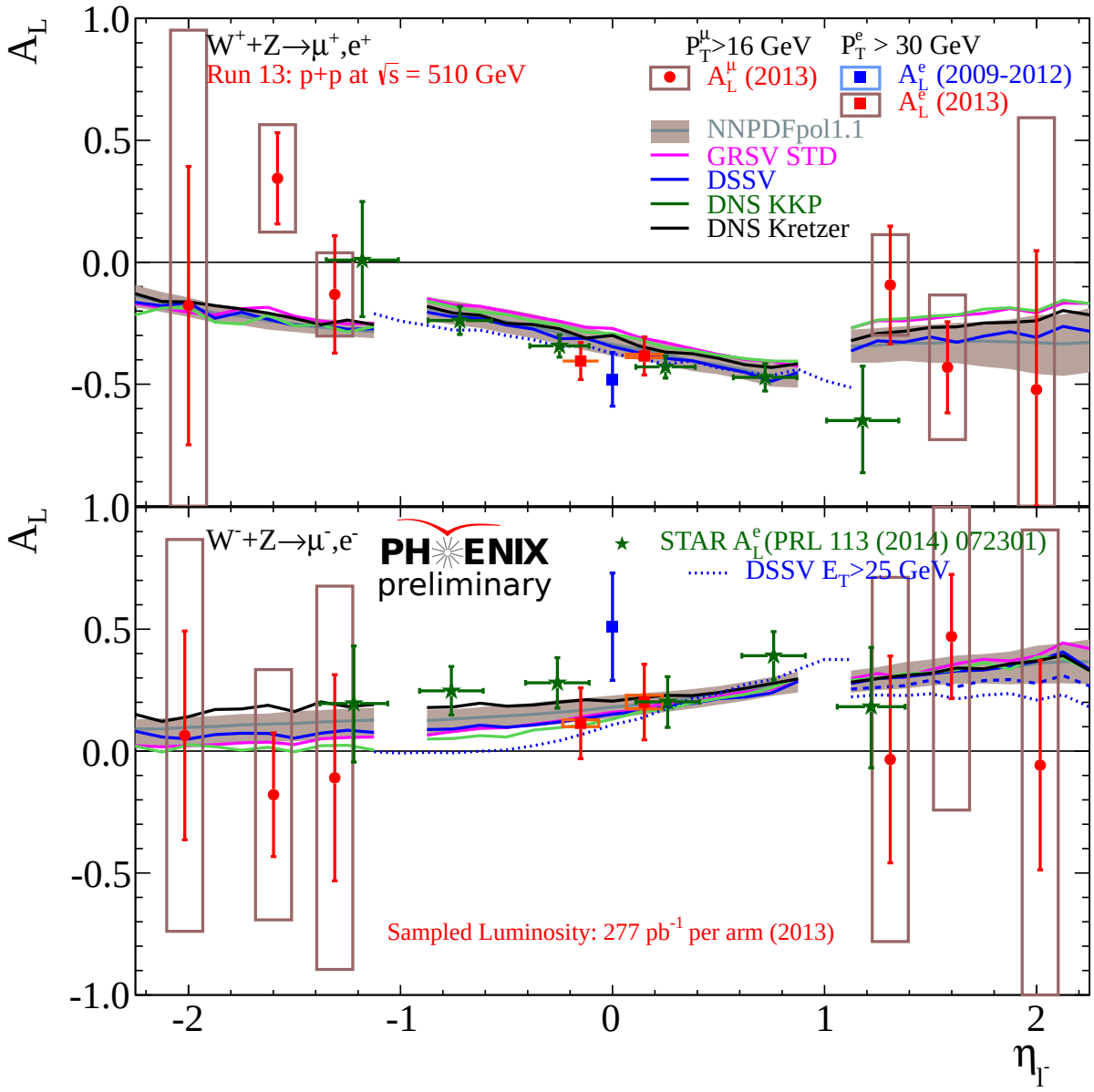

Figure 6.1: Preliminary single spin asymmetries for run12 (blue markers) and new preliminary results for run13 (red markers, shown for 3 separate η bins) using a $W_{ness} > 0.99$ selection, as well as published run12 STAR results and central W results. The top plot displays the $W^+/Z \to \mu^+$ asymmetries, the bottom plot displays the $W^-/Z \to \mu^-$ asymmetries. Background dilution was corrected with the unbinned maximum likelihood based S/BG method with the full systematic uncertainties, the S/BG uncertainty and the charge reconstruction uncertainty as described in the text.

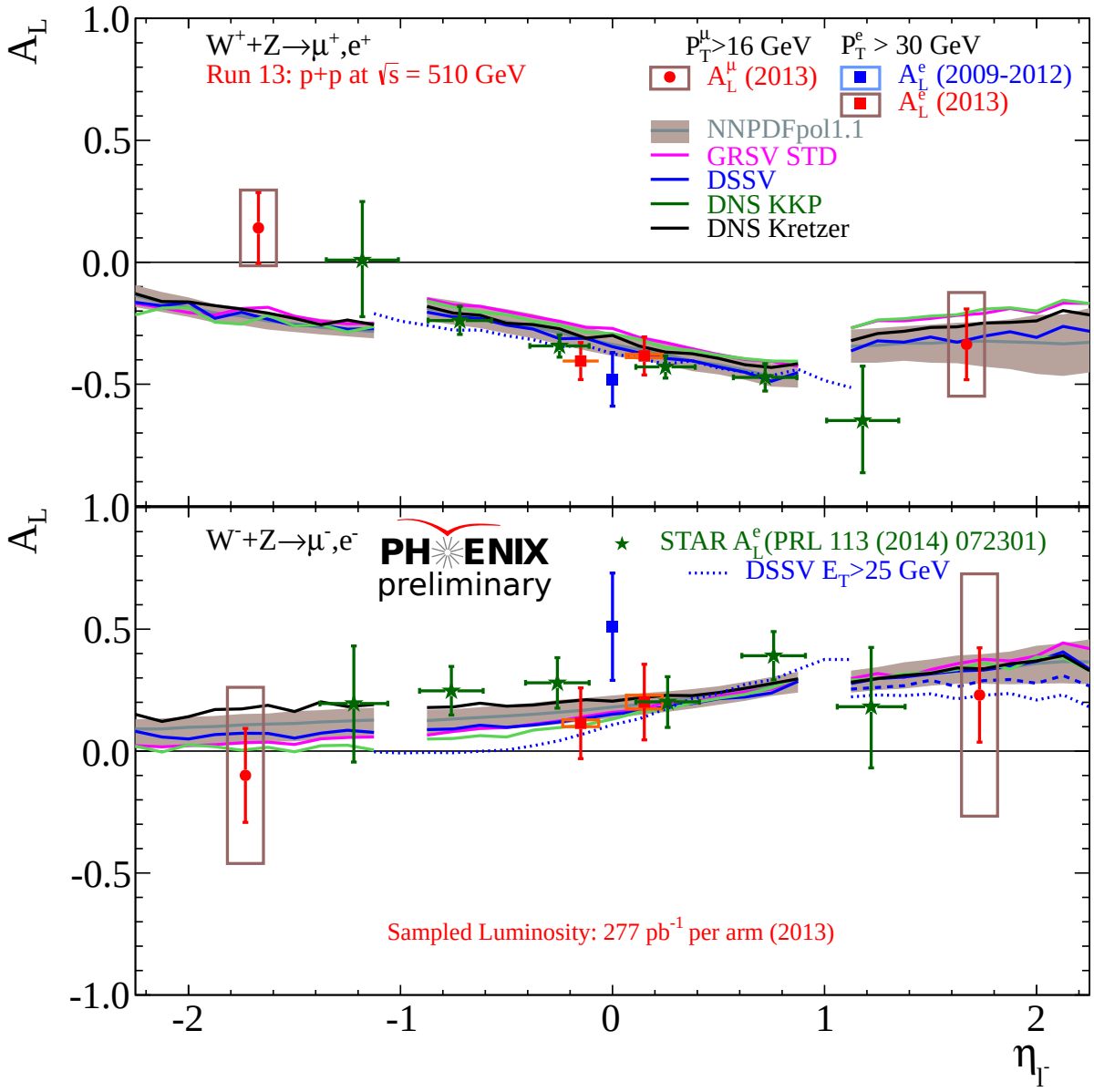

Figure 6.2: Preliminary single spin asymmetries for run12 (blue markers) and new preliminary results for run13 (red markers, shown for only 1 bin in η) using a $W_{ness} > 0.99$ selection, as well as published run12 STAR results and central W results. The top plot displays the $W^+/Z \to \mu^+$ asymmetries, the bottom plot displays the $W^-/Z \to \mu^-$ asymmetries. Background dilution was corrected with the unbinned maximum likelihood based S/BG method with the full systematic uncertainties, the S/BG uncertainty and the charge reconstruction uncertainty as described in the text.

Table 6.1: BG corrected single spin asymmetries A_L for the whole eta range as a function of rapidity with minimum transverse momentum of 16 GeV/c with and without combining the two beams and using a minimum W likelihood cut level of $W_{ness} > 0.99$. The signal to background values were extracted from the MC based signal and data, the uncertainty on the S/BG value from the fit is given as a systematic uncertainty.

Arm/charge	beam	etabin	eta	S/BG	raw A_L	corrected A_L
N^+	B	1.10-2.60	1.68	$0.50^{0.11}_{0.16}$	-0.057 ± 0.037	$-0.327 \pm 0.21^{0.08}_{0.08}$
S^+	Y	1.10-2.60	1.66	$0.50^{0.13}_{0.14}$	-0.063 ± 0.037	$-0.346 \pm 0.20^{0.20}_{0.20}$
FW^+	comb	1.10-2.60	1.67			$-0.337 \pm 0.15^{0.22}_{-0.22}$
S^+	B	1.10-2.60	-1.66	$0.50^{0.13}_{0.14}$	0.015 ± 0.037	$0.087 \pm 0.21^{0.08}_{0.08}$
N^+	Y	1.10-2.60	-1.68	$0.50^{0.11}_{0.16}$	0.035 ± 0.037	$0.194 \pm 0.20^{0.14}_{0.14}$
BW^+	comb	1.10-2.60	-1.67			$0.141 \pm 0.15^{0.16}_{-0.16}$
N^-	B	1.10-2.60	1.74	$0.45^{0.18}_{0.20}$	0.039 ± 0.041	$0.247 \pm 0.25^{0.16}_{0.16}$
S^-	Y	1.10-2.60	1.72	$0.30^{0.12}_{0.21}$	0.026 ± 0.041	$0.214 \pm 0.32^{0.50}_{0.50}$
FW^-	comb	1.10-2.60	1.73			$0.233 \pm 0.20^{0.52}_{-0.52}$
S^-	B	1.10-2.60	-1.72	$0.30^{0.12}_{0.21}$	-0.016 ± 0.041	$-0.134 \pm 0.33^{0.30}_{0.30}$
N^-	Y	1.10-2.60	-1.74	$0.45^{0.18}_{0.20}$	-0.012 ± 0.041	$-0.076 \pm 0.24^{0.24}_{0.24}$
BW^-	comb	1.10-2.60	-1.73			$-0.101 \pm 0.19^{0.38}_{-0.38}$

other modern measurements were shown in figure 2.3 as discussed in section 2.1.5.

Furthermore, it has been studied to what extend the W-data from RHIC will contribute to constraining a possible asymmetry for the helicity sea quark distributions, $\Delta\bar{u}(x) - \Delta\bar{d}(x)$. The results from the NNPDF group for this difference are shown in figure 6.5 , including projected W-data from RHIC (red) and including only current RHIC data (green). The uncertainties in the sea quark asymmetry will be reduced only by 30-40%. Nevertheless it might be possible to observe an asymmetry at the 2 sigma level. This comparison of $\Delta\bar{u}(x) - \Delta\bar{d}(x)$ also serves as a projection of the 2013 RHIC data impact (indirectly) on helicity distribution constraints as determined by the NNPDF group using different techniques than the DSSV group.

6.2 Outlook

As mentioned, the PHENIX A_L^W results are preliminary and have been presented at Spin 2014. There are some open analysis questions that are currently being addressed, particularly in regards to finalizing systematic uncertainties. This work is nearing completion and is expected to move toward publication this fall (2016).

Projections were given for the expected impact of PHENIX A_L^W results on the determined helicity

Table 6.2: BG corrected single spin asymmetries A_L in the 3 eta bins as a function of rapidity with minimum transverse momentum of 16 GeV/c with and without combining the two beams and using a minimum W likelihood cut level of $W_{ness} > 0.99$. The signal to background values were extracted from the MC based signal and data, the uncertainty on the S/BG value from the fit is given as a systematic uncertainty.

Arm/charge	beam	etabin	eta	S/BG	raw A_L	corrected A_L
N^+	B	1.10-1.40	1.31	$1.18^{0.26}_{0.44}$	-0.105 ± 0.094	$-0.366 \pm 0.32^{0.09}_{0.09}$
S^+	Y	1.10-1.40	1.31	$0.91^{0.24}_{0.23}$	0.059 ± 0.099	$0.227 \pm 0.38^{0.20}_{0.20}$
FW^+	comb	1.10-1.40	1.31			$-0.094 \pm 0.24^{0.22}_{-0.22}$
S^+	B	1.10-1.40	-1.31	$0.91^{0.24}_{0.23}$	-0.020 ± 0.099	$-0.075 \pm 0.38^{0.13}_{0.13}$
N^+	Y	1.10-1.40	-1.31	$1.18^{0.26}_{0.44}$	-0.053 ± 0.094	$-0.181 \pm 0.31^{0.12}_{0.12}$
BW^+	comb	1.10-1.40	-1.31			$-0.133 \pm 0.24^{0.18}_{-0.18}$
N^-	B	1.10-1.40	1.31	$0.75^{0.30}_{0.39}$	-0.015 ± 0.124	$-0.058 \pm 0.54^{0.37}_{0.37}$
S^-	Y	1.10-1.40	1.31	$0.44^{0.18}_{0.32}$	-0.000 ± 0.122	$-0.003 \pm 0.72^{0.69}_{0.69}$
FW^-	comb	1.10-1.40	1.31			$-0.035 \pm 0.43^{0.78}_{-0.78}$
S^-	B	1.10-1.40	-1.31	$0.44^{0.18}_{0.32}$	-0.061 ± 0.123	$-0.370 \pm 0.74^{0.70}_{0.70}$
N^-	Y	1.10-1.40	-1.31	$0.75^{0.30}_{0.39}$	0.015 ± 0.124	$0.071 \pm 0.53^{0.45}_{0.45}$
BW^-	comb	1.10-1.40	-1.31			$-0.111 \pm 0.43^{0.83}_{-0.83}$
N^+	B	1.40-1.80	1.58	$0.54^{0.12}_{0.18}$	-0.091 ± 0.053	$-0.502 \pm 0.28^{0.12}_{0.12}$
S^+	Y	1.40-1.80	1.58	$0.55^{0.16}_{0.14}$	-0.070 ± 0.049	$-0.366 \pm 0.25^{0.28}_{0.28}$
FW^+	comb	1.40-1.80	1.58			$-0.431 \pm 0.19^{0.30}_{-0.30}$
S^+	B	1.40-1.80	-1.58	$0.55^{0.16}_{0.14}$	0.056 ± 0.049	$0.297 \pm 0.26^{0.11}_{0.11}$
N^+	Y	1.40-1.80	-1.58	$0.54^{0.12}_{0.18}$	0.075 ± 0.053	$0.394 \pm 0.27^{0.20}_{0.20}$
BW^+	comb	1.40-1.80	-1.58			$0.344 \pm 0.19^{0.22}_{-0.22}$
N^-	B	1.40-1.80	1.59	$0.50^{0.20}_{0.23}$	0.086 ± 0.060	$0.497 \pm 0.33^{0.22}_{0.22}$
S^-	Y	1.40-1.80	1.61	$0.33^{0.14}_{0.23}$	0.061 ± 0.057	$0.454 \pm 0.41^{0.71}_{0.71}$
FW^-	comb	1.40-1.80	1.60			$0.478 \pm 0.26^{0.75}_{-0.75}$
S^-	B	1.40-1.80	-1.61	$0.33^{0.14}_{0.23}$	-0.067 ± 0.056	$-0.510 \pm 0.42^{0.43}_{0.43}$
N^-	Y	1.40-1.80	-1.59	$0.50^{0.20}_{0.23}$	0.014 ± 0.060	$0.071 \pm 0.33^{0.33}_{0.33}$
BW^-	comb	1.40-1.80	-1.60			$-0.182 \pm 0.26^{0.54}_{-0.54}$
N^+	B	1.80-2.60	2.01	$0.16^{0.05}_{0.03}$	0.016 ± 0.064	$0.223 \pm 0.86^{0.59}_{0.59}$
S^+	Y	1.80-2.60	1.99	$0.19^{0.09}_{0.04}$	-0.108 ± 0.070	$-1.239 \pm 0.80^{1.11}_{1.11}$
FW^+	comb	1.80-2.60	2.00			$-0.534 \pm 0.58^{1.25}_{-1.25}$
S^+	B	1.80-2.60	-1.99	$0.19^{0.09}_{0.04}$	-0.049 ± 0.070	$-0.581 \pm 0.81^{0.94}_{0.94}$
N^+	Y	1.80-2.60	-2.01	$0.16^{0.05}_{0.03}$	0.016 ± 0.064	$0.232 \pm 0.84^{0.82}_{0.82}$
BW^+	comb	1.80-2.60	-2.00			$-0.182 \pm 0.58^{1.24}_{-1.24}$
N^-	B	1.80-2.60	2.04	$0.27^{0.11}_{0.09}$	0.000 ± 0.065	$-0.003 \pm 0.56^{0.50}_{0.50}$
S^-	Y	1.80-2.60	1.99	$0.21^{0.10}_{0.13}$	-0.013 ± 0.066	$-0.128 \pm 0.69^{0.92}_{0.92}$
FW^-	comb	1.80-2.60	2.02			$-0.059 \pm 0.44^{1.04}_{-1.04}$
S^-	B	1.80-2.60	-1.99	$0.21^{0.10}_{0.13}$	0.066 ± 0.066	$0.711 \pm 0.70^{0.66}_{0.66}$
N^-	Y	1.80-2.60	-2.04	$0.27^{0.11}_{0.09}$	-0.050 ± 0.065	$-0.440 \pm 0.55^{0.57}_{0.57}$
BW^-	comb	1.80-2.60	-2.02			$0.065 \pm 0.43^{0.87}_{-0.87}$

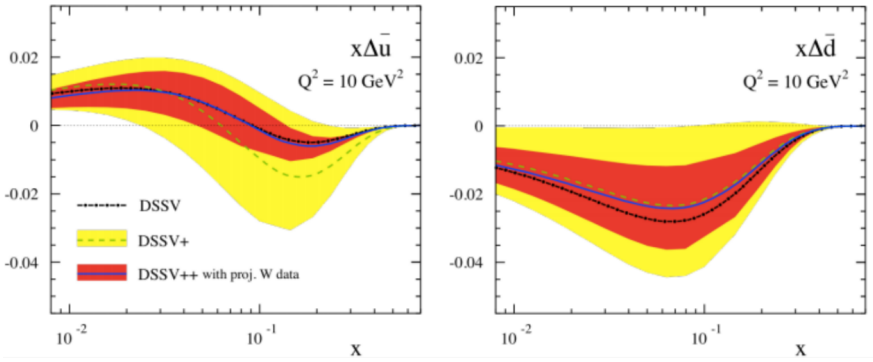

Figure 6.3: Taken from [47]. Projected impact of PHENIX and STAR A_L^W measurements on the uncertainty of $\Delta\bar{u}$ and $\Delta\bar{d}$ by the DSSV global fit. Current uncertainty bands shown in yellow and projected reduced uncertainty is the red bands.

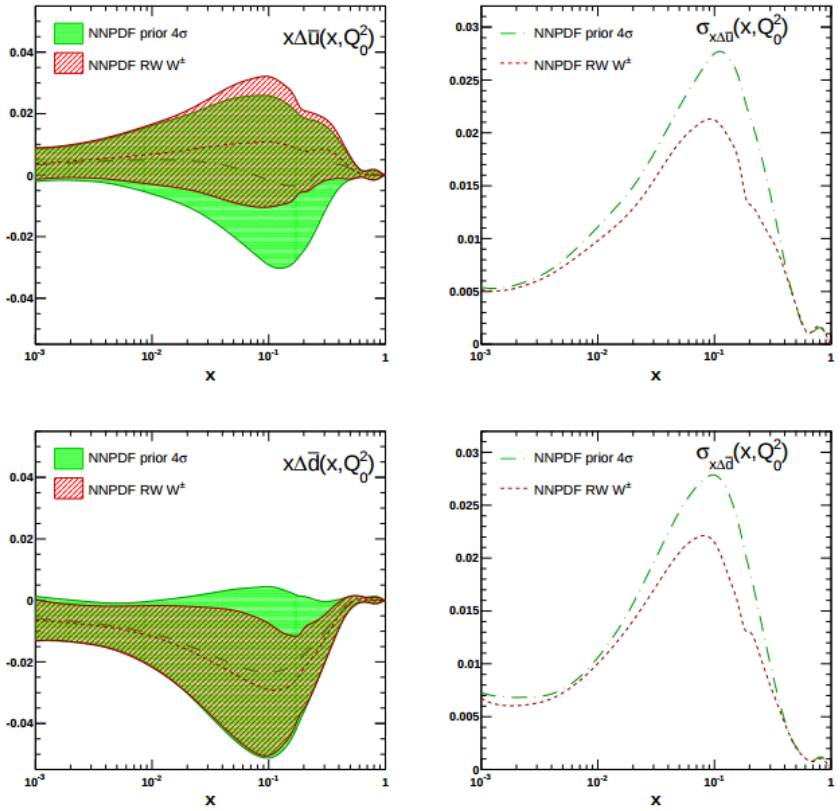

Figure 6.4: Taken from [18]. NNPDF impact of 2012 STAR A_L^W results on $\Delta\bar{u}$ and $\Delta\bar{d}$ (left plots). Prior results are in green and results with STAR data are in red. Magnitude of uncertainty bands are plotted in the right plots.

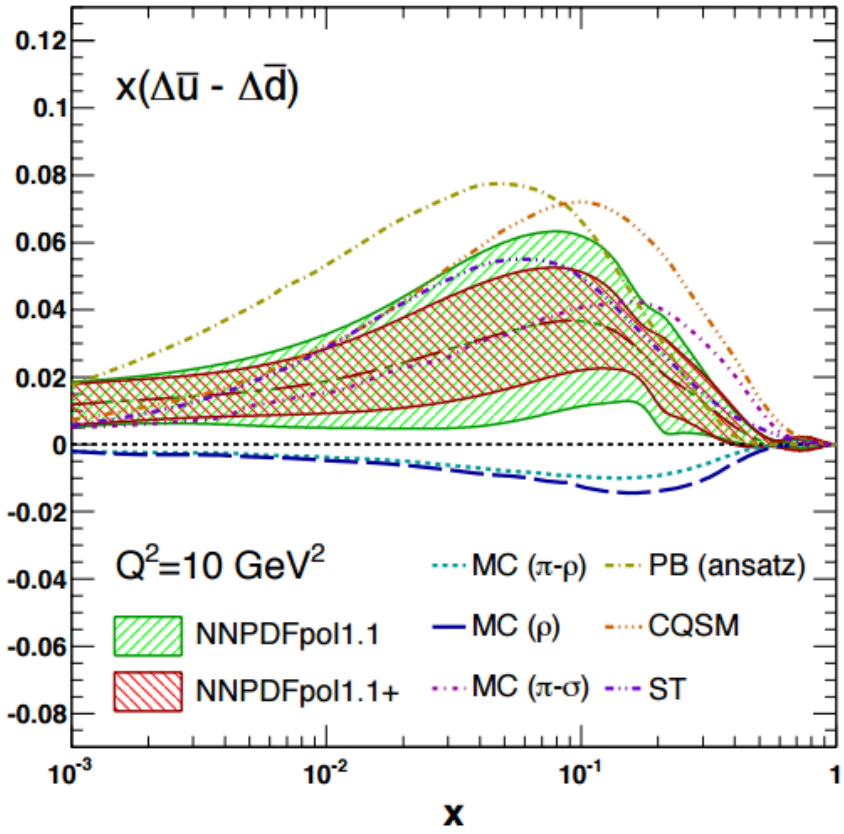

Figure 6.5: Taken from [48]. $\Delta\bar{u}(x) - \Delta\bar{d}(x)$ distribution from global data including currently published RHIC data (green) compared with projected impact of 2013 RHIC data.

distributions from global fits of available experimental data. As can perhaps be inferred from this, groups performing these global fits have machinery in place that is ready to include PHENIX data. Once PHENIX's measurement is published, it is expected that publication of updated global fit results from the DSSV and NNPDF groups will follow quickly.

Looking ahead, there are proposals and work toward future experiments that will build further on these results, namely the 12 GeV electron beam upgrade at Jefferson Lab[49] and the Electron Ion Collider [50]. In the near term, the Jefferson Lab upgrade take data with the newly upgraded 12 GeV high intensity, high polarization CEBAF electron accelerator for fixed target DIS and SIDIS experiments. The large luminosities and high resolution availible from this upgrade will extend the kinematic reach of helicity distribution measurements to a factor of 2 small x and to larger x than is currently available[50]. In the medium term, a polarized electron-ion collider is proposed to be built as an extension of either RHIC or CEBAF. This facility will offer much larger Q^2 scattering at a much lower x range than what is currently possible. Figure 6.6(left) shows this extended kinematic reach relative to current measurements and 6.6(right) shows the corresponding anticipated improvement in constraint of the spin contribution gluon(ΔG) and the summed quark contribution ($\Delta \sum$) to the proton spin. Figure 6.7 shows expected improvement on constraints of individual spin-dependent PDF's.

It's clear that these future measurements will continue to improve the precision of our knowledge of anti quark helicity distributions (as well as others, notably the gluon helicity distribution). But further still, they will offer first tools to consider proton structure in detail under a new paradigm of three dimensionality. Both experiments will have physics goals related to transverse spin and transverse momentum in the proton, as well as beginning to spatially image the distribution of sea quarks and gluons. These types of studies will open the door to the next level of understanding of the comprehensive structure of nucleons. A detailed description of the physics capabilities of the EIC can be found in the EIC white paper [50]

6.3 Conclusion

As this dissertation has reported, the measurement of single spin asymmetries in $W^{\pm}$ production allows fairly direct access to anti quark helicity distributions. The unique ability of RHIC to provide $\sqrt{s} = 510$ GeV polarized proton collisions and PHENIX's forward-rapidity muon arm trigger upgrades allowed sufficient data to be taken for this measurement in 2013. Analysis of this data has been performed and preliminary results have been released. With further refining of the analysis currently underway, final results are anticipated to be ready to submit for publication in the near future.

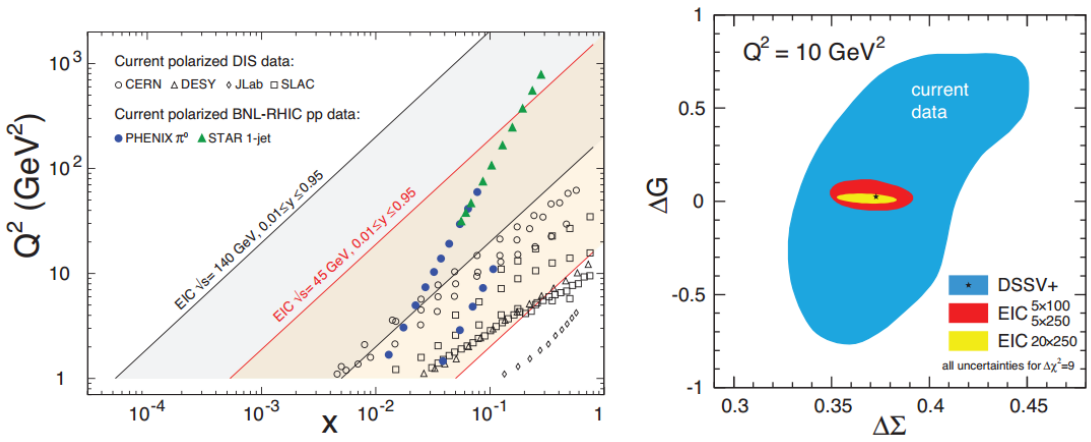

Figure 6.6: Taken from [50]. Left plot: projected kinematic reach of EIC measurements compared with RHIC and DIS results. Right plot: projected constraints on quark and gluon spin contributions from EIC measurements compared with current results according to the DSSV global fit.

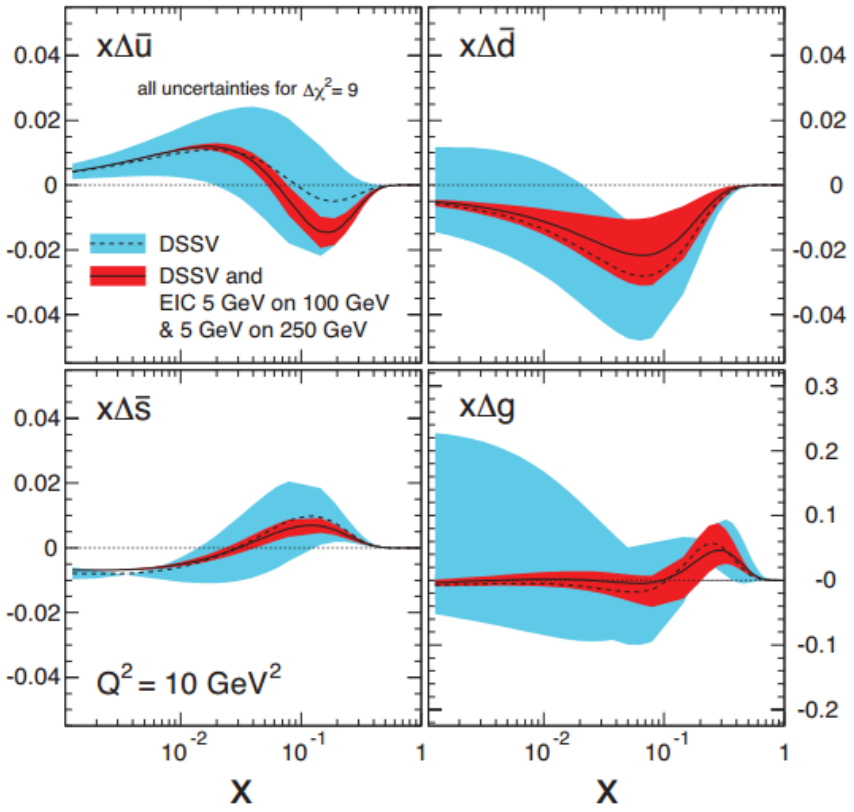

Figure 6.7: Taken from [50]. Projected impact from EIC measurements on sea quark and gluon PDF's according to the DSSV global fit. Current results are in blue and projected results are in red.

PHENIX's A_L^W measurement is projected to improve $\Delta\bar{u}$ and $\Delta\bar{d}$ constraints as in fact complimentary RHIC measurements already have. Preparation is already underway on future projects such as high lumi-

nosity SIDIS experiments in the 12 GeV upgrade at Jefferson Lab and the eventual Electron Ion Collider both of which will offer new insights in to various aspects of the proton's internal structure, including an even more precise measurements of spin-dependent PDF's.

This work has been an important step in a continuing, long-term effort to understand the spin of the proton.

References

[1] Richard P. Feynman. Very high-energy collisions of hadrons. *Phys. Rev. Lett.*, 23:1415–1417, Dec 1969.

[2] J. Ashman, B. Badelek, G. Baum, et al. A measurement of the spin asymmetry and determination of the structure function g1 in deep inelastic muon-proton scattering. *Physics Letters B*, 206(2):364 – 370, 1988.

[3] M. Gell-Mann. A schematic model of baryons and mesons. *Physics Letters*, 8(3):214 – 215, 1964.

[4] G Zweig. An SU_3 model for strong interaction symmetry and its breaking; Version 2. (CERN-TH-412):80 p, Feb 1964.

[5] M. A. B. Bég, B. W. Lee, and A. Pais. Su(6) and electromagnetic interactions. *Phys. Rev. Lett.*, 13:514–517, Oct 1964.

[6] Bunji Sakita. Electromagnetic properties of baryons in the supermultiplet scheme of elementary particles. *Phys. Rev. Lett.*, 13:643–646, Nov 1964.

[7] J. D. Bjorken. Asymptotic sum rules at infinite momentum. *Phys. Rev.*, 179:1547–1553, Mar 1969.

[8] E. D. Bloom, D. H. Coward, H. DeStaebler, et al. High-energy inelastic $e - p$ scattering at 6° and 10°. *Phys. Rev. Lett.*, 23:930–934, Oct 1969.

[9] M. Breidenbach, J. I. Friedman, H. W. Kendall, et al. Observed behavior of highly inelastic electron-proton scattering. *Phys. Rev. Lett.*, 23:935–939, Oct 1969.

[10] R.L. Jaffe and Aneesh Manohar. The g1 problem: Deep inelastic electron scattering and the spin of the proton. *Nuclear Physics B*, 337(3):509 – 546, 1990.

[11] S. E. Kuhn, J. P. Chen, and E. Leader. Spin Structure of the Nucleon - Status and Recent Results. *Prog. Part. Nucl. Phys.*, 63:1–50, 2009.

[12] Richard D. Ball, Stefano Forte, Alberto Guffanti, et al. Unbiased determination of polarized parton distributions and their uncertainties. *Nucl. Phys.*, B874:36–84, 2013.

[13] K. Abe, T. Akagi, P. L. Anthony, et al. Precision measurement of the deuteron spin structure function g_1^d. *Phys. Rev. Lett.*, 75:25–28, Jul 1995.

[14] B. Adeva, E. Arik, A. Arvidson, et al. The spin-dependent structure function g1(x) of the proton from polarized deep-inelastic muon scattering. *Physics Letters B*, 412(34):414 – 424, 1997.

[15] B. Adeva, T. Akdogan, E. Arik, et al. Polarised quark distributions in the nucleon from semi-inclusive spin asymmetries. *Physics Letters B*, 420(12):180 – 190, 1998.

[16] K. Ackerstaff, A. Airapetian, N. Akopov, et al. Flavor decomposition of the polarized quark distributions in the nucleon from inclusive and semi-inclusive deep-inelastic scattering. *Physics Letters B*, 464(12):123 – 134, 1999.

[17] A. Airapetian, N. Akopov, Z. Akopov, et al. Quark helicity distributions in the nucleon for up, down, and strange quarks from semi-inclusive deep-inelastic scattering. *Phys. Rev. D*, 71:012003, Jan 2005.

[18] Emanuele R. Nocera, Richard D. Ball, Stefano Forte, Giovanni Ridolfi, and Juan Rojo. A first unbiased global determination of polarized PDFs and their uncertainties. *Nucl. Phys.*, B887:276–308, 2014.

[19] Daniel de Florian, Rodolfo Sassot, Marco Stratmann, and Werner Vogelsang. Global analysis of helicity parton densities and their uncertainties. *Phys. Rev. Lett.*, 101:072001, Aug 2008.

[20] Daniel de Florian, Rodolfo Sassot, Marco Stratmann, and Werner Vogelsang. Extraction of spin-dependent parton densities and their uncertainties. *Phys. Rev. D*, 80:034030, Aug 2009.

[21] G. Bunce and et al. Plans for the rhic spin physics program. 2008.

[22] P.M. Nadolsky and C.-P. Yuan. Soft parton radiation in polarized vector boson production: theoretical issues. *Nuclear Physics B*, 666(12):3 – 30, 2003.

[23] P.M. Nadolsky and C.-P. Yuan. Single-spin physics with weak bosons at rhic. *Nuclear Physics B*, 666(12):31 – 55, 2003.

[24] Daniel de Florian and Werner Vogelsang. Helicity parton distributions from spin asymmetries in w-boson production at rhic. *Phys. Rev. D*, 81:094020, May 2010.

[25] M. Harrison, T. Ludlam, and S. Ozaki. Rhic project overview. *Nuclear Instruments and Methods in Physics Research Section A: Accelerators, Spectrometers, Detectors and Associated Equipment*, 499(23):235 – 244, 2003. The Relativistic Heavy Ion Collider Project: RHIC and its Detectors.

[26] I Alekseev, C Allgower, M Bai, et al. Polarized proton collider at rhic. *Nuclear Instruments and Methods in Physics Research Section A: Accelerators, Spectrometers, Detectors and Associated Equipment*, 499(23):392 – 414, 2003. The Relativistic Heavy Ion Collider Project: RHIC and its Detectors.

[27] K. Adcox, S.S. Adler, M. Aizama, et al. Phenix detector overview. *Nuclear Instruments and Methods in Physics Research Section A: Accelerators, Spectrometers, Detectors and Associated Equipment*, 499(23):469 – 479, 2003. The Relativistic Heavy Ion Collider Project: RHIC and its Detectors.

[28] A. Basye and et al. Conceptual design report for a fast muon trigger at phenix. 2007. www.phenix.bnl.gov/WWW/trigger/muonupgrade/CDR/CDR_final.pdf.

[29] Abraham Meles, Ralf Seidl, Francesca Giordano, et al. Run 13 $w \to \mu$. *PHENIX Analysis Note*, Mar 2014. https://www.phenix.bnl.gov/phenix/WWW/p/info/an/1137/Run13_WtoMu_vs2.1-02.pdf.

[30] Sanghwa Park. Measurement of the single spin asymmetry in w boson production in polarized p+p collisions at $\sqrt{s} = 510$ gev with the phenix muon spectrometer. *Ph.D. thesis at Seoul National University*, 2015. http://www.phenix.bnl.gov/phenix/WWW/talk/archive/theses/2015/Park_Sanghwa-Thesis_SPark_print_fin.pdf.

[31] Mickey Chiu, Matthias Grosse Perdekamp, and Scott Wolin. New ideas on relative luminosity determination in run09 500 gev polarized proton collisions. *PHENIX Analysis Note*, Apr 2014. https://www.phenix.bnl.gov/phenix/WWW/p/draft/chiu/notes/rel_lumi/scott_rl.pdf.

[32] Mike Beaumier. Probing the spin structure of the proton using polarized proton-proton collisions and the production of w bosons. *Ph.D. thesis at University of California Riverside (publication pending)*, 2016.

[33] Rhic polarimitry analysis note. https://wiki.bnl.gov/rhicspin/upload/e/e4/Pol_resultsMay2016.pdf.

[34] Rhic spin group wiki. https://wiki.bnl.gov/rhicspin/Results.

[35] Michael Beaumier, Ciprian Gal, Minjung Kim, et al. Run 13 spin database quality assurance. *PHENIX Analysis Note*, Mar 2014. https://www.phenix.bnl.gov/phenix/WWW/p/draft/rseidl/spin/Run13/main_1.1.pdf.

[36] Run 13 muon quality assurance. *PHENIX Analysis Note*. http://www.phenix.bnl.gov/phenix/WWW/p/info/an/1136/Run13qa_note_v0.pdf.

[37] Run 12 muon quality assurance. *PHENIX Analysis Note*. https://www.phenix.bnl.gov/phenix/WWW/p/info/an/1102/Run12MuonQA.pdf.

[38] Run 11 muon quality assurance. *PHENIX Analysis Note*. http://www.phenix.bnl.gov/phenix/WWW/p/info/an/1022/Run11MuonQA.pdf.

[39] Hideyuki Oide. Measurement of longitudinal spin asymmetry in production of muons from w/z boson decays in polarized p+p collisions at s = 500 gev with the phenix detector at rhic. *Ph.D. thesis at RIKEN (The Institute of Physical and Chemical Research)*, 2013. http://www.phenix.bnl.gov/phenix/WWW/talk/archive/theses/2013/Oide_Hideyuki-thesis.pdf.

[40] R. E. Kalman. A new approach to linear filtering and prediction problems. *ASME Journal of Basic Engineering*, 82(1):35–45, 1960.

[41] Sanghwa Park. Measurement of the single spin asymmetry in w boson production in polarized p+p collisions at $\sqrt{s}$ = 510 gev with the phenix muon spectrometer. *Ph.D. thesis at Seoul National University*, 2015. http://www.phenix.bnl.gov/phenix/WWW/talk/archive/theses/2015/Park_Sanghwa-Thesis_SPark_print_fin.pdf.

[42] Torbjrn Sjstrand, Stephen Mrenna, and Peter Skands. Pythia 6.4 physics and manual. *Journal of High Energy Physics*, 2006(05):026, 2006.

[43] Xiaochun He and Murad Sarsour. Run 11 cosmic ray background analysis. *PHENIX Analysis Note*, Feb 2012. https://www.phenix.bnl.gov/phenix/WWW/p/info/an/1014/run11CosmicAnalysis_sarsour.pdf.

[44] Abraham Meles, Ralf Seidl, Francesca Giordano, et al. Run 13 $w \to \mu$ - updated. *PHENIX Analysis Note*, Oct 2014. https://www.phenix.bnl.gov/phenix/WWW/p/info/an/1195/Run13W2m_2014_10_12-03.pdf.

[45] Roger Barlow. Extended maximum likelihood. *Nuclear Instruments and Methods in Physics Research Section A: Accelerators, Spectrometers, Detectors and Associated Equipment*, 297(3):496 – 506, 1990.

[46] A. Adare, S. Afanasiev, C. Aidala, et al. Cross section and parity-violating spin asymmetries of $W^{\pm}$ boson production in polarized $p + p$ collisions at $\sqrt{s}$ = 500 GeV. *Phys. Rev. Lett.*, 106:062001, Feb 2011.

[47] Elke-Caroline Aschenauer, Alexander Bazilevsky, Kieran Boyle, et al. The rhic spin program: Achievements and future opportunities. 2012. BNL Published White Paper.

[48] Elke-Caroline Aschenauer et al. The RHIC SPIN Program: Achievements and Future Opportunities. 2015.

[49] Jozef Dudek et al. Physics Opportunities with the 12 GeV Upgrade at Jefferson Lab. *Eur. Phys. J.*, A48:187, 2012.

[50] A. Accardi et al. Electron Ion Collider: The Next QCD Frontier - Understanding the glue that binds us all. 2012.